

The Pennsylvania State University

The Graduate School

**INFLUENCE OF DEFECTS ON POLARIZATION DISTRIBUTION IN
FERROELECTRICS: A PHASE-FIELD STUDY**

A Dissertation in

Materials Science and Engineering

by

Xiaoxing Cheng

© 2020 Xiaoxing Cheng

Submitted in Partial Fulfillment

of the Requirements

for the Degree of

Doctor of Philosophy

August 2020

The dissertation of Xiaoxing Cheng was reviewed and approved by the following:

Long-Qing Chen

Hamer Professor of Materials Science and Engineering,

Professor of Engineering Science and Mechanics,

Professor of Mathematics

Dissertation Advisor, Chair of Committee

Michael Lanagan

Professor of Engineering Science and Mechanics

Venkatraman Gopalan

Professor of Materials Science and Engineering and Physics

Roman Engel-Herbert

Associate Professor of Materials Science and Engineering and Physics

John Mauro

Professor of Materials Science and Engineering

Chair, Intercollege Graduate Degree Program

Associate Head for Graduate Education, Materials Science and Engineering

Abstract

Ferroelectric is a large group of functional materials that has outstanding ferroelectric, piezoelectric, dielectric properties, and a wide range of applications, such as capacitors, actuators, transducers, random access memories, waveguides, etc. One of the defining features of the ferroelectric materials is the appearance of a complex switchable spontaneous polarization domain structure, which determines the effective properties of the studied material that leads to usage in different applications. In recent years, due to the increasing demand for novel nanoelectronic devices, scientists have been working on nanoscale domain engineering, which means understanding and manipulating the polarization domain structures at the nanoscale, to search for potential answers to the next generation semiconductors from a materials science perspective. In this dissertation, we study how defect engineering, particularly, dislocations in SrTiO_3 and non-stoichiometric charged defects in BiFeO_3 , may contribute to the control of both local and long-range polarization distribution at the nanoscale.

There is a long-standing interest in creating and stabilizing ferroelectric polarity in non-polar crystals such as SrTiO_3 . Recently, measurable electrical polarization as large as $\sim 28\mu\text{C}/\text{cm}^2$ has been reported at the dislocation cores in SrTiO_3 bicrystals [1]. The origin of this polarity was attributed to the flexoelectric effect, i.e., induced polarization due to strain gradients. In this work, we systematically study the role of flexoelectricity on inducing polarization around three types of dislocation cores in SrTiO_3 , $b = a(100)$ edge dislocation, $b = \frac{a}{2}(110)$ edge dislocation, and $b = a(010)$ screw dislocation. We demonstrate that, in the two edge dislocation cases, flexoelectricity has a significant influence on both the polarization's magnitude and distribution. It increases the average polarization value and drives the polarization into a symmetric distribution. For $b = a(100)$ edge dislocation, the ferroelectric phase is mainly tetragonal and can exist even without flexoelectricity, relying purely on the electrostrictive effect. For $b = \frac{a}{2}(110)$ edge dislocation, electrostriction alone is not sufficient to stabilize the ferroelectric phases, and flexoelectricity is essential for the presence of the orthorhombic polarization in this case. Moreover, through tuning of the three flexoelectric coefficients, we recognize the shear flexoelectric coefficient V_{1212} to have the largest effect on the stable polarization pattern and magnitude for both types of edge dislocations. In contrast, in the $b = a(010)$ screw

dislocation cases, we learn that neither electrostriction nor flexoelectricity will be able to stabilize any polar state in SrTiO₃. Our findings provide an in-depth understanding of the flexoelectric effects on the induced polarization around three dislocation cores, which may potentially bring new insights into the defect engineering of ferroic materials using dislocations.

A discussion about the role of dislocation core's electric effect on polarization distribution and the comparison with the elastic contribution is also crucial for the comprehensive understanding and prediction of polarization patterns near the dislocation cores in SrTiO₃. We explore the influence of defect charges on local polarization in room temperature SrTiO₃ of three types of dislocations, $b = a(100)$ edge dislocation, $b = \frac{a}{2}(110)$ edge dislocation, and $b = a(010)$ screw dislocation. We find that for edge dislocations, defect charges have a shorter interaction range compares to the flexoelectric effect. The charge induced polarization has a highly anisotropic distribution that is directly related to the local stress state of the system. Defect charges, in the edge dislocation cases, lead to larger polarization value at the dislocation core comparing to the flexoelectric and electrostrictive effect, while the defect's elastic effects have a broader impact region and larger magnitude than the electric ones. Similar polarization distribution can be observed in experimental characterization of regions around $b = a(100)$ edge dislocations in SrTiO₃ [1]. In the screw dislocation case, the defect charges induce an almost isotropic polarization distribution around the dislocation core. At the same time, flexoelectricity has no influence on the polarization due to the contrary contribution of the non-zero shear stress to the flexoelectric field. Overall, the pure electric effect of the defect charges leads to a nearly isotropic distribution of local polarization within 1 nm around the dislocation core for all three types of dislocations. The flexoelectric effect has a much larger impact on polarization in the two edge dislocation cases than the screw dislocation case. The electrostrictive effect only affects the polarization distribution in the two edge dislocation cases since the location of the total free energy minima is shifted by the local normal stresses while remaining almost unchanged with the presence of the shear stress components. These results provide a comprehensive understanding of how the elastic and electric effects of dislocations in ferroic materials help to stabilize the local polarization around the dislocation cores.

Another type of defect engineering system that we investigate to control the ferroelectric domain structures is the non-stoichiometric charged defect in BiFeO₃. The differences between this type of defect and the dislocation are, first, it has no lattice mismatch with the matrix (zero eigenstrain); second, it is a two-dimensional defect. We study how the planar non-stoichiometric charged defect configurations, including defect width, interval, and location, may determine the thermodynamically most stable domain structure inside the thin film. We perform high-throughput simulations varying the defect width, interval, and height within a 200 nm BiFeO₃ thin film. The trends for every energy term with respect to the defect configurations are explained and analyzed. The stability of the 71° domain strips above the charged defects is explained through the competition between elastic and domain wall energy. We obtain an empirical formula that relates the defect

width, position, and thin film thickness with the final domain pattern, which can be used as a predictive tool for the occurrence of the 71° domain strips above the defects in similar BiFeO_3 thin film systems. Our conclusion is that there exists a minimal defect width that favors 71° domain above the charged defect over a single domain state. The threshold value is determined by the thin film thickness and the defect configuration. This result provides a novel route to precisely control the 71° domain pattern formation in BiFeO_3 .

The planar non-stoichiometric charged defect in BiFeO_3 of a smaller dimension (less than 10 nm) may also affect the equilibrium domain structures in a ferroelectric thin film. We perform high-throughput simulations varying the defect width, location, shape, charge state, electric boundary condition, and initial domain structure within a 100 nm BiFeO_3 thin film. We identify the factors that have significant influences on the polarization distribution and several configurations that can stabilize the 109° domain wall, thus applicable as a novel nanoscale domain engineering method. Under the short circuit boundary condition, for a negatively charged defect, we found that the defect thickness (or shape) determines whether we can get a local hedgehog state around the defect or not. Varying the defect thickness also leads to a preference for either 180° or 109° domain pattern below the defect. On the other hand, defect width and defect location have limited influence on the final domain pattern. For neutrally charged defects, the domain pattern is relatively insensitive to defect location and defect thickness. It favors a 109° domain above the defect, except when the defect width is too small, and a single domain state is preferred over the 109° domain pattern for the final polarization state. In the open circuit cases, we observe smaller domains, in other words, a higher density of domain walls, and more interaction between the charged defect and the 109° domain wall, comparing to their short circuit counterparts. We discover that the initial domain structure, whether it is random noise or a single domain, will affect the equilibrium polarization, indicating the possibility of experimental tricks such as small miscut angle or introduction of built-in potential may also contribute to the control of the as-grown domain pattern around the defect. These results illustrate how we can utilize the defects as a novel method to control the occurrence 109° domain wall in future nanoscale domain engineering applications.

This work presents in-depth understandings of the local and long-range polarization pattern formation within two defect systems, which provides a solid basis for future experimental design and validation. We discuss the flexoelectric, electrostrictive, and defect charges contribution to local polarization around edge and screw dislocations in SrTiO_3 . Further, we perform a series of high-throughput simulations to explore the influences of non-stoichiometric charged defect configurations on long-range 71° and 109° domain pattern stability in defect engineered BiFeO_3 . This work clearly demonstrates the possibility and capability of precise domain pattern control through defect engineering, which could be a viable route to the design and fabrication of more complicated ferroelectric nano-devices.

Table of Contents

List of Figures	ix
List of Tables	xv
List of Symbols	xvi
Acknowledgments	xviii
Chapter 1	
Introduction	1
1.1 Overview	1
1.2 Background of SrTiO ₃	2
1.2.1 Dislocations in SrTiO ₃	5
1.2.2 SrTiO ₃ parameters for phase-field modeling	6
1.3 Background of BiFeO ₃	10
1.3.1 Charged defects in BiFeO ₃	13
1.3.2 BiFeO ₃ parameters for phase-field modeling	14
1.4 Computational method	17
1.4.1 Phase-field model	17
1.4.2 Numerical method of the phase-field model for ferroelectric	22
1.5 Objectives	27
1.6 Dissertation structure	29
Chapter 2	
Role of flexoelectric effect on polarization around dislocation in SrTiO₃	31
2.1 Introduction	31
2.2 Materials and Methods	34
2.3 Results and Discussion	37
2.4 Conclusion	50
Chapter 3	
Role of defect charge on polarization around dislocation in SrTiO₃	52

3.1	Introduction	52
3.2	Materials and methods	55
3.3	Results and discussion	56
3.4	Conclusion	63
Chapter 4		
	Control the 71° domain patterns in BiFeO₃ through defect engineering	65
4.1	Introduction	65
4.2	Materials and method	69
4.3	Results and discussion	72
4.4	Conclusion	80
Chapter 5		
	The influence of defect topology on polarization distribution	81
5.1	Introduction	81
5.2	Materials and method	84
5.3	Results and discussion	87
5.4	Conclusion	93
Chapter 6		
	Conclusions and Future works	95
6.1	Conclusion	95
6.2	Future works	98
6.2.1	Dislocation dynamics in SrTiO ₃	98
6.2.2	Free carrier evolution in SrTiO ₃	99
Appendix		
	Bulk, thin film and membrane elastic solver	100
1	Bulk homogeneous system	100
1.1	The homogeneous(macroscopic) part	101
1.2	The heterogeneous(microscopic) part	102
2	Thin film homogeneous system	103
2.1	The homogeneous(macroscopic) part	104
2.2	The heterogeneous(microscopic) part	105
2.2.1	Part A: Non-zero rhs, periodic BC	105
2.2.2	Part B: Zero-rhs, thin film BC	105
3	Membrane homogeneous system	114
3.1	The homogeneous(macroscopic) part	114
3.2	The heterogeneous(microscopic) part	116
3.2.1	Part A: Zero rhs, periodic BC	117
3.2.2	Part B: Non-zero rhs, membrane BC	117
4	Bulk inhomogeneous system	120
4.1	The homogeneous (macroscopic) part	121

4.2	The heterogeneous (microscopic) part	122
5	Thin film inhomogeneous system	124
5.1	The homogeneous (macroscopic) part	124
5.2	The heterogeneous (microscopic) part	125
5.2.1	Part A: Non-zero rhs, periodic BC	125
5.2.2	Part B: Zero rhs, thin film BC	125
6	Membrane inhomogeneous system	126
6.1	The homogeneous (macroscopic) part	126
6.2	The heterogeneous (microscopic) part	126
6.2.1	Part A: None-zero rhs, periodic BC	126
6.2.2	Part B: Zero rhs, membrane BC	127

Bibliography **128**

List of Figures

1.1	Blue spheres are Ti atoms, red spheres are O atoms, and green spheres are Sr atoms. Left, the high temperature ($>105\text{K}$) cubic paraelectric phase. Middle, the low temperature ($<105\text{K}$) tetragonal antiferrodistortive phase. Right, illustration of the out-of-phase oxygen octahedral tilt of the antiferrodistortive phase in a pseudocubic manner. The octahedra in the upper layer is rotated counterclockwisely around c axis, and the octahedra in the lower layer is rotated clockwise.	4
1.2	Dielectric constants of monodomain SrTiO_3	5
1.3	The rhombohedral structure of BiFeO_3 with oxygen octahedral tilt. Left, a primitive cell. Right, two pseudocubic cells. Purple spheres are Bi atoms, red spheres are O atoms, and brown spheres are Fe atoms.	11
1.4	Flowchart of the phase-field program	25
2.1	Comparison of stress distribution around (100) dislocation core between analytical and simulation results. All data in comparison are taken from the stress profile along a line 1 nm to the right of the dislocation core. (a), σ_{11} (b), σ_{13} (c) σ_{33} . Subscript 1 means the horizontal x direction. 2 means the y direction that goes into the paper which is invisible. 3 means the vertical z direction.	35
2.2	The simulation setup. (a) A total of 75 jobs, with 5 sets of flexoelectric coefficient, 3 sets of Burgers vector, and 5 different random seeds, are calculated. (b) The (100) edge dislocation setup, (c) (110) partial edge dislocation setup. (d) (010) screw dislocation setup.	36

2.3	Stress and strain gradient distribution around $b = a(100)$ edge dislocation core. (a) σ_{11} , (b) σ_{33} , (c) σ_{13} , (d) $\nabla\epsilon_{11}$, (e) $\nabla\epsilon_{33}$, (f) $\nabla\epsilon_{13}$. Subscript 1 means the horizontal axis to the right, subscript 3 means the vertical axis to the up, and 2 is the axis goes into the paper plane. Dislocation core is located at the center of the region labeled by the green marker.	38
2.4	The total free energy landscape of SrTiO ₃ under various conditions. (a) stress free. (b) 3% tensile strain along vertical y direction. (c) 3% compressive strain along vertical y direction. (d) 3% shear strain.	39
2.5	Illustration of each strain gradient component's contribution to the final flexoelectric field for case 8. The light green column is strain gradient, the area of each circle is proportional to the maximum value of that strain gradient component. The dark green column is the flexoelectric coefficients for case 8, the area of which is proportional to the value of each flexoelectric coefficient. The two rectangles in the right column represent the x and z component of flexoelectric field vector. The area of each color shows the contribution from each strain gradient.	40
2.6	Comparison of polarization distribution with and without flexoelectric effect. (a) Polarization distribution without flexoelectricity. (b) Polarization distribution considering flexoelectricity. The quivers in (a),(b) indicate the polarization vector, and the background heat plot illustrates the magnitude of polarization. (c) Statistics of average and maximum Px, Pz and P total magnitude. (d) Flexoelectric field distribution, quivers indicate the flexoelectric field and background heat plot shows the magnitude of flexoelectric field.	41
2.7	The polarization and flexoelectric field distribution using different flexoelectric coefficients for $b = a(100)$ edge dislocation. White quiver represent the plotted vector field, and background heat plot shows the magnitude of the vector.(a, b, c) Polarization distribution. (d, e, f) Flexoelectric field distribution. (a, d) non-zero longitudinal flexoelectric coefficient. (b, e) non-zero transverse flexoelectric coefficient. (c, f) non-zero shear flexoelectric coefficient.	42
2.8	The polarization and flexoelectric field distribution using different flexoelectric coefficients for $b = a(100)$ edge dislocation. White quiver represent the plotted vector field, and background heat plot shows the magnitude of the vector.(a, b, c) Polarization distribution. (d, e, f) Flexoelectric field distribution. (a, d) 2V non-zero longitudinal coefficient. (b, e) 2V, non-zero transverse coefficient. (c, f) 2V, non-zero shear coefficient.	44

2.9 The changes in overall polarization with small increment in the flexoelectric coefficient. Simulations in this graph are performed with only one non-zero flexoelectric coefficient while keeping the other two zero, and the varying range of each coefficient is from 0 V to 3 V with an increment of 0.1 V. For the percentage value of y axis, we need to first subtract the polarization of smaller coefficient setup from the setup that the coefficient is larger by 0.1 V, and then sum the magnitude of such polarization difference over the whole simulation system to obtain a scalar value representing the total changes in polarization, then normalize it by the total polarization of the smaller flexoelectric coefficient case. Peak on this graph means a small change in flexoelectric coefficient will lead to large variation in the polarization distribution. 45

2.10 Stress and strain gradient distribution around (110) partial dislocation core. The dimension of the plotted region is 10nm by 10nm, and the dislocation is located at the center, labeled by the green T shape marker. 46

2.11 The polarization distribution using different flexoelectric coefficients for $b = \frac{a}{2}(110)$ edge dislocation. (a) no-flexo. (b) case 2 flexoelectric coefficient (d) non-zero longitudinal coefficient (e) non-zero transverse coefficient (f) non-zero shear coefficient. (c) Sum of total polarization for each orientation angle with respect to the (100) direction. Peak means more polarization is aligned along such direction. 47

2.12 Flexoelectric field distribution of case 2, 3, 4, 5 for (110) partial edge dislocation. 48

2.13 The results for $b = a(010)$ screw dislocation. (a), (b) polarization distribution without flexoelectricity and with case 2 flexoelectric coefficients, white dots are actually quivers for polarization and the background color is the magnitude of the polarization. 49

2.14 The results for $b = a(010)$ screw dislocation. (a) σ_{12} distribution. (b) σ_{23} distribution. (c), (d) White quiver shows $\nabla\epsilon_{12}$ and $\nabla\epsilon_{23}$ respectively, background color is distribution of $\frac{\partial\epsilon_{12}}{\partial x}$ and $\frac{\partial\epsilon_{23}}{\partial z}$, respectively. 50

3.1 Comparison of polarization distribution with and without defect charges. White quivers represent polarization vectors, background heat map shows the polarization magnitude, and green crosses mark the location of dislocations. In all cases flexoelectricity are considered. (a), (b), (c) with $0.96 \times 10^{-10} C/m$ defect charge at dislocation core. (d), (e), (f) 0 defect charge. (a), (d) $b = a(100)$ edge dislocation. (b), (c) $b = \frac{a}{2}(110)$ edge dislocation. (c), (f) $b = a(010)$ screw dislocation. 57

3.2 Radial distribution of maximum polarization around the dislocation core. Lower panel is for control group 1, when flexoelectricity is ignored, and defect charge is considered. The upper panel is for control group 2, in which flexoelectricity is taken into account but without defect charge. . . . 58

3.3 Polarization distribution for control group 1 (a) $b = a(100)$ edge, (b) $b = \frac{a}{2}(110)$ edge, (c) $b = a(010)$ screw. (d) Experimental polarization mapping around a $b = a(100)$ edge dislocation in 10° SrTiO₃ bicrystal, the direction of polarization is indicate by the illustration arrows on top, and the magnitude is shown by the color. The white trapezoid represents the dislocation core. (e) Illustration of the free energy profile with respect to the polarization value under different conditions. Red dash line shows energy profile of strong electrostrictive coupling. Solid green line shows the energy profile when both external electric field and applied strain exists. And the dot purple line shows the landau part of the total free energy, which can be considered as a reference for the other two curves. 59

3.4 Angular distribution for the summation of total polarization for every 10° of orientational angle. X axis is the angle between polarization and (100) direction. Left green axis is for the results of control group 1, in which there is non zero defect charge but no flexoelectricity, and right blue axis is for the results of control group 2, in which flexoelectricity is considered but without defect charge. The three panels correspond to the three types of dislocation, as shown on the right of the figure. 60

3.5 Electric field and flexoelectric field distribution for the three types of dislocations. (a), (b) and (c) electric field of control group 1, with defect charge, no flexoelectricity. (d), (e) and (f) the flexoelectric field of control group 2, with flexoelectricity, but 0 defect charge. 62

4.1	Experimental results. (a) Cross-sectional bright-field TEM image and corresponding schematic of polarization structures showing ordered 71° and 109° domains separated by an array of defects in a 400 nm BiFeO_3 film. (b) PFM phase image showing the same periodically ordered domain patterns in the same BiFeO_3 film. [2]	68
4.2	The parameter space that is explored with our high-throughput simulations.	69
4.3	The 5 preset domain structures that we have studied. (a) Case 0, (b) Case 4, (c) Case 3, (d) Case 2, (e) Case 1. Case number means one 71° domain strip every n^{th} of defects. The meaning of width, interval and height are marked in (a). Each color represent one type of polarization domain, gray represents substrate, and the polarization directions are labeled in (c). All four types of domain walls are labeled in (b).	71
4.4	Free energy components for Case 2 (Figure 4.3d) varying defect width and interval. The defect height is fixed at 100 nm. (a) Elastic energy density. (b) Gradient energy. (c) Landau energy density.	72
4.5	Free energy components for Case 2 varying defect height and width. The defect interval is chosen to be the same as defect width. (a) Elastic energy density. (b) Gradient energy. (c) Landau energy density.	74
4.6	The elastic and gradient energy difference between Case 2 and Case 0.(a), (b) have the same setup as in Figure 4.4. (c), (d) have the same setup as in Figure 4.5.	75
4.7	Linear fitting of energies for all simulation setups. (a) The linear relationship between elastic energy density and 71° domain percentage. (b) The gradient energy's relationship with defect width at various defect height. (c) The relationship between the gradient energy and the defect height at various defect width.	77
5.1	Comparison of polarization distribution around defects in experiment and simulation. (a, b, c, d) Polarization vector mapped from experimental HRTEM images. (e, f, g, h) the corresponding phase-field simulation results with the same setup as experimental observations.	83

5.2 The 4 defect shapes that we have studied. Color represent the amount of defect charges we added, navy blue means negative charge, bright yellow means positive charge. (a) Case 1, loop shape, negatively charged defect. (b) Case 2, loop shape, neutrally charged defect. (c) Case 3, planar shape, negatively charged defect. (d) Case 4, planar shape, neutrally charged defect. 85

5.3 The parameter space that is explored with high-throughput simulations. . 87

5.4 Simulation results under open circuit and short circuit electric boundary conditions. All other defect configurations are controlled to be the same. Defect width is 6.4 nm. Defect location is 3.2 nm away from the interface. All simulations are starting from random but with different random seeds. The arrows illustrate the direction and magnitude of the polarization, and the background color represent the defect charges. 89

5.5 Phase-field simulation results starting from different initial conditions, two random polarization distribution, initial R1+ (+,+,+) domain, and initial R2- (+,-,-). All other defect configurations are controlled to be the same. Defect width is 9.6 nm. Defect height is 9.6 nm. Electric boundary condition is the short circuit boundary condition. 90

5.6 Polarization distribution for defects at various heights, 3.2 nm and 9.6 nm, and either open or short circuit electric boundary conditions. All simulations are starting from random initial polarization, with a defect width of 9.6 nm. 91

5.7 Polarization distribution for different defect width, 6.4 nm and 12.8 nm, and either open or short electric boundary conditions. All simulations are starting from random noise, with a defect height of 6.4 nm. 92

List of Tables

1.1	Possible slip system and their corresponding Peierls stress. [3]	6
1.2	SrTiO ₃ coefficients for phase-field simulation	6
1.2	SrTiO ₃ coefficients for phase-field simulation	7
1.2	SrTiO ₃ coefficients for phase-field simulation	8
1.2	SrTiO ₃ coefficients for phase-field simulation	9
1.2	SrTiO ₃ coefficients for phase-field simulation	10
1.3	BiFeO ₃ coefficients for phase-field simulation	15
1.3	BiFeO ₃ coefficients for phase-field simulation	16

List of Symbols

- η Order parameters, in our case, the three components of polarization vector p_1, p_2, p_3 and three component of oxygen octahedral rotation q_1, q_2, q_3 , p. 21
- t Time, p. 21
- L Kinetic coefficient that controls the evolution speed of the simulation, p. 21
- F Total free energy of the system, which is the spatial integration of energy density, p. 21
- Ω The simulation domain, in our case the 3D system, p. 21
- f_{land} The landau free energy density which includes the double well potential for polarization, oxygen octahedral tilt and the coupling between them, p. 21
- f_{elec} The electric energy density, p. 21
- f_{elas} The elastic energy density, p. 21
- f_{flexo} The flexoelectric energy density, p. 21
- f_{grad} The gradient energy density, p. 21
- \mathbf{p} The polarization vector, has three components, p_1, p_2, p_3 , p. 21
- \mathbf{q} The oxygen octahedral tilt and rotation, has three components, q_1, q_2, q_3 , p. 21
- α The landau coefficient for polarization, including the second order terms $\alpha_1, \alpha_2, \alpha_3$, the fourth order terms α_{11}, α_{12} , and the sixth order terms $\alpha_{111}, \alpha_{112}, \alpha_{123}$, p. 21
- β The landau coefficient for octahedral rotation, including the second order terms $\beta_1, \beta_2, \beta_3$, the fourth order terms β_{11}, β_{12} , and the sixth order terms $\beta_{111}, \beta_{112}, \beta_{123}$, p. 21

γ_{ijkl}	The coupling landau coefficient between polarization and oxygen octahedral tilt, it is a fourth order term, $i, j, k, l = 1, 2, 3$, p. 21
\mathbf{E}	The electric field, E_1, E_2, E_3 , p. 21
ϵ_0	The vacuum permittivity, $\epsilon_0 = 8.854187 \times 10^{-12} F \cdot m^{-1}$, p. 21
κ_{ij}	The background permittivity 2nd rank tensor, p. 21
C_{ijkl}	Elastic stiffness 4th rank tensor, p. 21
ϵ_{ij}	The total strain tensor, $\epsilon_{ij}, i, j = 1, 2, 3$. it includes elastic strain and eigenstrain, p. 21
ϵ_{ij}^0	The eigenstrain tensor, $i, j = 1, 2, 3$. it is related to the stress free strain changes, p. 21
V_{ijkl}	The flexoelectric coefficient tensor, $i, j, k, l = 1, 2, 3$. p. 21
x_i	The coordinate axis, x_1, x_2, x_3 , p. 21
G_{ijkl}^p	The gradient energy coefficient for order parameter \mathbf{p} , polarization. p. 21
G_{ijkl}^q	The gradient energy coefficient for order parameter \mathbf{q} , oxygen octahedral tilt. p. 21
ϕ	The electric potential, p. 21
Q_{ijkl}	The electrostrictive coefficient, p. 21
R_{ijkl}	The rotostrictive coefficient, p. 21
v_{ijkl}	The reverse flexoelectric coefficient, p. 21
b_i	The burgers vector of dislocation, p. 21
n_i	The normal direction of sliding plane for dislocation, p. 21
d_0	The distance bewteen atomic plane, p. 21
ρ_{defect}	The charge density of defect, p. 21

Acknowledgments

First, I would like to thank my advisor, Dr. Long-Qing Chen, for all of the guidance and supports he provided throughout my Ph.D. research at The Pennsylvania State University. It is the understanding and encouragement Dr. Chen gave me that allows me to find my passion for code development of simulations. He also connected me to many smart and unique collaborators that I would otherwise have never been able to work with. Second, I would like to thank several former group members, Dr. Yulan Li, Dr. Ben Winchester, and Dr. Jason Britson, for all of their efforts in developing the phase-field simulation program that I further improved and personalized for all of my own researches. Third, I would like to thank all of my experimental collaborators. The BiFeO_3 researches in this dissertation are inspired by the fruitful collaboration with Dr. Linze Li from Dr. Xiaoqing Pan's group. The SrTiO_3 researches are inspired by the collaboration with Ning Li from Dr. Peng Gao's group and Lukas Porz from Dr. Jürgen Rödel's group. Fourth, I would like to thank all of my lab mates. I had numerous fruitful discussions with many of them, and they had inspired many new ideas for my researches. Finally, I would like to thank my mother, Guiping Dong, and my father, Weijun Cheng. They allow me to take my time and have my own pace to figure out what I want to do for my career.

Financial support for this research was through the U.S. Department of Energy, Office of Basic Energy Sciences, Division of Materials Sciences and Engineering under Award DE-FG02-07ER46417. All computations for this research were performed on the Pennsylvania State University's Institute for Computational and Data Sciences Advanced CyberInfrastructure (ICDS-ACI).

Any opinions, findings, and conclusions or recommendations expressed in this dissertation are those of the author and do not necessarily reflect the views of the U.S. Department of Energy and the Pennsylvania State University.

Chapter 1 |

Introduction

1.1 Overview

Ferroelectrics are a group of functional materials that exhibit ferroelectricity over a temperature range. The defining characteristics are a complex microstructure of the spontaneous polarization domain, which can be switched by applying an external electric field. According to symmetry, only 10 out of the 32 point groups are allowed to have ferroelectricity, and all ferroelectric materials are automatically pyroelectric and piezoelectric. Thus, ferroelectrics are one of the most widely used functional materials in many of our daily applications. Ferroelectrics are old and young. It has a long history since researchers found the first ferroelectric material almost a century ago in Rochelle salt [4] and KH_2PO_4 [5]. Since then, scientists have discovered various materials systems including BaTiO_3 [6], $\text{Pb}(\text{Zr}, \text{Ti})\text{O}_3$ [7], BiFeO_3 [8], $\text{PbMg}_{1/3}\text{Nb}_{2/3}\text{O}_3\text{PbTiO}_3$ [9], etc., and have been studying the physics of ferroelectrics, such as the phenomenological theory of ferroelectrics [10], the lattice dynamics theory and phonon mode softening of ferroelectrics [11], morphotropic phase boundaries in ferroelectrics [12], domain engineering of periodic polarization pat-

terns within bulk single crystal [13]. Over the years, people have utilized ferroelectrics in many applications, for example, the usage of BaTiO_3 as high-dielectric constant ceramics in capacitors [14], piezoelectric generator used in fuel igniter, piezoelectric motor and actuator used in Microelectromechanical Systems (MEMS), ultrasonic transducer used in medical ultrasonography, PbTiO_3 pyroelectric thin-film infrared sensors [15], etc. On the other hand, ferroelectric is also young because it is an active field of research, scientists are still discovering and fabricating new materials in the recent decade, such as halide perovskite ferroelectrics for photovoltaic applications [16], metal-free three-dimensional perovskite ferroelectrics for flexible devices [17], the domain wall nanoelectronics [18], transparent ferroelectric single crystal [19], etc.

From the materials science perspective, studying and controlling the material's microstructure is always one of the most critical tasks, and within the context of ferroelectric materials, microstructure means the spontaneous polarization domain pattern. In this dissertation, we explore how do defects, such as dislocations and non-stoichiometric charged defects, influence the polarization domain patterns.

1.2 Background of SrTiO_3

SrTiO_3 was first synthesized along with several other titanates in the 1950s. The natural source of SrTiO_3 was discovered decades later, in an extremely rare mineral called tausonite. At room temperature, strontium titanate (SrTiO_3) is a perovskite paraelectric material, with a cubic space group of $\text{Pm}\bar{3}\text{m}$, lattice parameter of 3.9053 Å, and relative dielectric permittivity of about 300. It is a wide band gap semiconductor, with an indirect band gap of 3.25 eV and a direct gap of 3.75 eV [20]. Thus, SrTiO_3 is a better insulator compare to other perovskite complex oxides, such as BiFeO_3 , BaTiO_3 , LiNbO_3 , etc. At

low temperature (105 K), SrTiO₃ undergoes a structural transition, also known as the antiferrodistortive transition [21], from cubic (space group Pm $\bar{3}$ m, point group m $\bar{3}$ m) to tetragonal (space group I4/mcm, point group 4/mmm). The zone boundary phonon mode softens, as the TiO₆ cage (oxygen octahedra) in SrTiO₃ rotates, and forms the oxygen octahedral tilt domains structures [22,23]. According to Glazer [24], the tilt system for SrTiO₃ is $a^0a^0c^-$, so only out-of-phase tilt along the c axis exists. The three letters of glazer notation represent tilting along the pseudocubic [001], [010] and [001] axis, and the superscript, which could be either -, +, or 0, represents whether the tilting angle of neighbouring octahedra along that specific direction is the same, opposite or no tilting. The glazer notation $a^0a^0c^-$ for SrTiO₃ means no oxygen octahedra tilt along the a and b axis, and out-of-phase tilt along the c axis which is the "elongated axis" in a tetragonal system. The octahedra rotation angle is usually small, about 1° ~ 2° according to [23,25]. The transition from cubic to tetragonal phase will lead to three degenerated phases, in which the c axis of the tetragonal phase lies along the three perpendicular cubic axes. Thus, in the phase-field modeling for SrTiO₃, three out-of-phase tilting order parameters, each describing the tilting along one of the three axes, is enough to represent all 6 of the possible oxygen octahedral tiling phases. Figure 1.1 shows the crystal structure of the cubic and tetragonal phases of SrTiO₃, and illustrates the out-of-phase tilting along the c axis in SrTiO₃.

In SrTiO₃, as the temperature decreases, there is another phonon softening mode at the zone center Γ point (Γ_{15} mode) [26,27], which is related to the ferroelectric phase transition. This phonon softening is never fully completed, and such a tendency of displacive ferroelectric phase transition gives SrTiO₃ two new names, quantum paraelectric and incipient ferroelectrics. These names come from researchers' belief that it is the

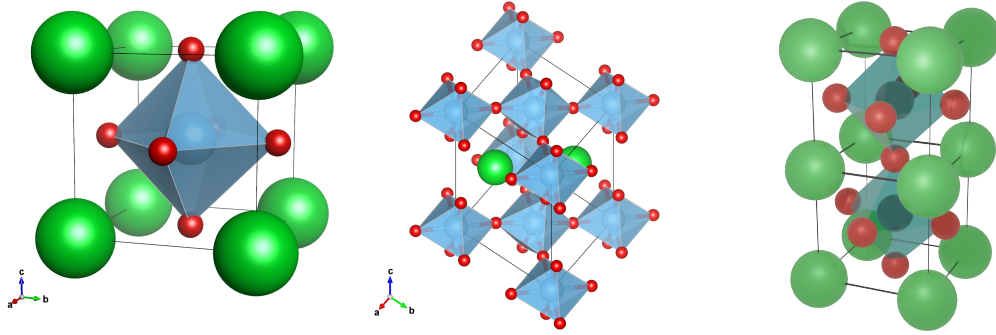


Figure 1.1. Blue spheres are Ti atoms, red spheres are O atoms, and green spheres are Sr atoms. Left, the high temperature ($>105\text{K}$) cubic paraelectric phase. Middle, the low temperature ($<105\text{K}$) tetragonal antiferrodistortive phase. Right, illustration of the out-of-phase oxygen octahedral tilt of the antiferrodistortive phase in a pseudocubic manner. The octahedra in the upper layer is rotated counterclockwisely around c axis, and the octahedra in the lower layer is rotated clockwisely.

large quantum fluctuation that prevents SrTiO_3 's transitioning from paraelectric phase to ferroelectric phase [28, 29]. Experimental evidence for the suppression of ferroelectricity due to quantum fluctuation shows that as SrTiO_3 deviates away from the Curie law below 35.5K , the dielectric constant reaches a plateau with value more than 10,000 as shown in Figure 1.2.

A natural question to ask within the context of SrTiO_3 quantum paraelectric is that how we can break the central symmetry and stabilize the polar states. There are several popular ways to achieve this goal, first, inducing local random field by doping, for example substituting a small amount of Sr by Ca [31], Bi [32], Pr [33], etc.; second, inducing local strain field through chemical substitution, for example, Fe [34]; third, isotope substitution of the oxygen element from O^{16} to O^{18} [35] which stabilize a normal ferroelectric static rather than the relaxor states in doped SrTiO_3 due to local random field; fourth, utilizing the mechanical effect, such as application of external stress [36] or clamping of the SrTiO_3 lattice through epitaxial thin film growth [37]; fifth, applying giant external electric field [38].

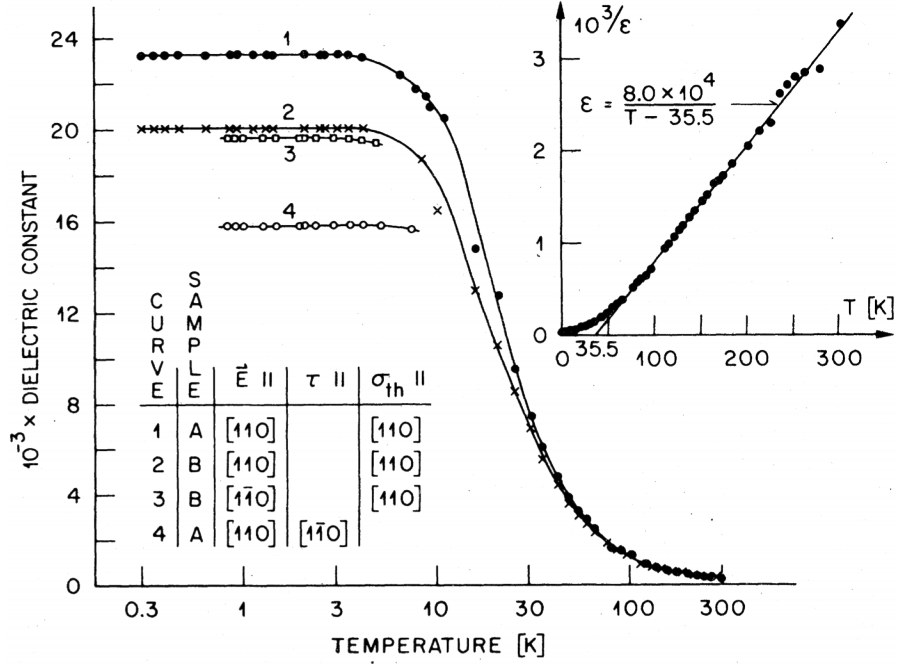


Figure 1.2. Dielectric constants of monodomain SrTiO₃ from [30].

There are many other interesting properties of SrTiO₃, for example, it becomes superconductor at 0.35 K [39], it is widely used as a substrate for epitaxial growth of other perovskite thin films [40], it is a novel photocatalyst for the water splitting process [41], and the LaAlO₃/SrTiO₃ heterostructures interface exhibits behaviors of 2 dimensional electron gas [40].

1.2.1 Dislocations in SrTiO₃

The plastic deformation of SrTiO₃ exhibits an interesting three stages transition, from ductile to brittle around 1000K, and then back to ductile again at higher temperature (this temperature is different for various types of dislocations, 1500K for <100> dislocation, and about 1300K for the others) [42]. For a cubic perovskite structure, we can obtain all possible slip systems of dislocations as shown in table (1.1) [3], from which we can calculate the Peierls stress τ using the equation (1.1). μ is the shear modulus, v is the

Table 1.1. Possible slip system and their corresponding Peierls stress. [3]

Slip plane	b	d/b	τ/μ
{001}	$\langle 100 \rangle$	0.5	3×10^{-2}
	$\langle 110 \rangle$	0.29	2×10^{-1}
{011}	$\langle 100 \rangle$	0.35	1×10^{-1}
	$\langle 011 \rangle$	0.25	3×10^{-1}
{111}	$\frac{1}{2}\langle 110 \rangle$	0.50	3×10^{-2}
	$\langle 110 \rangle$	0.2	5×10^{-1}
	$\frac{1}{3}\langle 112 \rangle$	0.35	10^{-1}

Poisson's ratio, b is the burgers vector, d is the interplanar spacing of the corresponding slip plane.

$$\frac{\tau}{\mu} = \frac{2}{1-v} e^{-\frac{2\pi d}{(1-v)b}} \quad (1.1)$$

Clearly, the full dislocation in $\langle 100 \rangle$ -{100} slip system and the partial dislocation in $\frac{1}{2}\langle 110 \rangle$ -{110} slip system have the smallest Peierls stress, and thus are the easiest ones to activate. According to experiment, in the high temperature regime the $\langle 100 \rangle$ -100 system is activated, while in the low temperature regime the $\langle 110 \rangle$ -110 system is activated [42]. In experiment, researches have verified the existence of the partial edge dislocation pairs of $\frac{1}{2}\langle 110 \rangle$ [43], $\langle 100 \rangle$ edge dislocation [44] and $\langle 100 \rangle$ screw dislocation [45].

1.2.2 SrTiO₃ parameters for phase-field modeling

Table 1.2: SrTiO₃ coefficients for phase-field simulation

Name	Meaning	Value	Unit
$\alpha_1, \alpha_2, \alpha_3$	Landau coefficient	$4.05 \times 10^7 \times [\coth(\frac{54}{T}) - \coth(\frac{54}{30})]$	$\frac{N \cdot m^2}{C^2}$
$\alpha_{11}, \alpha_{22}, \alpha_{33}$	Landau coefficient	1.70×10^9	$\frac{N \cdot m^6}{C^4}$

Table 1.2: SrTiO₃ coefficients for phase-field simulation

Name	Meaning	Value	Unit
$\alpha_{12}, \alpha_{13}, \alpha_{23}$ $\alpha_{21}, \alpha_{32}, \alpha_{31}$	Landau coefficient	1.96×10^9	$\frac{N \cdot m^6}{C^4}$
$\beta_1, \beta_2, \beta_3$	Landau coefficient	$1.32 \times 10^{29} \times [\coth(\frac{145}{T}) - \coth(\frac{145}{105})]$	$\frac{N}{m^4}$
$\beta_{11}, \beta_{22}, \beta_{33}$	Landau coefficient	1.69×10^{50}	$\frac{N}{m^6}$
$\beta_{12}, \beta_{13}, \beta_{23}$ $\beta_{21}, \beta_{32}, \beta_{31}$	Landau coefficient	1.94×10^{50}	$\frac{N}{m^6}$
$\gamma_{1111}, \gamma_{2222}, \gamma_{3333}$	p, q coupling coefficient	-1.74×10^{29}	$\frac{N}{C^2}$
$\gamma_{1122}, \gamma_{1133}, \gamma_{2233}$ $\gamma_{2211}, \gamma_{3311}, \gamma_{3322}$	p, q coupling coefficient	-0.755×10^{29}	$\frac{N}{C^2}$
$\gamma_{1212}, \gamma_{2323}, \gamma_{1313}$ $\gamma_{1221}, \gamma_{2332}, \gamma_{1331}$ $\gamma_{2112}, \gamma_{3223}, \gamma_{3113}$ $\gamma_{2121}, \gamma_{3232}, \gamma_{3131}$	p, q coupling coefficient	0.733×10^{29}	$\frac{N}{C^2}$
$C_{1111}, C_{2222}, C_{3333}$	Elastic stiffness tensor	3.36×10^{11}	$\frac{N}{m^2}$
$C_{1122}, C_{1133}, C_{2233}$ $C_{2211}, C_{3322}, C_{3311}$	Elastic stiffness tensor	1.07×10^{11}	$\frac{N}{m^2}$

Table 1.2: SrTiO₃ coefficients for phase-field simulation

Name	Meaning	Value	Unit
$C_{1212}, C_{2323}, C_{1313}$	Elastic stiffness tensor	1.27×10^{11}	$\frac{N}{m^2}$
$C_{1221}, C_{2332}, C_{1331}$			
$C_{2112}, C_{3223}, C_{3113}$			
$C_{2121}, C_{3232}, C_{3131}$			
$Q_{1111}, Q_{2222}, Q_{3333}$	Electrostrictive tensor	0.0457	$\frac{m^4}{C^2}$
$Q_{1122}, Q_{1133}, Q_{2233}$	Electrostrictive tensor	-0.0135	$\frac{m^4}{C^2}$
$Q_{2211}, Q_{3311}, Q_{3322}$			
$Q_{1212}, Q_{2323}, Q_{1313}$	Electrostrictive tensor	0.0023925	$\frac{m^4}{C^2}$
$Q_{1221}, Q_{2332}, Q_{1331}$			
$Q_{2112}, Q_{3223}, Q_{3113}$			
$Q_{2121}, Q_{3232}, Q_{3131}$			
$R_{1111}, R_{2222}, R_{3333}$	Rotostriptive tensor	8.7×10^{18}	m^{-2}
$R_{1122}, R_{2233}, R_{1133}$	Rotostriptive tensor	-7.8×10^{18}	m^{-2}
$R_{2211}, R_{3322}, R_{3311}$			
$R_{1212}, R_{2323}, R_{1313}$	Rotostriptive tensor	-2.3×10^{18}	m^{-2}
$R_{1221}, R_{2332}, R_{1331}$			
$R_{2112}, R_{3223}, R_{3113}$			
$R_{2121}, R_{3232}, R_{3131}$			

Table 1.2: SrTiO₃ coefficients for phase-field simulation

Name	Meaning	Value	Unit
$V_{1111}, V_{2222}, V_{3333}$	Flexoelectric coefficient	0.08	V
$V_{1122}, V_{1133}, V_{2233}$	Flexoelectric coefficient	2.6	V
$V_{2211}, V_{3311}, V_{3322}$			
$V_{1212}, V_{2323}, V_{1313}$			
$V_{1221}, V_{2332}, V_{1331}$	Flexoelectric coefficient	2.2	V
$V_{2112}, V_{3223}, V_{3113}$			
$V_{2121}, V_{3232}, V_{3131}$			
$G_{1111}^p, G_{2222}^p, G_{3333}^p$	Gradient energy coefficient for \mathbf{p}	7.3266×10^{-11}	$\frac{N \cdot m^4}{C^2}$
$G_{1122}^p, G_{2233}^p, G_{1133}^p$	Gradient energy coefficient for \mathbf{p}	-7.3266×10^{-11}	$\frac{N \cdot m^4}{C^2}$
$G_{2211}^p, G_{3322}^p, G_{3311}^p$			
$G_{1212}^p, G_{2323}^p, G_{1313}^p$			
$G_{1221}^p, G_{2332}^p, G_{1331}^p$	Gradient energy coefficient for \mathbf{p}	7.3266×10^{-11}	$\frac{N \cdot m^4}{C^2}$
$G_{2112}^p, G_{3223}^p, G_{3113}^p$			
$G_{2121}^p, G_{3232}^p, G_{3131}^p$			
$G_{1111}^q, G_{2222}^q, G_{3333}^q$	Gradient energy coefficient for \mathbf{q}	7.3266×10^{-13}	$\frac{N}{m^2}$
$G_{1122}^q, G_{2233}^q, G_{1133}^q$	Gradient energy coefficient for \mathbf{q}	-7.3266×10^{-13}	$\frac{N}{m^2}$
$G_{2211}^q, G_{3322}^q, G_{3311}^q$			

Table 1.2: SrTiO₃ coefficients for phase-field simulation

Name	Meaning	Value	Unit
$G_{1212}^q, G_{2323}^q, G_{1313}^q$			
$G_{1221}^q, G_{2332}^q, G_{1331}^q$	Gradient energy	7.3266×10^{-13}	$\frac{N}{m^2}$
$G_{2112}^q, G_{3223}^q, G_{3113}^q$	coefficient for \mathbf{q}		
$G_{2121}^q, G_{3232}^q, G_{3131}^q$			

¹ We have cubic symmetry for the parent phase, and only non-zero coefficients are listed here. The conversions of tensor to voigt notation, which are also commonly used in other literature [46, 47] are listed below.

² $\gamma_{11} = \gamma_{1111}, \gamma_{12} = \gamma_{1122}, \gamma_{44} = 4\gamma_{1212}$

³ $C_{11} = C_{1111}, C_{12} = C_{1122}, C_{44} = C_{1212}$

⁴ $Q_{11} = Q_{1111}, Q_{12} = Q_{1122}, Q_{44} = 4Q_{1212}$

⁵ $R_{11} = R_{1111}, R_{12} = R_{1122}, R_{44} = 4R_{1212}$

⁶ $V_{11} = V_{1111}, V_{12} = V_{1122}, V_{44} = V_{1212}$

⁷ $G_{11} = G_{1111}, G_{12} = G_{1122}, G_{44} = G_{1212}$

1.3 Background of BiFeO₃

BiFeO₃, bismuth ferrite, is one of the most studied multiferroic materials. It has both ferroelectricity and antiferromagnetism (a cycloidal spin order) [8, 48]. At high temperature (above 1203K), due to the structural instability, it is difficult to determine the crystal structure, thus researchers proposed BiFeO₃ has the cubic perovskite structure of space group Pm $\bar{3}$ m in this range [49]. For temperature between 1093K and 1198K, the high temperature cubic structure transforms into an Pnma orthorhombic paraelectric phase,

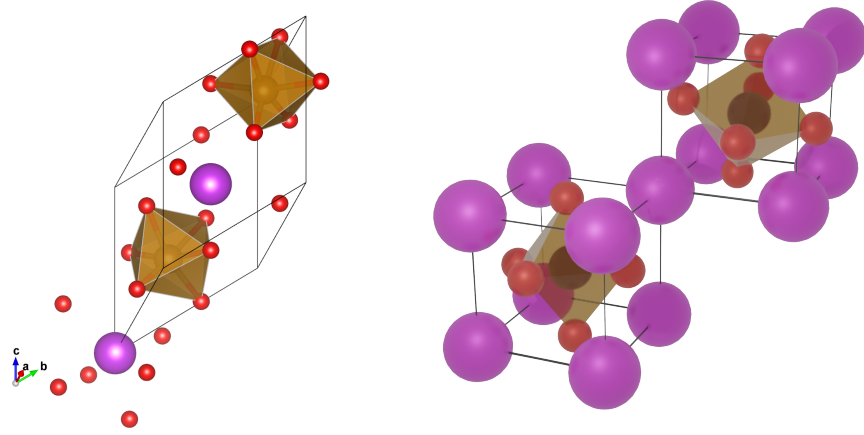


Figure 1.3. The rhombohedral structure of BiFeO_3 with oxygen octahedral tilt. Left, a primitive cell. Right, two pseudocubic cells. Purple spheres are Bi atoms, red spheres are O atoms, and brown spheres are Fe atoms.

which features a $a^-a^-a^+$ oxygen octahedral tilt pattern. At about 1093K, there is a paraelectric to ferroelectric transition, and BiFeO_3 transforms into a rhombohedral structure of $R3c$ space group [50]. At room temperature the lattice parameter of BiFeO_3 is 3.965\AA , and the rhombohedral angle is measured to be 89.3° to 89.4° [51], with polarization of $100\mu\text{C}/\text{cm}^2$ along the body diagonal direction [111] of the pseudocubic lattice. The band gap of BiFeO_3 is calculated to be about 2.3 to 2.8 eV [52], which means BiFeO_3 is much more conductive than SrTiO_3 .

Given the ionic radius of Bi, O and Fe, we can calculate the Goldschmidt tolerance factor $t = \frac{r_{\text{Bi}^{3+}} + r_{\text{O}^{2-}}}{\sqrt{2}(r_{\text{Fe}^{3+}} + r_{\text{O}^{2-}})} = 0.88$. The value is less than 1 meaning the oxygen octahedra chain must buckle to squeeze into the lattice. In BiFeO_3 the calculated octahedra rotation angle along the polar axis is around 11° - 14° [53], And the the Fe-O-Fe angle is about 154° - 156° [54]. According to Glazer [24], the tilt system for BiFeO_3 is $a^-a^-a^-$, similar to the SrTiO_3 case, only out-of-phase components exists, thus three order parameters are enough to describe the oxygen octahedral tilt in BiFeO_3 .

BiFeO_3 is a G-type antiferromagnet (Néel temperature is calculated to be 643 K [55–

57)), which means each Fe^{+3} spin is surrounded by six anti-parallel spins at Fe neighbors. The preferred Fe magnetic moment orientation is perpendicular to the polar [111] direction, and it may exhibit weak magnetism due to the canting of the antiferromagnetic sublattices [58]. The antiferromagnetic spin order is inhomogeneous inside $BiFeO_3$ bulk single crystal, as researchers have found a 62-64 nm periodic, the antiferromagnetic incommensurate spin cycloidal, along [110] direction in bulk system [59,60]. Such a cycloidal structure can be destroyed and transform into a homogeneous state under a large external magnetic field [61], or preparing the sample through epitaxial thin film growth [62]. Besides from the ferroelectric and antiferromagnetic properties, $BiFeO_3$ has some interesting optical properties, for example, it is a photovoltaic material that absorbs near the violet edge of the visible range [63]. $BiFeO_3$ is also a photoelectrolysis that can potentially achieve unassisted water splitting [64].

Similar to $SrTiO_3$, $BiFeO_3$ was first synthesized in the 1950s. In the early days, it was difficult to obtain a single phase $BiFeO_3$, since kinetically many impurity phases, such as $Bi_2Fe_4O_9$, Bi_2O_3 , would also form [65]. It was also very difficult to a grow single crystal, and the $BiFeO_3$ ceramic was too leaky for any practical usage. Thus, back in history, $BiFeO_3$ was not as popular as it is now. The recent surge of interest in $BiFeO_3$ starts from the highly cited work from R. Ramesh et al. in 2003 that huge spontaneous polarization (more than 10 times larger than the previously observed bulk value) was first reported in epitaxial thin film [8]. Then, D. Lebeugle et al. were able to grow single crystal in 2007 and confirm the large polarization found in an epitaxial thin film to be intrinsic [66]. And in the same year, even larger polarization value of $100\mu C/cm^2$ was observed [67].

The capability of growing a high quality epitaxial thin film and the coupling of optical, ferroelectric, magnetic properties at room temperature enable scientists to design and

envision the usage of BiFeO₃ in various multifunctional nano-devices, such as electronics, spintronics, photonics, etc. [48].

1.3.1 Charged defects in BiFeO₃

Several types of charged defects are available in BiFeO₃, among which the most widely studied one is definitely oxygen vacancy. The defect is well known for contributing to the leaky behavior of BiFeO₃ at room temperature as Qi et. al found that Ni²⁺ doped BiFeO₃ becomes more conductive due to the higher level of oxygen vacancies and thus higher density of carrier concentration [68]. Oxygen vacancies also play a major role in the inhibition of BiFeO₃ domain wall movement as the defects can migrate to their stable configuration and form acceptor-oxygen-vacancy dipole pairs. Researchers have found that methods which can prevent the formation of such dipole pairs, such as quenching from above the Curie temperature that freezes the disorder defect state or re-oxidation annealing that dissociates the defect pairs, are able to de-pin the domain wall, thus significantly improve the domain wall mobility and ferroelectric performance [69, 70]. The relationship between oxygen vacancy and fatigue behavior of BiFeO₃ is still under debate. Some claim mobile carriers, such as oxygen vacancies, will stabilize and pin the charged domain walls which lead to a fatigue behavior during multistep 180° switching [71], others claim that the charged domain wall can still be switched under alternating field and it is the charges injected from the electrode that pin the domains and lead to fatigue [72].

The second type of charged defect in BiFeO₃ is the locally charged nonstoichiometric nano-defects. For example, in the Nd, Ti co-doped BiFeO₃, (Bi_{0.85}Nd_{0.15})(Fe_{0.9}Ti_{0.1})O_{0.3}, defects of a single unit cell Nd, O rich rods [73] and planar or stepped antiphase boundaries (APBs) are formed [74]. These defects have a structure of edge sharing BO₆ octahedra,

and a negatively charged defect core that will induce local tetragonally distorted region and thus stabilize a polar state within the originally antiferroelectric matrix [75, 76]. A second example is a planar defect embedded in BiFeO_3 , $\text{Bi}_2\text{FeO}_{6-x}$, which resembles an Aurivillius phase with a single layer of FeO_6 octahedra sandwiched by two layers of Bi_2O_2 . The defect is always perfectly epitaxial along the film growing direction, with no mismatch for the in-plane direction but huge out-of-plane lattice shrinkage compares to the BiFeO_3 matrix. This will induce out-of-plane lattice expansion in the neighboring ferroelectric layer and, thus, enhancement in the magnitude of the polarization. Both the flexoelectric effect due to the strong strain gradient near the defect and the negative charges due to local non-stoichiometry will stabilize a head-to-head charged domain wall [77]. Another example is a planar or stepped defect in un-doped BiFeO_3 that structurally resembles the charged defect in the Nb, Ti co-doped antiferroelectric BiFeO_3 . The stepped units are formed by one pair of Bi atoms alternating with two pairs of Fe atoms, and the planar units (normal vector parallel to $\langle 001 \rangle$) are one pair of Bi atoms alternating with one pair of Fe atoms. There is no mismatch between this type of defect and the BiFeO_3 matrix, but it possesses charges with an estimated charge density of -1.1Cm^{-2} . The negative defect charges will result in a head-to-head charged domain wall configuration [2]. This defect is the one that we are mainly concerned in this dissertation. With the development of thin film growth techniques, researchers are able to roughly control the shape, size, and location of these charged defects [2, 78], and thus a new dimension of defect engineering that will help to manipulate the domain and domain wall structure is awaiting us to explore.

1.3.2 BiFeO_3 parameters for phase-field modeling

Table 1.3: BiFeO₃ coefficients for phase-field simulation

Name	Meaning	Value	Unit
$\alpha_1, \alpha_2, \alpha_3$	Landau coefficient	$4.64385 \times 10^5 \times (T - 1103)$	$\frac{N \cdot m^2}{C^2}$
$\alpha_{11}, \alpha_{22}, \alpha_{33}$	Landau coefficient	2.2905×10^8	$\frac{N \cdot m^6}{C^4}$
$\alpha_{12}, \alpha_{13}, \alpha_{23}$ $\alpha_{21}, \alpha_{32}, \alpha_{31}$	Landau coefficient	3.0636×10^8	$\frac{N \cdot m^6}{C^4}$
$\alpha_{111}, \alpha_{222}, \alpha_{333}$	Landau coefficient	5.9919×10^7	$\frac{N \cdot m^{10}}{C^6}$
$\alpha_{112}, \alpha_{113}, \alpha_{221}$ $\alpha_{223}, \alpha_{331}, \alpha_{332}$	Landau coefficient	-3.3398×10^5	$\frac{N \cdot m^{10}}{C^6}$
$\alpha_{123}, \alpha_{132}, \alpha_{213}$ $\alpha_{231}, \alpha_{321}, \alpha_{312}$	Landau coefficient	-1.7775×10^8	$\frac{N \cdot m^{10}}{C^6}$
$C_{1111}, C_{2222}, C_{3333}$	Elastic stiffness tensor	2.280×10^{11}	$\frac{N}{m^2}$
$C_{1122}, C_{1133}, C_{2233}$ $C_{2211}, C_{3322}, C_{3311}$	Elastic stiffness tensor	1.28×10^{11}	$\frac{N}{m^2}$
$C_{1212}, C_{2323}, C_{1313}$ $C_{1221}, C_{2332}, C_{1331}$ $C_{2112}, C_{3223}, C_{3113}$ $C_{2121}, C_{3232}, C_{3131}$	Elastic stiffness tensor	0.65×10^{11}	$\frac{N}{m^2}$
$Q_{1111}, Q_{2222}, Q_{3333}$	Electrostrictive tensor	0.032	$\frac{m^4}{C^2}$
$Q_{1122}, Q_{1133}, Q_{2233}$ $Q_{2211}, Q_{3311}, Q_{3322}$	Electrostrictive tensor	-0.016	$\frac{m^4}{C^2}$

Table 1.3: BiFeO₃ coefficients for phase-field simulation

Name	Meaning	Value	Unit
$Q_{1212}, Q_{2323}, Q_{1313}$	Electrostrictive tensor	0.010075	$\frac{m^4}{C^2}$
$Q_{1221}, Q_{2332}, Q_{1331}$			
$Q_{2112}, Q_{3223}, Q_{3113}$			
$Q_{2121}, Q_{3232}, Q_{3131}$			
$G_{1111}^p, G_{2222}^p, G_{3333}^p$	Gradient energy coefficient for \mathbf{p}	7.3266×10^{-11}	$\frac{N \cdot m^4}{C^2}$
$G_{1122}^p, G_{2233}^p, G_{1133}^p$	Gradient energy coefficient for \mathbf{p}	-7.3266×10^{-11}	$\frac{N \cdot m^4}{C^2}$
$G_{2211}^p, G_{3322}^p, G_{3311}^p$			
$G_{1212}^p, G_{2323}^p, G_{1313}^p$	Gradient energy coefficient for \mathbf{p}	7.3266×10^{-11}	$\frac{N \cdot m^4}{C^2}$
$G_{1221}^p, G_{2332}^p, G_{1331}^p$			
$G_{2112}^p, G_{3223}^p, G_{3113}^p$			
$G_{2121}^p, G_{3232}^p, G_{3131}^p$			

¹ We have cubic symmetry for the parent phase, and only non-zero coefficients are listed here. The conversions of tensor to voigt notation, which are also commonly used in other literature [79] are listed below.

$$^2 \gamma_{11} = \gamma_{1111}, \gamma_{12} = \gamma_{1122}, \gamma_{44} = 4\gamma_{1212}$$

$$^3 C_{11} = C_{1111}, C_{12} = C_{1122}, C_{44} = C_{1212}$$

$$^4 Q_{11} = Q_{1111}, Q_{12} = Q_{1122}, Q_{44} = 4Q_{1212}$$

$$^5 R_{11} = R_{1111}, R_{12} = R_{1122}, R_{44} = 4R_{1212}$$

$$^6 V_{11} = V_{1111}, V_{12} = V_{1122}, V_{44} = V_{1212}$$

$$^7 G_{11} = G_{1111}, G_{12} = G_{1122}, G_{44} = G_{1212}$$

1.4 Computational method

1.4.1 Phase-field model

Phase-field simulation is a powerful mesoscale computational materials science tool for predicting microstructure evolution. It is suitable for a wide range of materials science phenomenon, including solidification, solid state phase transition, grain growth, dislocation dynamics, crack propagation, metallic insulator transition, superconductor phase transition, ferromagnetic, ferroelectric and ferroelastic domain evolution, etc. The usage of so-called order parameter to describe phase distribution with a continuous diffused description of phase boundaries differentiate phase-field model from many other sharp interface models. In a phase-field model, the interface is tracked automatically as the order parameters evolve, while in other models interfaces are tracked manually which consumes a large portion of the computation time.

Order parameter is the most important concept in phase-field modeling. It is a variable (or a set of variables) that describes how the "phases" are distributed in your simulation system. Such distribution (or "field") of order parameter gives us information about the morphology of the microstructure that we are interested in. Thus obtaining the evolution of the order parameter is equivalent of knowing the whole process of microstructure development. There are two types of order parameters, one is conservative, which means the change of order parameter at any location equals to the net flow into the voxel. This type of order parameter is usually related to mass, thus obey the mass conservation law and is governed by the Cahn-Hilliard diffusion equation, for example, concentration of solutes in the solid solution. The other type is non-conservative, which is governed by the Allen-Cahn type relaxation equation, for example, polarization in ferroelectric and ,

magnetization ferromagnetic materials.

Before we get to the evolution of order parameter, I need to point out that there are two types of phase-field models. The first one uses order parameters with physical meanings, and provides a physical description of the total free energy for the simulation system based on thermodynamics. The governing equation can then be obtained by minimizing the total free energy. The second one uses abstract order parameter whose only purpose is to represent the different phases in the system and to utilize the convenience of automatic interface tracking, thus no free energy function can be provided, and people start the modeling by directly write out the governing equation. Here we will only focus on the first type of phase-field model, since this is the one that our ferroelectric model belongs to.

To get the equilibrium microstructure in our simulation, we need to minimize the total free energy in the whole system. This is a calculus of variations problem that requires performing functional derivative to solve. To be more precise and mathematical, knowing the total free energy functional, $F[\eta(\mathbf{r}), \eta'(\mathbf{r})] = \int_{\Omega} f[\eta(\mathbf{r}), \eta'(\mathbf{r})]d\Omega$, of the order parameter $\eta(\mathbf{r})$, which itself is a function of space, we want to solve for the function (distribution of order parameter $\eta(\mathbf{r})$) that minimize the functional (total free energy F). \mathbf{r} is the coordinate in space, and Ω is the domain of simulation. To obtain the evolution of the order parameters, we can use the gradient descent method, which relates the change of order parameter with respect time to the negative functional derivative of total free energy with respect to order parameter, $\frac{\partial \eta}{\partial t} = -L \frac{\delta F}{\delta \eta}$. The L in this equation is the kinetic coefficient, which controls how fast the system evolves.

Now the problem becomes how we can express the total free energy using the given order parameter. The answer will be completely different from case to case, but we can say for sure there will be at least two parts, one related to the bulk energy and another

one related to the interfacial energy. The bulk energy, also called the Landau free energy, should have multiple minima in the order parameter space, each describing one of the possible stable phases of the system. The interfacial energy is related to the gradient terms of order parameters (these gradient terms are the reason for automatic interface tracking), which we may call them gradient energy. Notice, gradient energy only contributes half of the interfacial energy, the other half comes from the bulk or Landau terms. From now on, we will focus on the ferroelectric materials and discuss the specific free energy terms in our ferroelectric phase-field model. [46, 47, 80–84].

The total free energy of ferroelectric includes the following four parts, Landau, gradient, mechanical and electrical. There are a total of six order parameters in our model, three for polarization vector $\mathbf{p} = (p_1, p_2, p_3)$, usually on the order of $0.1 \sim 1C/m^2$, and the other three for oxygen octahedral tilt $\mathbf{q} = (q_1, q_2, q_3)$, usually on the order of $10^{-12} \sim 10^{-11}m$. The total free energy function will be $F(\mathbf{p}(\mathbf{r}), \mathbf{q}(\mathbf{r}), \mathbf{p}'(\mathbf{r}), \mathbf{q}'(\mathbf{r}), \boldsymbol{\epsilon}, \mathbf{E}) = \int_{\Omega} (f_{land}(\mathbf{p}, \mathbf{q}) + f_{grad}(\mathbf{p}', \mathbf{q}') + f_{elas}(\mathbf{p}, \mathbf{q}, \boldsymbol{\epsilon}) + f_{flex}(\mathbf{p}, \mathbf{p}', \boldsymbol{\epsilon}, \boldsymbol{\epsilon}') + f_{elec}(\mathbf{p}, \mathbf{q}, \mathbf{E}))d\Omega$. All lower case f is the energy density and Ω is the volume of 3D simulation space. Details for each term will be explained below.

The Landau free energy, equation (1.4), contain three parts, the polarization terms, the oxygen octahedral tilt terms, and the coupling terms between \mathbf{p} and \mathbf{q} , all of which has a simple polynomial form. The polarization and oxygen octahedral tilt parts are even powered terms because due to symmetry, positive and negative order parameters states should be degenerated. The highest order of the Landau free energy is determined by the materials and the physics problems we are simulating, for example, first order phase transition must have at least 6th order terms, while for second order phase transition the minimum rank is 4. α, β, γ are the landau coefficients for polarization, oxygen octahedral

rotation and coupling terms between \mathbf{p} and \mathbf{q} , respectively.

The subscript i, j, k, l in the following equations represent ranks of the tensor which is related to the dimension of the simulation domain, thus in our 3D simulation they can take values of 1, 2, 3. These equations are written in the Einstein notation, also known as the Einstein summation convention. The rule is as follows, whenever an index appears twice, a summation of all possible value for that terms is performed. The full form of the equations can be found in the numerical method part, Section 1.4.2.

The gradient energy, equation (1.8), contains \mathbf{p}' terms for the polarization domain wall, and \mathbf{q}' terms for the oxygen octahedral tilt domain wall. Similar to the Landau energy, only even power terms exists, since the wall from lower to higher order parameter and the wall from higher to lower order parameter must have the same amount of energy.

The electric energy, equation (1.5), is the electrostatic potential energy. κ here is the relative dielectric constant, \mathbf{E} in these equations is the electric field including contribution from both external applied field and depolarization field. The electric field can be calculated by solving the Poisson equation (1.10). The right hand side of Poisson equation is negative of local charge density, through which the bound charge due to polarization is considered. Equation (1.12) shows how we can consider the defect charges that in this dissertation comes from two sources, first due to non-stoichiometry at dislocation cores in SrTiO_3 , and second, due to non-stoichiometric nanoregions (NSNRs) in BiFeO_3 . More details are discussed in the corresponding chapters.

The flexoelectric effect is the phenomena that strain gradient will contribute to the final polarization distribution within the material. The flexoelectric coefficient, \mathbf{V} , is a 4th rank tensor which means it is allow to exist in materials of any point group by symmetry. This is similar to the electrostriction, which is also described by a 4th rank

tensor, and in contrast to the piezoelectric effect, which is a 3rd rank tensor that is only allowed by symmetry in the 21 non-centrosymmetric point groups. The flexoelectric energy, equation (1.7), couples the strain gradient with polarization and polarization gradient with strain. Notice the strain ϵ here is the total strain of the system, including both the elastic strain and eigenstrain. Please refer to these references [83, 85] for more details of why the flexoelectric energy is in such formation.

For the elastic energy, equation (1.6), ϵ is the total strain, ϵ^0 is the eigenstrain also known as the stress free strain. The total strain can be obtained by solving the mechanical equilibrium equation (1.9). The eigenstrain, ϵ^0 , has multiple source. There is the electrostrictive contribution $Q_{ijkl}p_k p_l$, the rotostrictive contribution $R_{ijkl}q_k q_l$, the flexoelectric contribution $v_{ijkl}p_{k,l}$, and the defect (dislocation) contribution $\frac{1}{2d_0}(b_i n_j + b_j n_i)$. v here is the reverse flexoelectric strain coefficient that $v_{ijkl} = S_{ijmn}V_{mnkl}$ where S_{ijmn} is the elastic compliance. b is the burgers vector of our studied dislocation, and n is the normal direction of slip plane. Please refer to these references for more details on the phase-field model of dislocations.

By solving the equations (1.2, 1.10 and 1.9) together, we can get the evolution of polarization and oxygen octahedral tilt domain structure, along with the strain/stress, electric potential distribution, etc.

$$\frac{\partial \eta}{\partial t} = -L \frac{\delta F}{\delta \eta} \quad (1.2)$$

$$F = \int_{\Omega} (f_{land} + f_{elec} + f_{elas} + f_{flex} + f_{grad}) d\Omega \quad (1.3)$$

$$f_{land}(\mathbf{p}, \mathbf{q}) = \alpha_i p_i^2 + \alpha_{ij} p_i^2 p_j^2 + \beta_i q_i^2 + \beta_{ij} q_i^2 q_j^2 + \gamma_{ijkl} p_i p_j q_k q_l \quad (1.4)$$

$$f_{elec}(\mathbf{p}, \mathbf{E}) = -\frac{1}{2} E_i \epsilon_0 \kappa_{ij} E_j - E_i p_i \quad (1.5)$$

$$f_{elas}(\mathbf{p}, \mathbf{q}, \boldsymbol{\epsilon}) = \frac{1}{2} C_{ijkl} (\epsilon_{ij} - \epsilon_{ij}^0) (\epsilon_{kl} - \epsilon_{kl}^0) \quad (1.6)$$

$$f_{flexo}(\mathbf{p}, \boldsymbol{\epsilon}) = \frac{1}{2} V_{ijkl} \left(\frac{\partial p_k}{\partial x_l} \epsilon_{ij} - \frac{\partial \epsilon_{ij}}{\partial x_l} p_k \right) \quad (1.7)$$

$$f_{grad}(\mathbf{p}) = \frac{1}{2} G_{ijkl}^p p_{i,j} p_{k,l} + \frac{1}{2} G_{ijkl}^q q_{i,j} q_{k,l} \quad (1.8)$$

$$C_{ijkl} (\epsilon_{kl,j} - \epsilon_{kl,j}^0) = 0 \quad (1.9)$$

$$\epsilon_0 \kappa_{ii} \phi_{,ii} = -\rho \quad (1.10)$$

$$\epsilon_{ij}^0 = Q_{ijkl} p_k p_l + R_{ijkl} q_k q_l - v_{ijkl} p_{k,l} + \frac{1}{2d_0} (b_i n_j + b_j n_i) \quad (1.11)$$

$$\rho = -p_{i,i} + \rho_{defect} \quad (1.12)$$

1.4.2 Numerical method of the phase-field model for ferroelectric

In the previous section, we explained all of the necessary equations that make up our phase-field model for ferroelectrics. In this section, we will discuss how to solve the problem numerically.

First thing is to calculate the driving force for order parameters, which is the negative of the functional derivative for energy density, $df^\eta = -\frac{\delta f}{\delta \eta}$, plug it back into equation (1.2) so that we can obtain the actual PDE that we are solving.

Landau driving force

$$\begin{aligned} df_{land}^{p_i} &= -2\alpha_1 p_i - 4\alpha_{11} p_i^3 - 2\alpha_{12} p_i p_j p_j \\ df_{land}^{q_i} &= -2\beta_1 q_i - 4\beta_{11} q_i^3 - 2\beta_{12} q_i q_j q_j \end{aligned} \quad (1.13)$$

The electric driving force is simply electric field. $df_{elec}^{p_1} = E_1$, $df_{elec}^{p_2} = E_2$, $df_{elec}^{p_3} = E_3$.

The elastic driving force is $-2C_{ijkl} (\epsilon_{ij} - \epsilon_{ij}^0) Q_{klmn} p_n$ and $-2C_{ijkl} (\epsilon_{ij} - \epsilon_{ij}^0) R_{klmn} q_n$ for polarization and oxygen octahedral tilt respectively. It is tedious and unnecessary

to write out every terms, since we can use several nested for loops to easily calculate the summation of repeating indices, thus the elastic driving force can be simplified as equation (1.14).

$$\begin{bmatrix} A^p \\ 3 \times 3 \end{bmatrix} = \begin{bmatrix} C \\ 3 \times 3 \times 3 \times 3 \end{bmatrix} \begin{bmatrix} Q \\ 3 \times 3 \times 3 \times 3 \end{bmatrix} \begin{bmatrix} \epsilon - \epsilon^0 \\ 3 \times 3 \end{bmatrix} \quad (1.14)$$

$$\begin{bmatrix} A^q \\ 3 \times 3 \end{bmatrix} = \begin{bmatrix} C \\ 3 \times 3 \times 3 \times 3 \end{bmatrix} \begin{bmatrix} R \\ 3 \times 3 \times 3 \times 3 \end{bmatrix} \begin{bmatrix} \epsilon - \epsilon^0 \\ 3 \times 3 \end{bmatrix} \quad (1.15)$$

$$\begin{aligned} df_{elas}^{p_i} &= -2A_{ij}^p p_j \\ df_{elas}^{q_i} &= -2A_{ij}^q q_j \end{aligned} \quad (1.16)$$

Since the flexoelectric energy terms involve polarization gradient, we need to use the Euler-Lagrange equation to calculate the flexoelectric driving force.

$$\frac{\delta f_{flex}}{\delta p_i} = \frac{\partial f_{flex}}{\partial p_i} - \frac{\partial}{\partial x_j} \left(\frac{\partial f_{flex}}{\partial p_{i,j}} \right) = -V_{ijkl} \epsilon_{kl,j} \quad (1.17)$$

$$\rightarrow df_{flex}^{p_i} = V_{ijkl} \frac{\partial \epsilon_{kl}}{\partial x_j} \quad (1.18)$$

For the gradient driving force term, similar to the flexoelectric part, we also need to use the Euler-Lagrange equation.

$$\frac{\delta f_{grad}}{\delta p_i} = \frac{\partial f_{grad}}{\partial p_i} - \frac{\partial}{\partial x_j} \left(\frac{\partial f_{grad}}{\partial p_{i,j}} \right) = -G_{ijkl}^p p_{k,lj} \quad (1.19)$$

$$\frac{\delta f_{grad}}{\delta q_i} = \frac{\partial f_{grad}}{\partial q_i} - \frac{\partial}{\partial x_j} \left(\frac{\partial f_{grad}}{\partial q_{i,j}} \right) = -G_{ijkl}^q q_{k,lj} \quad (1.20)$$

So now the TDGL becomes

$$\frac{\partial p_i}{\partial t} = LG_{ijkl}^p p_{k,lj} + L(df_{land}^{p_i} + df_{elec}^{p_i} + df_{elas}^{p_i} + df_{flex}^{p_i}) \quad (1.21)$$

$$\frac{\partial q_i}{\partial t} = LG_{ijkl}^q q_{k,lj} + L(df_{land}^{q_i} + df_{elas}^{q_i}) \quad (1.22)$$

The flow chart, Figure (1.4), illustrate the procedure of our program. From the driving force equations above, we know that the elastic driving force and flexoelectric driving force depends on the strain distribution, and the electric driving force depends on the electrical potential distribution. Thus, we need to solve the mechanical equilibrium equation and Poisson equation before we can calculate those driving forces. Please see the appendix for more details of solving the mechanical equilibrium and the Poisson equation under various boundary conditions using fourier spectral method. Here we will only discuss how the last step, solving TDGL is been done.

Equation (1.21) and (1.22) are the time dependent PDEs for ferroelectric phase-field model that we are trying to solve. The method that we are using is call semi-implicit Fourier spectral method.

Semi-implicit is the numerical algorithm that we are using to transform the time dependent PDE into an iterative form. Other algorithms are explicit method, which treats all of the order parameters on the right hand side of equation (1.21, 1.22) as known value from previous time step, and implicit method, which treats all of the order parameters on the right hand side as unknown value from current time step. Explicit method is simple and fast, but not very stable and suffers from small time step size. Implicit method has better stability, larger time step, but more difficult to solve, especially when there is non-linear terms involved. Semi-implicit method treats part of the right hand side from current time step (the gradient energy related terms), and rest of the terms as from

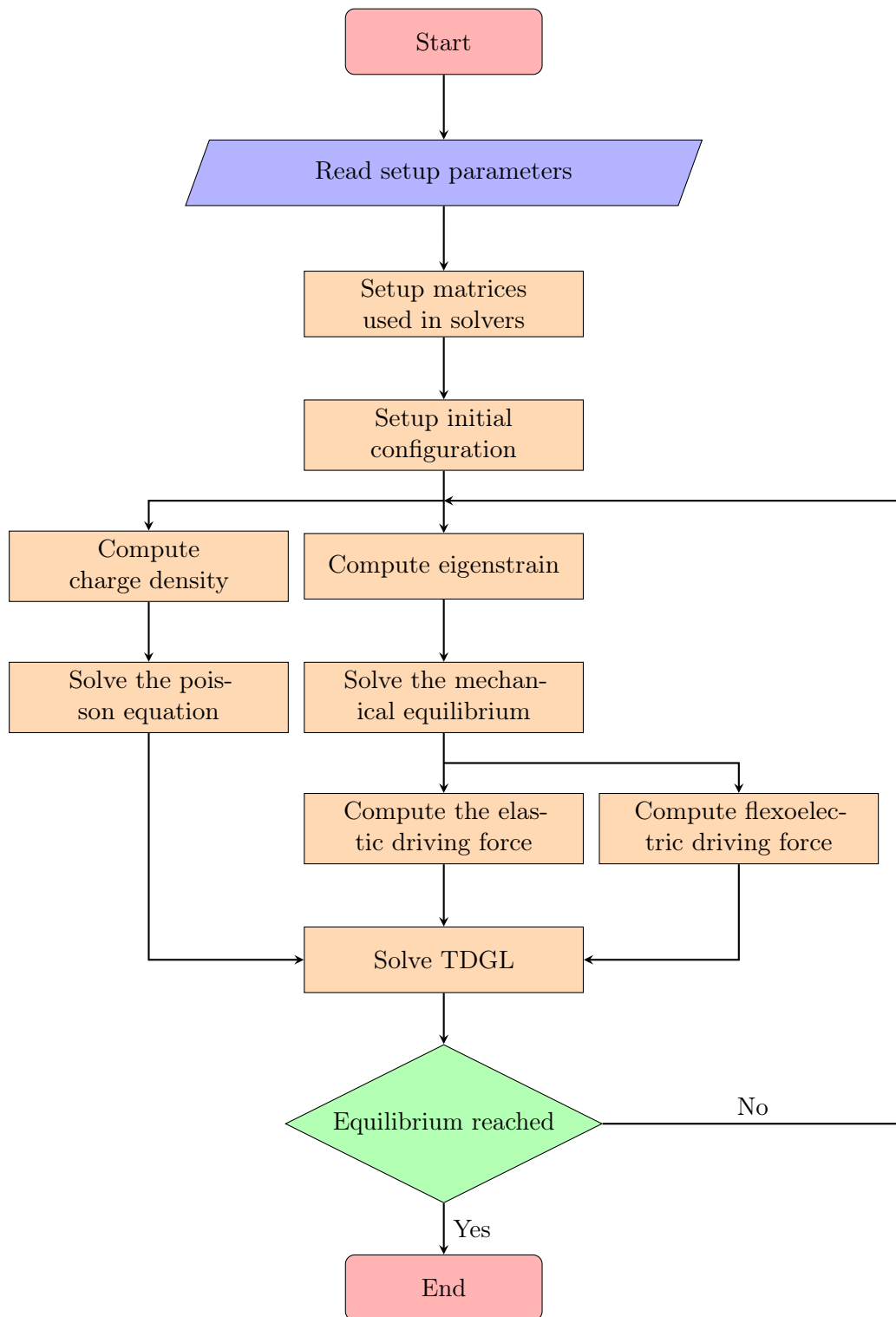


Figure 1.4. Flowchart of the phase-field program

the previous time step. Applying the semi-implicit method, gives us the set of equations

(1.23)

$$\begin{cases} p_1^{n+1} - L\Delta t(G_{1j1l}p_{1,lj}^{n+1} + G_{1j2l}p_{2,lj}^{n+1} + G_{1j3l}p_{3,lj}^{n+1}) = p_1^n + L\Delta tdf^{p_1^n} \\ p_2^{n+1} - L\Delta t(G_{2j1l}p_{1,lj}^{n+1} + G_{2j2l}p_{2,lj}^{n+1} + G_{2j3l}p_{3,lj}^{n+1}) = p_2^n + L\Delta tdf^{p_2^n} \\ p_3^{n+1} - L\Delta t(G_{3j1l}p_{1,lj}^{n+1} + G_{3j2l}p_{2,lj}^{n+1} + G_{3j3l}p_{3,lj}^{n+1}) = p_3^n + L\Delta tdf^{p_3^n} \end{cases} \quad (1.23)$$

Fourier spectral method is the solver that we are using to solve the equation at each time step. Other methods include, finite element method, finite difference method, finite volume method, etc. Often, people may misunderstand finite element as a simulation method similar to phase-field, but at a larger length scale. Finite element is a mathematical solver for PDE regardless of the scale, and phase-field is a physics based theoretical model which will utilize solvers such as fourier spectral method and finite element method to obtain the solution. The benefit of spectral solver over finite element is its efficiency, since fourier transform is a $O(N\log N)$ algorithm, while finite element is a $O(N^3)$ algorithm. On the other hand, the advantage of finite element compared to fourier spectral method is the scalability, as the communication overhead of fast fourier transform is higher than finite element in parallel computing.

Performing fourier transform to equations (1.23), we will get equations (1.24), from which we can obtain the solution of \mathbf{p} in reciprocal space by multiplying the inverse matrix, and thus the final solution of polarization distribution in real space after a backward fourier transformation.

$$\rightarrow \begin{bmatrix} 1 + \xi_j \xi_l L \Delta t G_{1j1l} & \xi_j \xi_l L \Delta t G_{1j2l} & \xi_j \xi_l L \Delta t G_{1j3l} \\ \xi_j \xi_l L \Delta t G_{1j1l} & 1 + \xi_j \xi_l L \Delta t G_{1j2l} & \xi_j \xi_l L \Delta t G_{1j3l} \\ \xi_j \xi_l L \Delta t G_{1j1l} & \xi_j \xi_l L \Delta t G_{1j2l} & 1 + \xi_j \xi_l L \Delta t G_{1j3l} \end{bmatrix} \begin{bmatrix} \tilde{p}_1^{n+1} \\ \tilde{p}_2^{n+1} \\ \tilde{p}_3^{n+1} \end{bmatrix} = \begin{bmatrix} \tilde{p}_1^n \\ \tilde{p}_2^n \\ \tilde{p}_3^n \end{bmatrix} + L \Delta t \begin{bmatrix} \tilde{d}f^{p_1^n} \\ \tilde{d}f^{p_2^n} \\ \tilde{d}f^{p_3^n} \end{bmatrix} \quad (1.24)$$

As shown in Figure 1.4, we need to repeat the solving procedures above to push the simulation system down the total free energy hill to an energy minima, in other word to evolve order parameter and obtain the equilibrium state.

1.5 Objectives

As discussed in the previous sections, domain engineering is crucial for ferroelectrics in real applications, and understanding the role of defects in polarization domain pattern formation of ferroelectrics is an essential task for designing the domain or domain wall microstructures and predicting the ferroelectric thin film properties. However, in the experiment, it is impossible to have full control over the experimental conditions, such as defect density, geometry, location, dimension, etc. On the other hand, the defects are not only interacting with the local polarization but also with each other and the external electric or mechanic excitation. Every complication related to domain pattern formation is unavoidably included, such as the flexoelectric contribution, the electric contribution, the electrostrictive contribution, defect distribution, the surface compensation, charge injection, oxygen vacancies, etc. It would be challenging to elucidate the effect of each defect since what we can measure and characterize in the sample is an effective value considering all the above-mentioned complexity of the system. The power of computer simulation based on the phase-field model is clearly demonstrated here that we have full control over the defect

configurations, and we are capable of isolation contribution from individual free energy terms. A detailed description of the single defect effect is important because it would allow us to identify which types of defects undermine the properties and what configurations are most suitable for stabilizing a specific type of domain patterns. The main objective of this dissertation is to develop a theoretical model and study the polarization defect interaction in ferroelectric materials from a simulation point of view to understand the details of how the defect is affecting domain structure and to provide guidance to the defect engineering for nanoscale domain engineering. We focus on two types of defects, the dislocation in SrTiO₃ and nonstoichiometric charged defect in BiFeO₃ as the example systems to be studied in this dissertation. The flexoelectric, electrostrictive, and electric contributions to the local and long-range most stable polarization distribution are investigated within our current ferroelectric phase-field model as described previously. However, the defect dynamics, such as dislocation dynamics and oxygen vacancies migration, and the defect's interaction with each other, are not studied in this work.

The detailed objectives of this dissertation are as follows:

1. Investigate and compare the role of electrostrictive and flexoelectric effects on stabilizing local polarizations in vicinity of $b = a(100)$ edge dislocation, $b = \frac{a}{2}(110)$ edge dislocation, $b = a(010)$ screw dislocation cores in SrTiO₃.
2. Investigate the influence of defect charges on the local polarization pattern around the three types of dislocations core, $b = a(100)$ edge dislocation, $b = \frac{a}{2}(110)$ edge dislocation, $b = a(010)$ screw dislocation, in SrTiO₃.
3. Explore the identify configurations of the nonstoichiometric charged nano defects in BiFeO₃ that stabilize 71° domain patterns.

4. Explore the identify configurations of the nonstoichiometric charged nano defects in BiFeO_3 that stabilize 109° domain walls.

1.6 Dissertation structure

The objectives are addressed through four chapters, from chapter two to chapter five, in this dissertation.

In Chapter 2 and 3, we set up ferroelectric phase-field simulations for SrTiO_3 as described in Chapter 1 with the presence of three types of dislocations, $b = a(100)$ edge dislocation, $b = \frac{a}{2}(110)$ edge dislocation, $b = a(010)$ screw dislocation, and considering both the energy contribution from oxygen octahedral tilt and flexoelectricity. First, we focus on investigating the elastic effect of dislocation, which is studying how the electrostrictive and flexoelectric effect due to the specific stress distribution around each type of dislocation cores would affect the local polarization distribution. It is shown that in the two edge dislocation cases, the flexoelectric contribution dominates and leads to a mirrored polarization pattern with respect to the dislocation, while in the screw dislocation case, neither electrostriction nor flexoelectricity has any influence on the surrounding polarization. Then, we introduce an experimentally estimated amount of defect charges at the three dislocation cores to consider the electric contribution of dislocations to the locally induced polarization. Through the comparison with the elastic effects, we learn that the defect charges lead to a smaller impacting region than the elastic effect, but a larger polarization value at the dislocation core.

In Chapter 4 and 5, we study the second type of defect, the nonstoichiometric charged defect in BiFeO_3 , and focus on how it may interact with the thin film BiFeO_3 to stabilize 781° and 109° domain and domain walls. This defect has no lattice mismatch with the

matrix, but it is charged due to the crystal structure. First, we explore the influence of defect configurations, including defect width, height, and interval, on the stabilization of 71° domain patterns. We find a criterion that can determine whether a specific defect configuration favors a single domain state or 71° strips state above the defect. Next, we reduce the defect dimension down to around 10 nm and incorporate additional parameters, including defect charge distribution, initial domain structure, defect shape, and electric boundary condition, to find the defect and thin film configurations that can stabilize and control the location of the 109° domain wall. We find that a neutrally charged defect (half negative, half positive) that is larger than 3.2 nm within a short circuit thin film is the optimum setup to achieve our goal.

In Chapter 6, conclusion of this work is summarized and possible directions for future works, which I discussed interesting topics to continue down the route of my simulations. And finally, there is an appendix, in which I derive in great detail of different elastic solvers for several different boundary conditions using the Fourier spectral method.

Chapter 2 |

Role of flexoelectric effect on polarization around dislocation in SrTiO₃

2.1 Introduction

SrTiO₃ is a quantum paraelectric, which structurally transform from cubic to tetragonal at 105K (antiferrodistortive transition), and the transverse optical mode softens near 0k while no ferroelectric transition can be observed [22, 25, 30, 86]. There is a long-standing interest in creating and stabilizing ferroelectric polarity in non-polar crystals such as SrTiO₃. Researchers have managed to find multiple ways to introduce ferroelectricity into the normally paraelectric SrTiO₃ at room temperature, such as non-stoichiometry [87, 88], thin film strain engineering [37, 89, 90], isotope [91], etc. Recently, measurable electrical polarization as large as $\sim 28\mu\text{C}/\text{cm}^2$ has been reported at the dislocation cores in SrTiO₃ bicrystals [1].

Flexoelectricity, which is the coupling between polarization and strain gradient, indicates that polarization can be induced deterministically given a strain gradient [92–94]. As a 4_{th} rank tensor, flexoelectricity is presented in all symmetry, in contrast to piezoelectricity which is absent in central-symmetric materials. Though universal, only in materials of large dielectric permittivity, the flexoelectric coupling coefficient will be large enough to result in observable polarization changes due to the strain gradient [85, 94–97]. The locally distorted region around dislocation core in dielectric material, such as SrTiO₃ is definitely a spot that flexoelectricity will play an important role. And since SrTiO₃ is not a ferroelectric material, at least it rules out the contribution to polarization from piezoelectricity. However, at this point, we cannot conclude that flexoelectricity determines the polarization pattern around a dislocation core, because based on our prior simulations [80], and literature results [98] a pure electrostrictive effect can also stabilize ferroelectric phases. Unfortunately, it is impossible to explicitly identify the contribution to polarization from the two effects through experiments. Thus in this work, we used phase-field simulation to investigate the flexoelectric and electrostrictive influence on polarization around dislocations in SrTiO₃. Our phase-field ferroelectric model provides a self-consistent way to isolate each of the flexoelectric coefficients that enables us to identify and compare the effect for each one of them.

It is worth noting that dislocation in SrTiO₃ itself is a complex topic [99]. It has rich physical phenomena, that can significantly influence the material’s properties [99]. For example, the interaction of dislocation cores with oxygen vacancies that leads to resistive switching [100–102], the stabilization of local polarization [1], the dislocation reactions and dynamics [3, 103, 104], and etc. In this work, we focused on the mechanical effect of three common types of dislocations, $b = a(100)$ edge dislocation, which is widely seen at small

angle grain boundary [1, 102] or in plastic deformation at high temperature [105, 106], $b = \frac{a}{2}(110)$ edge dislocation, and $b = a(010)$ screw dislocation, which can be observed in SrTiO₃ that undergoes plastic deformation at low temperature [42, 105, 106]. For the $b = a(100)$ edge dislocation, the atomic and electronic structure has been characterized using the modern high-resolution STEM and EELS, which gives us information including polarization, local charges, and strain mapping [1, 102]. For the $b = \frac{a}{2}(110)$ edge dislocation and $b = a(010)$ screw dislocation, no atomic resolution experimental data is available. Thus, our phase-field ferroelectric simulation will be useful for understanding the polarization distribution and role of flexoelectricity around $b = a(100)$ edge dislocation and predicting the polarization arrangement in $b = \frac{a}{2}(110)$ edge dislocation and $b = a(010)$ screw dislocation. For a fair comparison between the three types of dislocations, only one single dislocation is introduced in all cases. In real world, however, $b = \frac{a}{2}(110)$ edge dislocation always comes in pairs, but that is beyond the discussion of this dissertation, and will be addressed in our future researches.

We systematically study the role of flexoelectricity on inducing polarization around three types of dislocation cores in SrTiO₃, $b = a(100)$ edge dislocation, $b = \frac{a}{2}(110)$ edge dislocation, and $b = a(010)$ screw dislocation. We demonstrate that, in both edge dislocation cases, flexoelectricity has a significant influence on both the polarization's magnitude and distribution. It increases the average polarization value and forces the polarization into a symmetric distribution. For $b = a(100)$ edge dislocations, the ferroelectric phase is mainly tetragonal and can exist even without flexoelectricity and rely on purely the electrostrictive effect. For $b = \frac{a}{2}(110)$ edge dislocations, electrostriction alone is not sufficient to stabilize the ferroelectric phases, and flexoelectricity is essential for the presence of orthorhombic polarization in this case. Moreover, through tuning of the three

flexoelectric coefficients, we recognize the shear flexoelectric coefficient V_{1212} to have the largest effect on the stable polarization pattern and magnitude for both types of edge dislocations. In contrast, in the $b = a(010)$ screw dislocation cases, we learn that neither electrostriction nor flexoelectricity will be able to stabilize any polar state in SrTiO₃. Our findings provide an in-depth understanding of the flexoelectric effects on the induced polarization around three dislocation cores which may potentially bring new insights into the defect engineering of ferroic materials using dislocations.

2.2 Materials and Methods

Phase-field method, a phenomenological diffused interface model, is employed to simulate the polarization distribution of bulk SrTiO₃ with the presence of dislocation [80, 81]. The temporal evolution of local polarization and oxygen octahedral tilt can be described by the time-dependent Ginzburg Landau equation (1.2) for two sets of order parameters P, polarization, and Q, oxygen octahedral tilt. Detail forms for each free energy term is shown in Einstein notation in the introduction chapter from Equation 1.4 to 1.8.

A self consistent distribution of order parameters can be obtained by solving the TDGL equation (1.2), mechanical equilibrium equation (S1.9), and Poisson equation (1.10) together. All of the coefficients that we used are listed in the Chapter 1 table (1.2).

The mechanical effect of dislocation is considered through the introduction of additional dislocation eigenstrain into the system. The eigenstrain can be expressed as $\epsilon_{ij}^{dis} = b_i n_j$, where b is the Burgers vector, n is the unit vector normal of the dislocation half plane [82]. In our simulation instead of a δ function, the Burgers vector is treated as a diffused value to avoid numerical issues. We applied a normal distribution with variance equals to 0.5 around the dislocation loop. In this work, three types of dislocations are considered, an

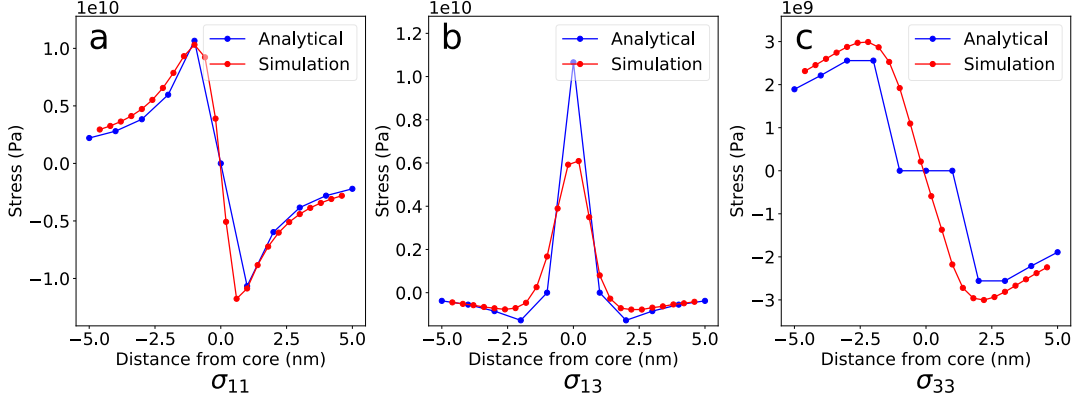


Figure 2.1. Comparison of stress distribution around (100) dislocation core between analytical and simulation results. All data in comparison are taken from the stress profile along a line 1 nm to the right of the dislocation core. (a), σ_{11} (b), σ_{13} (c) σ_{33} . Subscript 1 means the horizontal x direction. 2 means the y direction that goes into the paper which is invisible. 3 means the vertical z direction.

edge dislocation $b = a(100), n = (100)$, a partial edge dislocation $b = \frac{a}{2}(110), n = \frac{1}{\sqrt{2}}(110)$, and a screw dislocation $b = a(010), n = (100)$.

To demonstrate our model correctly capture the stress distribution around dislocation core, we compared our simulation result with the analytical solutions, as shown in Figure S2.1.

The flexoelectric effect is considered through the introduction of f_{flexo} term in the total free energy and an additional converse flexoelectric term for calculating eigenstrain [83,84]. We can make an analogy between electric field and flexoelectric field, which can be calculated using the expression $V_{ijkl} \frac{\partial \epsilon_{kl}}{\partial x_j}$. The flexoelectric field distribution is an important result that will help us to understand the role of flexoelectricity in affecting polarization. SrTiO₃ at room temperature has cubic symmetry, thus only 21 non-zero coefficients survive, with three independent values, $V_{1111}, V_{1122}, V_{1212}$. We must be aware that even though flexoelectric coefficient is a 4th rank tensor, it is different from other more commonly seen 4th rank tensor, such as electrostrictive tensor, since the first two indices of flexoelectric tensor are not commutable, which will lead to more independent variables within the

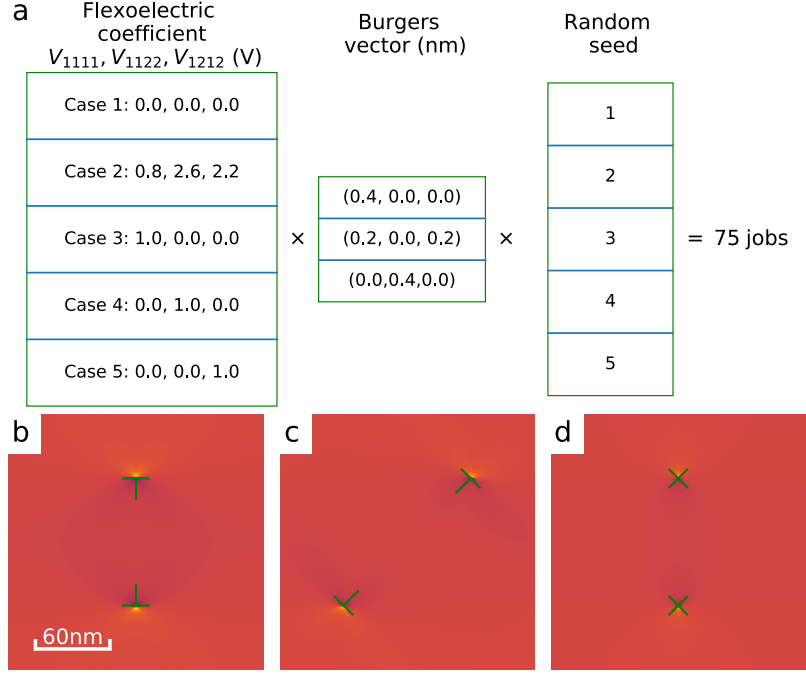


Figure 2.2. The simulation setup. (a) A total of 75 jobs, with 5 sets of flexoelectric coefficient, 3 sets of Burgers vector, and 5 different random seeds, are calculated. (b) The (100) edge dislocation setup, (c) (110) partial edge dislocation setup. (d) (010) screw dislocation setup.

tensor after symmetry analysis. It is coincidental that for cubic system, the amount of independent variables happens to be the same for flexoelectric coefficient and other 4th rank tensors.

3D bulk simulation of $512 \times 1 \times 512$ grids (0.4 nm per grid) with periodic conditions and stress-free boundary condition is set up. One pair of edge dislocations of opposite Burgers vector are placed inside the simulation system, which form a closure inclusion plane for dislocation so that the periodic boundary condition is fulfilled. In this work, we have three groups of simulations. In two of them, $b = a(100)$ edge dislocation (Figure 2.2(b)) and $b = a(010)$ screw dislocation (Figure 2.2(d)), the two dislocations are put at $\frac{1}{4}$ and $\frac{3}{4}$ of the vertical center line. The third type of dislocation is $b = \frac{a}{2}(110)$ edge dislocation (Figure 2.2(c)), that the two dislocations are at $\frac{1}{4}$ and $\frac{3}{4}$ of the diagonal line. The distance between the two imaging dislocations are 102.4 nm and 144.8 nm respectively,

which should be enough to eliminate the interaction between each other. Besides from the comparison between no-flexoelectricity and with-flexoelectricity (using experimentally measured coefficients, $V_{1111} = 0.08(V)$, $V_{1122} = 2.6(V)$, $V_{1212} = 2.2(V)$ [85, 107]) to demonstrate and explain the flexoelectric effect of edge dislocations, we also isolate each of the independent flexoelectric coefficients and studied their individual's effect because the value for the flexoelectric coefficient is a controversial topic. There exists a huge discrepancy between experimental measurements and theoretical calculations. So in the future, even if more accurate measurement or calculation shows that the flexoelectric coefficients of SrTiO_3 are different from what we are using in this work, our data should still be meaningful to the community.

2.3 Results and Discussion

The stress distribution and strain gradient distribution around $b = a(100)$ edge dislocation is shown in Figure 2.3. σ_{11} has the largest magnitude because it is directly affected by the eigenstrain distribution due to the additional atomic plane inside the dislocation loop. Electrostriction, as a quadruple relationship between polarization and strain, can affect the shape of total free energy in Equation 1.3 and thus the equilibrium polarization value [108]. This is illustrated in Figure 2.4 that tensile stress will favor the ferroelectric phase along the tensile direction and compressive stress still favors the paraelectric phase (not large enough to stabilize the ferroelectric state). As a result, polarization will be suppressed inside the compressive stress region and enhanced inside the tensile stress region.

The flexoelectric effect, on the other hand, correlates polarization's orientation to the strain gradient, which breaks the central symmetry and stabilize the ferroelectric phases

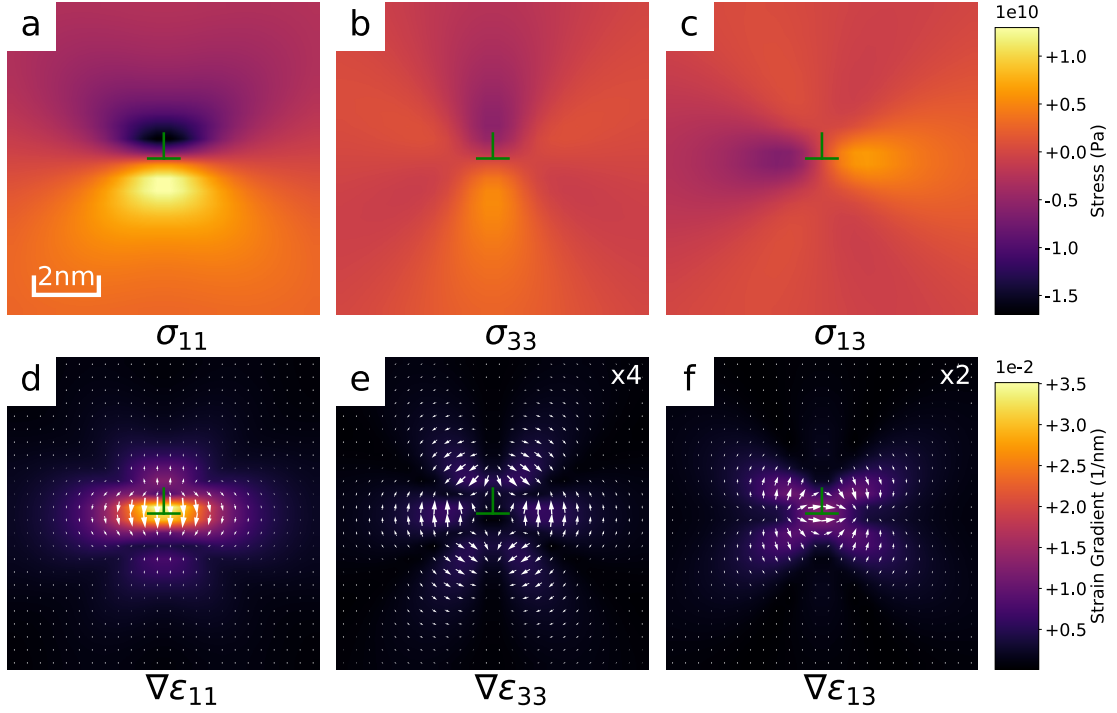


Figure 2.3. Stress and strain gradient distribution around $b = a(100)$ edge dislocation core. (a) σ_{11} , (b) σ_{33} , (c) σ_{13} , (d) $\nabla\epsilon_{11}$, (e) $\nabla\epsilon_{33}$, (f) $\nabla\epsilon_{13}$. Subscript 1 means the horizontal axis to the right, subscript 3 means the vertical axis to the up, and 2 is the axis goes into the paper plane. Dislocation core is located at the center of the region labeled by the green marker.

directly. The strain gradient distributions in Figure 2.3(d), (e), and (f), show that gradient of ϵ_{11} and ϵ_{33} are mainly along (001) direction while ϵ_{13} gradient is along (100) direction. The ϵ_{11} gradient has the largest magnitude, nearly 3 times of ϵ_{33} and ϵ_{13} gradient. To activate the flexoelectric effect, significant strain gradient and large flexoelectric coefficient are the two necessities.

For a qualitative understanding of the contribution to the flexoelectric field from each of the strain gradient, we multiply the maximum value of each strain gradient with the corresponding flexoelectric coefficient and calculate the value of each flexoelectric field component according to the following equations, $E_1^{flexo} = V_{1111}\epsilon_{11,1} + V_{1133}\epsilon_{33,1} + 2V_{1313}\epsilon_{13,3}$, and $E_3^{flexo} = V_{3333}\epsilon_{33,3} + V_{3311}\epsilon_{11,3} + 2V_{3113}\epsilon_{13,1}$. The results are shown in Figure 2.5. The area of the shapes in Figure 2.5 is proportional to the magnitude of the

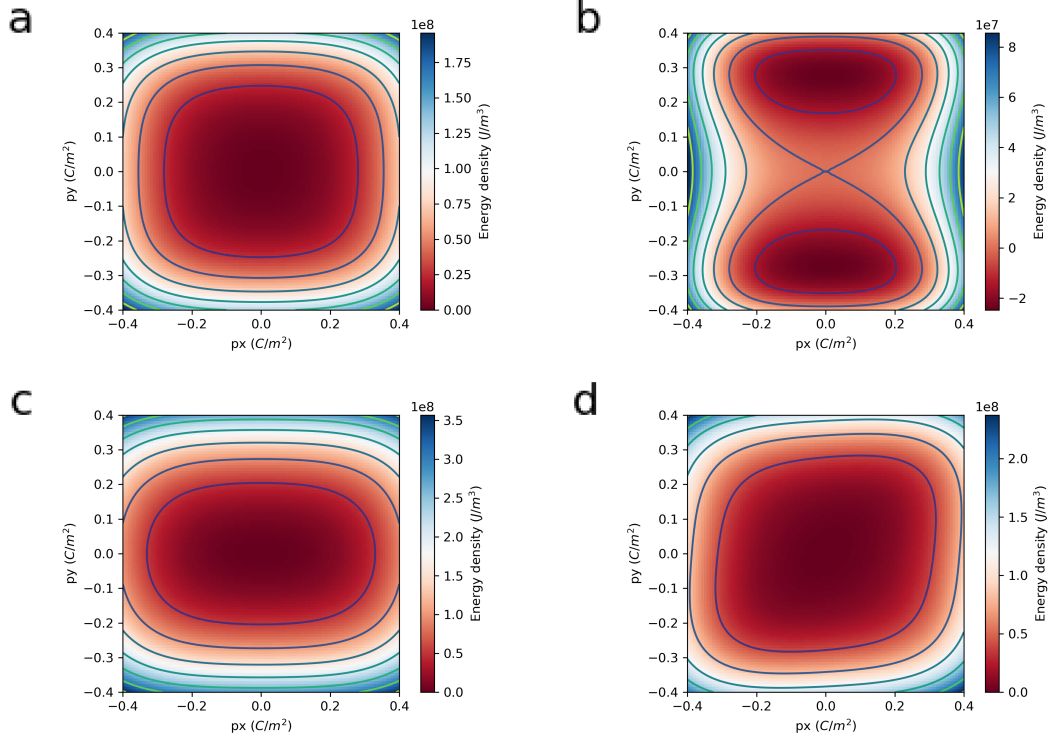


Figure 2.4. The total free energy landscape of SrTiO₃ under various conditions. (a) stress free. (b) 3% tensile strain along vertical y direction. (c) 3% compressive strain along vertical y direction. (d) 3% shear strain.

value they are representing.

Since $\epsilon_{11,3}$ dominates, and flexoelectric field along z have the largest value, we will naturally expect polarization to align along z direction. Surprisingly, the simulation result proves our intuition is wrong. The reason will become clear as we discuss the results in Figure 2.6 and 2.7.

The polarization distribution with and without flexoelectric contribution is shown in Figure 2.6. Result in Figure 2.6(a) is consistent with the analysis in Figure 2.3(a) and Figure 2.4(b,c) that if only consider electrostriction, it is possible to stabilize the polar state in the tensile region below the dislocation core with the polarization distribution along the tensile stress direction, and also remains in paraelectric phase in the compressive region above the dislocation core. The reason polarization in Figure 2.3(a) is pointing

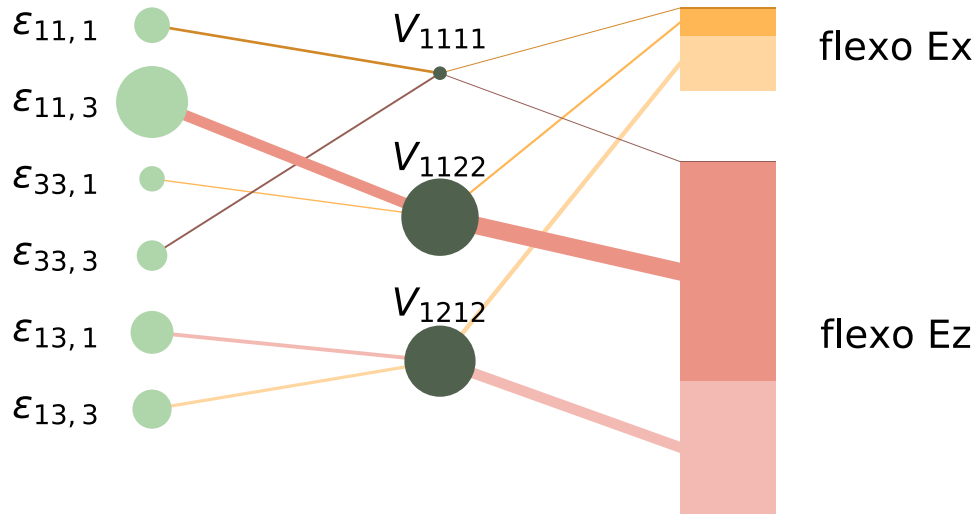


Figure 2.5. Illustration of each strain gradient component’s contribution to the final flexoelectric field for case 8. The light green column is strain gradient, the area of each circle is proportional to the maximum value of that strain gradient component. The dark green column is the flexoelectric coefficients for case 8, the area of which is proportional to the value of each flexoelectric coefficient. The two rectangles in the right column represent the x and z component of flexoelectric field vector. The area of each color shows the contribution from each strain gradient.

towards left is merely due to the initial random noise, as we have also observed the other degenerate state with polarization pointing towards right, if starting from a different noise distribution. Figure 2.6(b) shows that if flexoelectricity is taken into consideration (case 2 setup), the polarization becomes mirrored with respect to z axis. The flexoelectric field plotted in Figure 2.6(d) demonstrate more clearly the symmetric relationship of the flexoelectric driving force for polarization around the dislocation core. But the final polarization distribution is totally different from the flexoelectric field, indicating that though there is a significant change in polarization pattern when flexoelectricity is considered, electrostrictive effect still plays an important role in determining the final polar state of Figure 2.6(b). We can draw the same conclusion based on the fact that polarization distribution in Figure 2.6(b) has a much larger magnitude in the tensile region below the defect compare to the compressive region above the dislocation. The bar

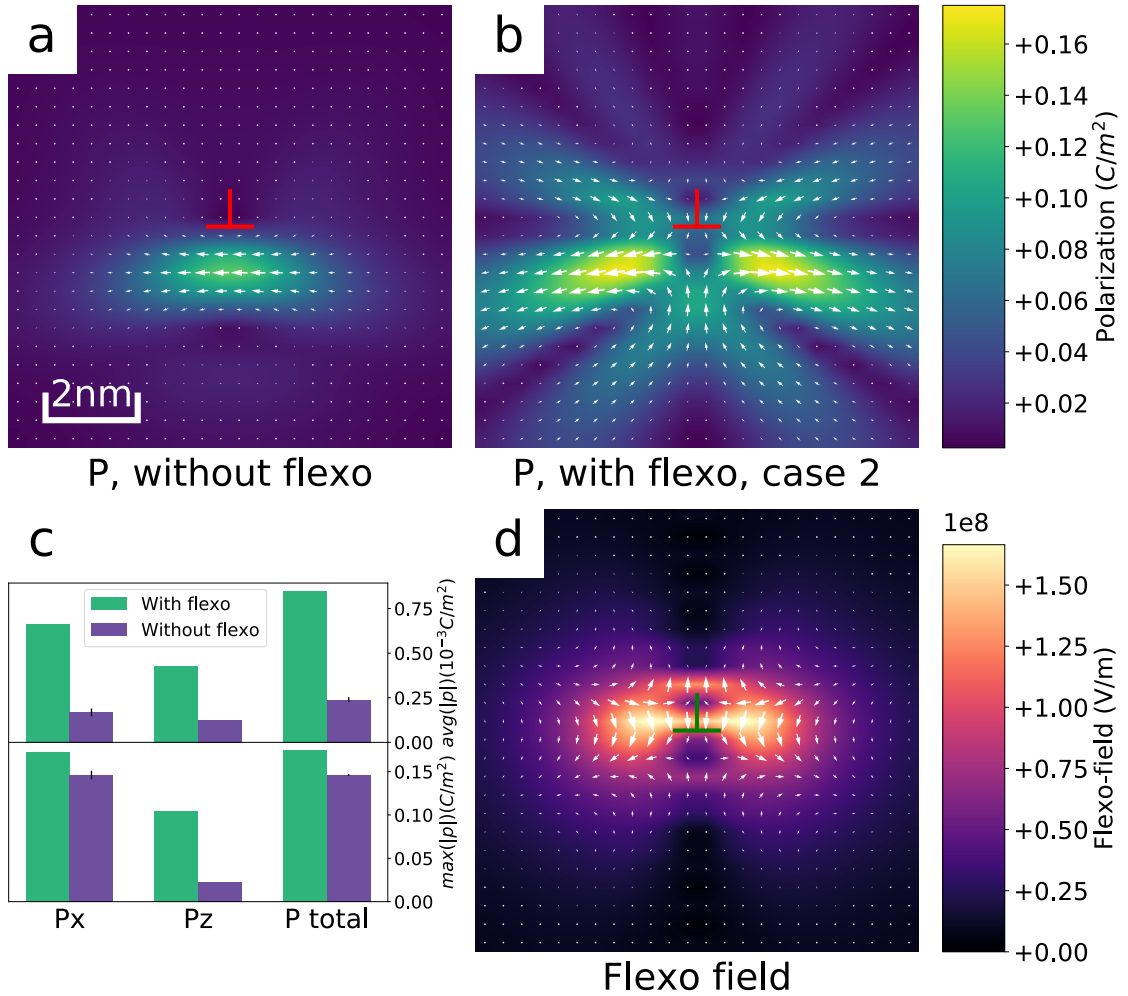


Figure 2.6. Comparison of polarization distribution with and without flexoelectric effect. (a) Polarization distribution without flexoelectricity. (b) Polarization distribution considering flexoelectricity. The quivers in (a),(b) indicate the polarization vector, and the background heat plot illustrates the magnitude of polarization. (c) Statistics of average and maximum Px, Pz and P total magnitude. (d) Flexoelectric field distribution, quivers indicate the flexoelectric field and background heat plot shows the magnitude of flexoelectric field.

plot in Figure 2.6(c) shows that flexoelectricity significantly boost the average polarization magnitude within the plotted region as in Figure 2.6(b) that flexoelectricity has a much larger influential region electrostriction. On the other hand, in terms of the maximum polarization, flexoelectricity has limited effect, since the maximum value always appear below the dislocation in the tensile region where the role of flexoelectricity is more of

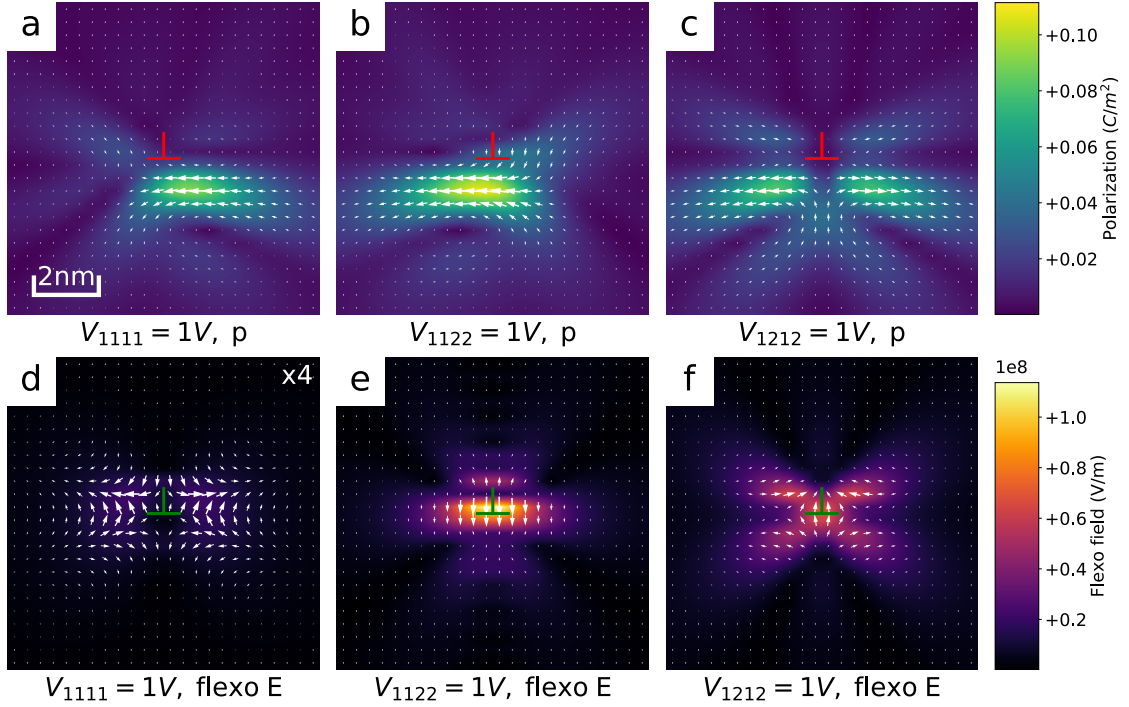


Figure 2.7. The polarization and flexoelectric field distribution using different flexoelectric coefficients for $b = a(100)$ edge dislocation. White quiver represent the plotted vector field, and background heat plot shows the magnitude of the vector. (a, b, c) Polarization distribution. (d, e, f) Flexoelectric field distribution. (a, d) non-zero longitudinal flexoelectric coefficient. (b, e) non-zero transverse flexoelectric coefficient. (c, f) non-zero shear flexoelectric coefficient.

reorienting the electrostrictively stabilized polarization. The larger increase in maximum P_z value is because in the pure electrostriction case, the tensile strain along x direction suppress the occurrence of polarization along z axis.

To further understand the influence of flexoelectricity, we took the advantage of simulation and performed a series of calculation varying the flexoelectric coefficients. Figure 2.7 shows the polarization and flexoelectric field distribution for three sets of flexoelectric coefficient. Comparing the polarization pattern in Figure 2.7 (a), (b), and (c) with the ones in Figure 2.6(a) and (b), we found that Figure 2.7(c) resembles Figure 2.6(b), both of which has the mirrored shape, while Figure 2.7(a) and (b) roughly maintain the uni-directional distribution as in the without flexoelectricity case in Figure 2.6(a). This

tells us that for the $b = a(100)$ edge dislocation case, the shear flexoelectric coefficient V_{1212} plays a more important role in shaping the polarization distribution than the longitudinal and transverse flexoelectric coefficient. As shown in the analysis of Figure 2.3 and 2.5, non-zero V_{1111} activates $\epsilon_{11,1}$ and $\epsilon_{33,3}$, but because both strain gradients and the coefficient are small, the magnitude of flexoelectric field in Figure 2.7(d) is small and thus the polarization pattern is only slightly changed compared to the without flexoelectricity case. Non-zero V_{1122} value leads to huge z component in the flexoelectric field due to the large $\epsilon_{11,3}$ value, but such large driving force did not transform into enhanced polarization along z axis. Similar to how strain engineering works in the epitaxial thin film, tensile strain here favors polarization along the same tensile direction, and suppress polarization in the perpendicular direction [80,108]. At the dislocation core, even though large flexoelectric field exists, it can only induce small vertical polarization because on one hand the vertical polarization is not favored, and on the other hand the polarization needs to try to align with the horizontal domain below the dislocation so that the electrical and gradient energy can be reduced. For V_{1212} , the combination of V_{1212} and $\epsilon_{13,3}$ result in the largest flexoelectric field along x (Figure 2.5), thus a symmetric polarization distribution with respect to the dislocation inclusion plane along the x direction is stabilized. And for a similar reason as in the V_{1122} case, the flexoelectric field along z direction at the dislocation core have no obvious effect on the final polarization pattern.

To understand how the magnitude of flexoelectric coefficient affect the final polarization pattern, we did some additional simulations using flexoelectric coefficients equal to 2V, as shown in Figure 2.8. The flexoelectric field scales linearly compared to the 1V cases in Figure 2.7, but the polarization patterns are clearly different for the longitudinal and transverse coefficient cases in Figure 2.8(a,b). For these larger coefficients, the flexoelectric

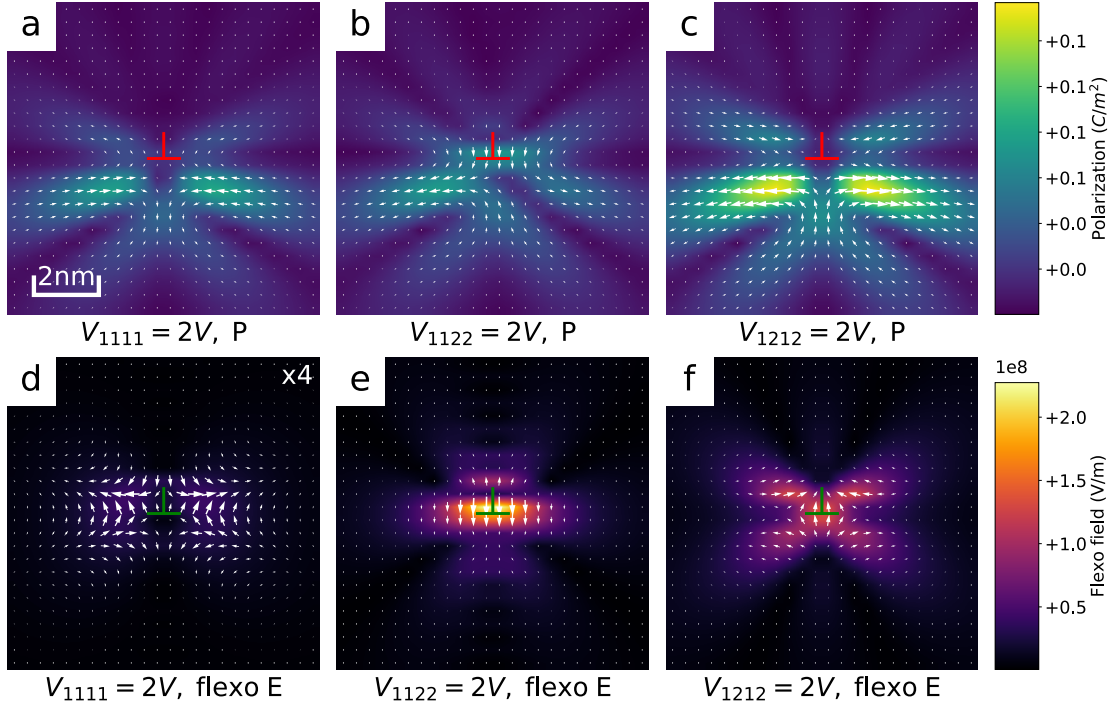


Figure 2.8. The polarization and flexoelectric field distribution using different flexoelectric coefficients for $b = a(100)$ edge dislocation. White quiver represent the plotted vector field, and background heat plot shows the magnitude of the vector. (a, b, c) Polarization distribution. (d, e, f) Flexoelectric field distribution. (a, d) 2V non-zero longitudinal coefficient. (b, e) 2V, non-zero transverse coefficient. (c, f) 2V, non-zero shear coefficient.

field is large enough to break out the local minima created by electrostriction and align the polarization with the field direction. The uncertainty of the flexoelectric coefficients is one of the problem for the study of flexoelectricity. There are discrepancies between experiment and theory, as well as between different experimental measurements. These uncertainties make the discussion of flexoelectricity more difficult as we have shown in Figure 2.7 and 2.8 that the polarization pattern may be completely different when the coefficients are only one time larger.

From Figure 2.3, 2.6, and 2.7, we learned several things, first, both polarization magnitude and pattern could be significantly affected by the flexoelectric effect. Second, though strain gradient and flexoelectric field may be large in some cases, it does not

necessarily mean polarization will follow the flexoelectric field direction.

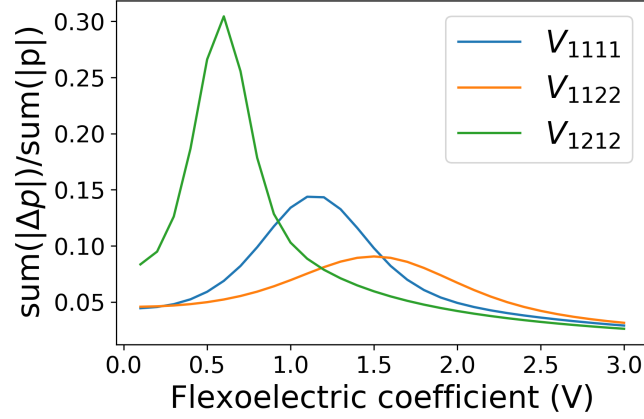


Figure 2.9. The changes in overall polarization with small increment in the flexoelectric coefficient. Simulations in this graph are performed with only one non-zero flexoelectric coefficient while keeping the other two zero, and the varying range of each coefficient is from 0 V to 3 V with an increment of 0.1 V. For the percentage value of y axis, we need to first subtract the polarization of smaller coefficient setup from the setup that the coefficient is larger by 0.1 V, and then sum the magnitude of such polarization difference over the whole simulation system to obtain a scalar value representing the total changes in polarization, then normalize it by the total polarization of the smaller flexoelectric coefficient case. Peak on this graph means a small change in flexoelectric coefficient will lead to large variation in the polarization distribution.

Since, on one hand, the magnitude of flexoelectric coefficients are extremely important in terms of determining the polarization distribution, and on the other hand, accurate coefficients are still undetermined in literature with only knowledge of the order's of magnitude. To get a better understanding of the effect for each flexoelectric coefficient, we must discuss how does the magnitude of the coefficient will affect the polarization. Figure 2.9 shows the relative changes in polarization for every 0.1 V changes in the flexoelectric coefficient. When the flexoelectric coefficients are small, the polarization distribution and magnitude are mainly determined by the electrostrictive effect. While when the flexoelectric coefficients are large enough to overtake electrostriction, the polarization pattern will change greatly as the domain reoriented towards the flexoelectric field directions, and peaks in Figure 2.9 occurs. When we further increase the flexoelectric

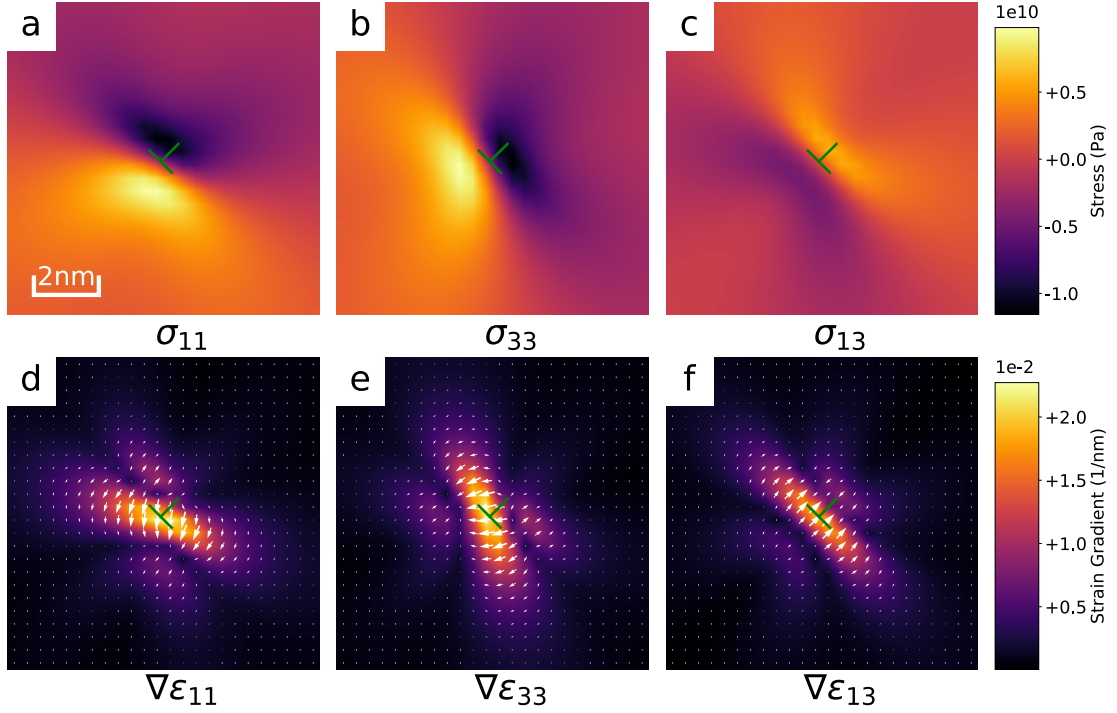


Figure 2.10. Stress and strain gradient distribution around (110) partial dislocation core. The dimension of the plotted region is 10nm by 10nm, and the dislocation is located at the center, labeled by the green T shape marker.

coefficient, the polarization distribution is mostly unchanged and only the magnitude becomes larger, thus the percentage of changing drops quickly. Figure 2.9 clearly indicates that the polarization distribution is most sensitive to the shear flexoelectric coefficient, as the peak comes at the lowest coefficient value but highest percentage magnitude.

Next, we performed the same set of calculation and analysis for $b = \frac{a}{2}(110)$ edge dislocation. To our surprise, the results are vastly different from the $b = a(100)$ edge dislocation case. For $b = \frac{a}{2}(110)$ edge dislocation, the stress/strain tensor is rotated by 45° compared to the $b = a(100)$ edge dislocation, which means smaller maximum stress/strain components and totally different strain/strain gradient distribution, both have a significant influence on the polarization distribution. From the comparison of Figure 2.10(a,b,c) and Figure 2.3(a,b,c), we can see that only σ_{11} has a similar distribution

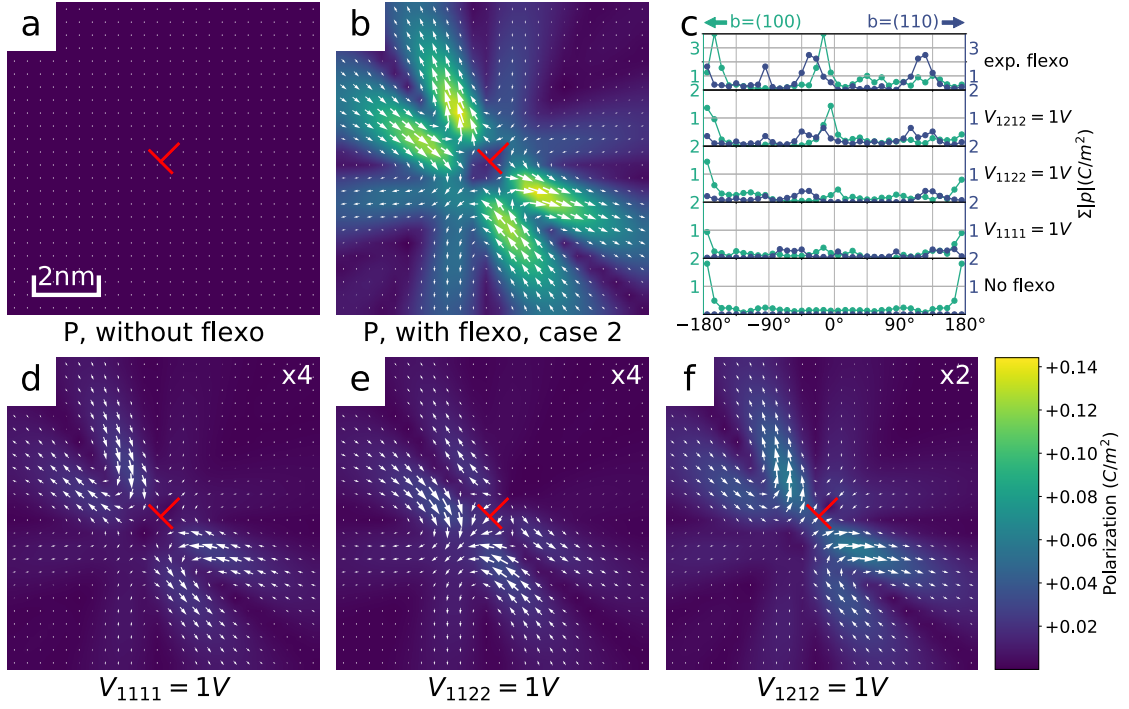


Figure 2.11. The polarization distribution using different flexoelectric coefficients for $b = \frac{a}{2}(110)$ edge dislocation. (a) no-flexo. (b) case 2 flexoelectric coefficient (d) non-zero longitudinal coefficient (e) non-zero transverse coefficient (f) non-zero shear coefficient. (c) Sum of total polarization for each orientation angle with respect to the (100) direction. Peak means more polarization is aligned along such direction.

in the two cases, while σ_{33} and σ_{13} are completely different. As a result, the strain gradient vector of $\nabla\epsilon_{33}$ and $\nabla\epsilon_{13}$ varies vastly in the $b = a(100)$ edge dislocation and $b = \frac{a}{2}(110)$ edge dislocation cases, which leads to different flexoelectric field distribution and the induced polarization pattern.

As shown in Figure 2.11(a), no ferroelectric phase can be stabilized by $b = \frac{a}{2}(110)$ edge dislocation without flexoelectricity. When flexoelectricity is considered, Figure 2.11(b), similar to the analysis for $b = a(100)$ edge dislocation, flexoelectric effect dominates the polarization pattern, which leads to a symmetric distribution of polarization with respect to the dislocation inclusion plane. There is no clear difference in polarization magnitude above and below the dislocation, which is different from $b = a(100)$ edge dislocation.

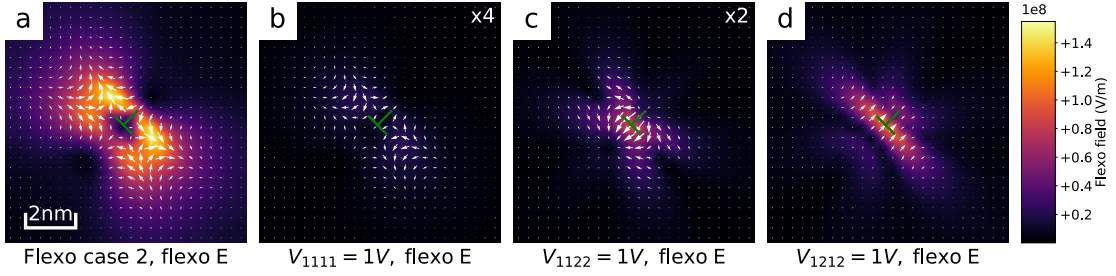


Figure 2.12. Flexoelectric field distribution of case 2, 3, 4, 5 for (110) partial edge dislocation.

To get a better idea of the difference between $b = a(100)$ edge dislocation and $b = \frac{a}{2}(110)$ edge dislocation, we plot the angular total polarization in Figure 2.11(c), in which x axis means the angle between polarization and the (100) direction and y axis means the summation of polarization, higher y value means more noticeable polarizations along such direction. The result shows that in $b = a(100)$ edge dislocation case, polarization is mainly along tetragonal direction as the angle is mostly 0° or 180° no matter what flexoelectric coefficients are used. While for the $b = \frac{a}{2}(110)$ edge dislocation case polarization is mainly along the orthorhombic direction, as peak angle appears at about 45° and 135° .

In Figure 2.11 (d), (e), and (f) we isolate the contribution from each of the flexoelectric coefficient and identify that still the shear flexoelectric coefficient V_{1212} has the largest effect on polarization among all three coefficients. Due to the non-existence of polarization under no-flexo condition, V_{1111} and V_{1122} are also capable of shaping polarization to follow the flexoelectric field direction, which is different from the $b = a(100)$ edge dislocation case.

We may also plot the flexoelectric field distribution for $b = \frac{a}{2}(110)$ edge dislocation, shown in Figure 2.12. As it is discussed in Figure 2.10, the flexoelectric field of the partial edge dislocation is not a simple rotation of the full edge dislocation case. Due to the smaller

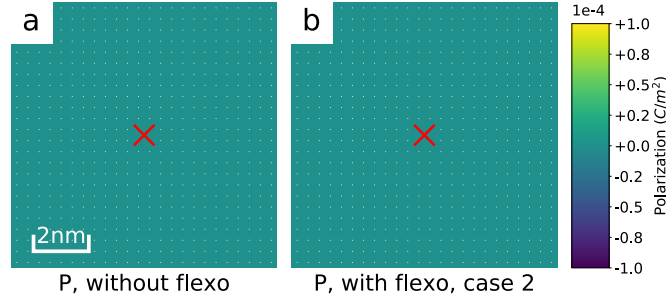


Figure 2.13. The results for $b = a(010)$ screw dislocation. (a), (b) polarization distribution without flexoelectricity and with case 2 flexoelectric coefficients, white dots are actually quivers for polarization and the background color is the magnitude of the polarization.

magnitude of stress magnitude for $b = \frac{a}{2}(110)$ edge dislocation, the electrostrictive effect is less significant compared to the $b = a(100)$ edge dislocation case, thus the polarization pattern in Figure 2.11 (b,d,e,f) roughly follows the direction flexoelectric field in Figure 2.12, with some minor differences in order to reduce some of the electrostatic and gradient energy. While in the $b = a(100)$ edge dislocation case, the polarization pattern is heavily influenced by the electrostrictive effect.

Figure 2.13 shows the results of polarization distribution around $b = a(010)$ screw dislocation core. From Figure 2.13 (a) and (b), we can draw the conclusion that neither electrostriction nor flexoelectricity will be able to stabilize any polar state in SrTiO_3 around the screw dislocation.

As shown Figure 2.14 (a, b), $b = a(010)$ screw dislocation will only introduce shear strain/stress into the system. From Figure 2.4(d), we know that the electrostrictive effect of shear strain can not stabilize the ferroelectric phases. For the flexoelectric effect of shear strain related to $b = a(010)$ screw dislocation, only the term $E_2^{flexo} = 2V_{1212}(\epsilon_{12,1} + \epsilon_{23,3})$ survives. But from Figure 2.14 (c) and (d), we know that $\epsilon_{12,1}$ and $\epsilon_{23,3}$ will cancel each other, thus lead to a net zero flexoelectric field and no induced polarization.

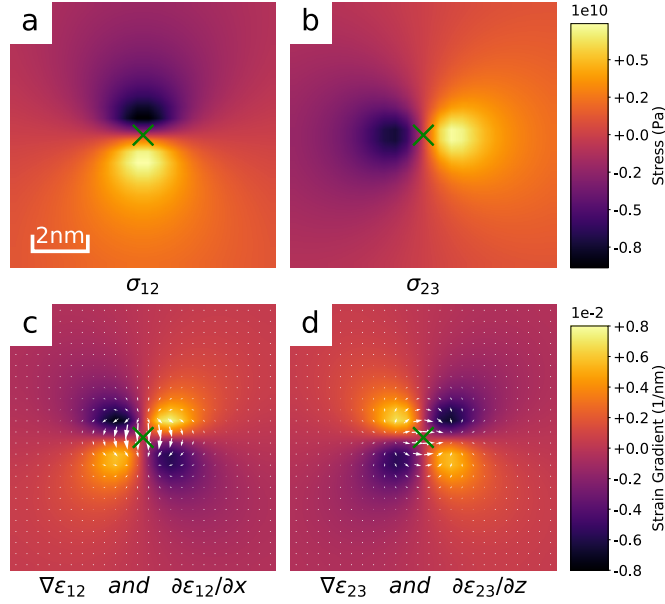


Figure 2.14. The results for $b = a(010)$ screw dislocation. (a) σ_{12} distribution. (b) σ_{23} distribution. (c), (d) White quiver shows $\nabla\epsilon_{12}$ and $\nabla\epsilon_{23}$ respectively, background color is distribution of $\frac{\partial\epsilon_{12}}{\partial x}$ and $\frac{\partial\epsilon_{23}}{\partial z}$, respectively.

2.4 Conclusion

In summary, we studied the role of flexoelectricity in stabilizing polarization at the dislocation core in SrTiO₃. Three types of dislocations, $b = a(100)$ edge dislocation, $b = \frac{a}{2}(110)$ edge dislocation, and $b = a(010)$ screw dislocation, are investigated. The effect of electrostriction and flexoelectricity is compared, and the contribution from the longitudinal, transverse, and shear flexoelectric coefficients are also discussed.

We found that in the case of $b = a(100)$ edge dislocation, both electrostriction and flexoelectricity are able to stabilize tetragonal polar phases. While in the $b = \frac{a}{2}(110)$ edge dislocation case, the electrostrictive effect is not large enough to induce any ferroelectric state and flexoelectricity is essential to the final orthorhombic + tetragonal polar state. For the $b = a(010)$ screw dislocations, neither the electrostrictive effect nor the flexoelectricity is able to stabilize any polar phases.

In both edge dislocation cases, flexoelectricity dominates and leads to a similar mirrored polarization distribution with respect to the dislocation inclusion plane. Maximum polarization value of about $0.18C/m^2$ and $0.14C/m^2$ can be obtained for the $b = a(100)$ edge dislocation and $b = \frac{a}{2}(110)$ edge dislocation cases respectively. A minor difference between the two cases is that for $b = a(100)$ edge dislocation, polarization below the dislocation is significantly larger than those above, while in the $b = \frac{a}{2}(110)$ edge dislocation case, the difference in polarization magnitude above and below the dislocation is negligible. Our study also identifies the shear component of flexoelectric tensor contributes the most to the flexoelectric induce polarization around the dislocation core.

Further simulations of how the charged dislocation core due to non-stoichiometry, may affect the local polarization distribution, and the interaction of multiple dislocations within SrTiO_3 are needed.

Chapter 3 |

Role of defect charge on polarization around dislocation in SrTiO₃

3.1 Introduction

Dislocations are the most common type of 1D defects in crystalline materials. It can significantly influence various properties of the material, such as plasticity [42], electric conductivity [43, 109, 110], magnetoresistivity [111], etc. Besides from the dislocation stresses due to lattice mismatch at the core, dislocation in ferroelectric or dielectric materials may also introduce defect charges into the system as the dislocation core has a distorted lattice which breaks local charge neutrality [101]. Many researches have explored the behavior of charges at dislocation core [43, 112], and demonstrate that dislocations can be considered as conducting filament which is particularly useful at the device level, such as in the nanoionics-based resistive switching memories [113]. Other researches

have shown that these dislocations in electroceramics will also lead to changes in the polarization distribution around the core region [1, 114], attributed to multiple causes including flexoelectric effect and local defect charges.

In perovskite electroceramics, such as SrTiO_3 , PbTiO_3 , dislocations may interact with the polarization through three effects, the strain or electrostrictive effect, the strain gradient or flexoelectric effect and the defect charges or the electric effect. Researchers have studied how the presence of dislocations in ferroelectric materials will influence properties, such as the transition temperature [115, 116], piezoelectric [117] and dielectric properties [118], but few have investigated how the three effects are affecting the local polarization distribution and identify the contribution for each one of them. In the past few decades, thanks to the advancement in electron microscopy and spectroscopy techniques, we are now able to map polarization and local chemistry directly from EELS and atomic resolution TEM image, but it is still very challenging to calculate the atomic displacement around distorted lattice region such as dislocation. Due to the limitations in both sample preparation and characterization techniques, researchers can only get those extreme quality HRTEM images for the $b = a(100)$ edge dislocation at the small angle grain boundary. Thus phase-field simulation is needed to explore and isolate the contribution to polarization from different sources and for various types of dislocations.

A discussion about the role of dislocation core's electric effect on polarization distribution and the comparison with the elastic contribution will be crucial for the comprehensive understanding and prediction of polarization patterns near the dislocation core in SrTiO_3 . In Chapter 2, we have already discussed the mechanical effect of dislocation core and studied the flexoelectric effect of the defect. In this chapter, we will further extend our model and explore the role of defect charges in creating local polarization.

We explore the influence of defect charges on local polarization in room temperature SrTiO₃ of three types of dislocation, $b = a(100)$ edge dislocation, $b = \frac{a}{2}(110)$ edge dislocation, and $b = a(010)$ screw dislocation. We find that for edge dislocations, defect charges have a shorter interaction range compares to the flexoelectric effect. The charge induced polarization has a highly anisotropic distribution that is directly related to the local stress state of the system. Defect charges, in the edge dislocation cases, lead to larger polarization value at the dislocation core comparing to the flexoelectric and electrostrictive effect, while the defect's elastic effects have a broader impact region and larger magnitude than the electric ones. Similar polarization distribution can be observed in experimental characterization of regions around $b = a(100)$ edge dislocations in SrTiO₃ [1]. In the screw dislocation case, the defect charges induce an almost isotropic polarization distribution around the dislocation core. At the same time, flexoelectricity does not influence the polarization due to the contrary contribution of the non-zero shear stress to the flexoelectric field. Overall, the pure electric effect of the defect charges leads to a nearly isotropic distribution of local polarization within 1 nm around the dislocation core for all three types of dislocation. The flexoelectric effect has a much larger impact on polarization in the two edge dislocation cases than the screw dislocation case. The electrostrictive effect only affects the polarization distribution in the two edge dislocation cases since the location of the total free energy minima is shifted by the local normal stress while remaining almost unchanged with the presence of shear stress. These results provide a comprehensive understanding of the elastic and electric effect of dislocations in ferroic materials on stabilizing the local polarization around the dislocation cores.

3.2 Materials and methods

We are using the phase-field method to simulate the polarization distribution around dislocation within bulk SrTiO₃, considering both the elastic and electric effect of the defect [80,81]. In our current model, we have two sets of order parameters, the polarization p , and the oxygen octahedral tilt, q , whose behaviors are described by the time-dependent Ginzburg Landau equation (TDGL 1.2). Equation 1.4 through 1.12 exhibit a self consistent thermodynamic based phase-field model whose coefficients are shown in table (1.2). Our model takes the defect charge due to non-stoichiometry, dislocation stress, and flexoelectric effect of non-uniform strain distribution into consideration by solving the TDGL (1.2), mechanical equilibrium (1.9) and poisson equation (1.10) in a coupled manner.

The mechanical effect of the dislocation is introduced through the eigenstrain terms in the equations [119,120]. In our simulation, instead of a δ function, the Burgers vector is treated as a normal distribution with variance equals to 0.5 around the dislocation loop.

The electrical effect of the dislocation is considered by manually adding some defect charges, q^D , at the dislocation core which ends up on the right-hand side of the Poisson equation (1.10) [2,78]. The amount of charges added is determined based on the reported range of charges due to oxygen deficiency in high resolution STEM and EELS characterization [102], and we picked an intermediate value of $0.96 \times 10^{-10} C/m$.

The flexoelectric effect is considered in the same fashion as in Chapter 2, with additional terms in both the free energy and eigenstrain [83,84]. Though flexoelectric effect is not the major concern of this chapter, it provides a reference for us to evaluate the effect of defect charges.

3D bulk simulation of $512 \times 1 \times 512$ grids (0.4 nm per grid) with periodic boundary

conditions and stress-free boundary condition is set up. One pair of dislocations with opposite Burgers vector are placed inside the simulation system, which form a dislocation inclusion plane so that the periodic boundary condition is fulfilled.

Among all of the possible dislocations in SrTiO_3 [3], we focus on three of them, $b = a(100)$ edge dislocation, $b = \frac{a}{2}(110)$ edge dislocation, $b = a(010)$ screw dislocation.

To clarify the role of defect charges in term of inducing local polarization, we conduct three groups of simulations, first, the main simulation that $0.96 \times 10^{-10} C/m$ of charges are added to the dislocation core and flexoelectricity is also considered, second, control group 1 in which defect charges are still considered but without flexoelectricity, and third, control group 2, 0 defect charges but with flexoelectric effect (using the following coefficients, $V_{1111} = 0.08(V)$, $V_{1122} = 2.6(V)$, $V_{1212} = 2.2(V)$ [85, 107]).

3.3 Results and discussion

Through the comparison of polarization for different dislocation charge state in Figure 3.1, we find that the polarization pattern for cases with and without defect charges are rather qualitatively similar to each other in the two edge dislocation setups. In contrast, the polarization distribution is vastly different in the screw dislocation case. This is due to the fact that flexoelectricity, which plays a dominant role in shaping the polarization for edge dislocations, has a negligible effect on screw dislocation, as it is shown in Chapter 2.

A more careful examination of the results in Figure 3.1 shows that in the edge dislocation zero defect charge cases, there is a "hole" at the dislocation core where the polarization magnitude is smaller than the surroundings, while non-zero defect charges lead to an increased polarization magnitude at the core, thus filling the "hole". This indicates that electrical effect due to defect charge and the mechanical effect, including

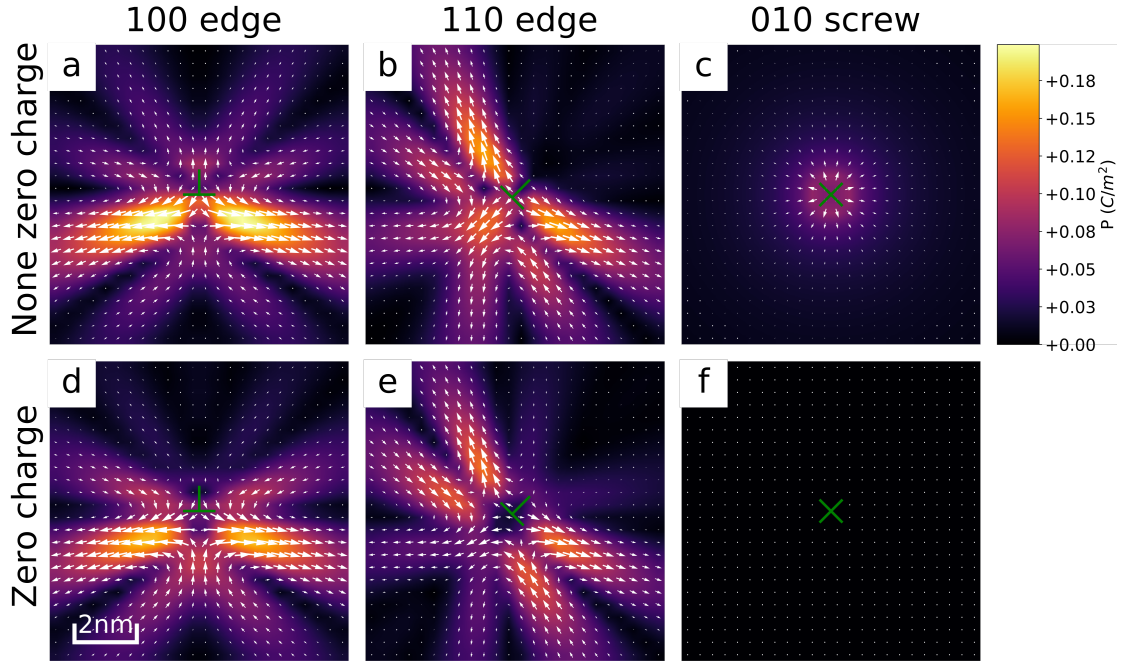


Figure 3.1. Comparison of polarization distribution with and without defect charges. White quivers represent polarization vectors, background heat map shows the polarization magnitude, and green crosses mark the location of dislocations. In all cases flexoelectricity are considered. (a), (b), (c) with $0.96 \times 10^{-10} C/m$ defect charge at dislocation core. (d), (e), (f) 0 defect charge. (a), (d) $b = a(100)$ edge dislocation. (b), (e) $b = \frac{a}{2}(110)$ edge dislocation. (c), (f) $b = a(010)$ screw dislocation.

electrostriction and flexoelectricit, have a different interaction length with polarization.

To quantitatively study how the interaction length is different, we plot the radial distribution of maximum polarization around the dislocation core for the two control groups of simulation that considers flexoelectricity and defect charge separately. In the upper panel of Figure 3.2 in which only flexoelectricity are considered, the peak appears around 5 to 6 nm, with a value of $0.175 C/m^2$ for the $b = a(100)$ edge case, $0.144 C/m^2$ for the $b = \frac{a}{2}(110)$ edge case. While in the lower panel of Figure 3.2 which is when $0.96 \times 10^{-10} C/m$ of defect charge is considered, the peak appears at around 1 to 2 nm, with peak value of $0.104 C/m^2$ and $0.114 C/m^2$ for the edge dislocation case and $0.079 C/m^2$ for the screw dislocation case. This result demonstrates that the interaction range of electric coupling between dislocation and the surrounding polarization is about 4

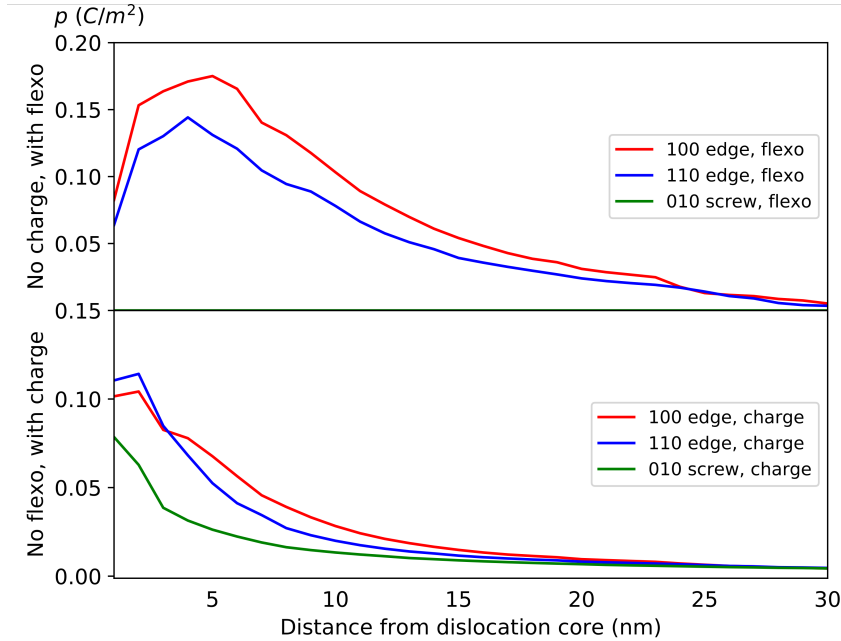


Figure 3.2. Radial distribution of maximum polarization around the dislocation core. Lower panel is for control group 1, when flexoelectricity is ignored, and defect charge is considered. The upper panel is for control group 2, in which flexoelectricity is taken into account but without defect charge.

nm shorter compared to the interaction range for strain gradient and local polarization coupling.

Another phenomenon we notice in Figure 3.1 is that in the two edge dislocation cases, the magnitude is slightly larger in certain regions when the charge is considered. This tells us that the charges at the edge dislocation core will lead to a none uniform polarization distribution. Result in Figure 3.3 shows how the polarization varies in all three dislocation cases for our control group 1, in which flexoelectricity is turned off, and only defect charge is considered. Such distribution is related to the tensile stress within the system, as you can see in the Figure 2.3, Figure 2.10, and Figure 2.14 the tensile stress patterns match with the charged induced polarization region in Figure 3.3.

The reasoning behind this is straight forward. For simulations in Figure 3.3(a,b,c), there is only the quadratic electrostrictive coupling between polarization and stress, which

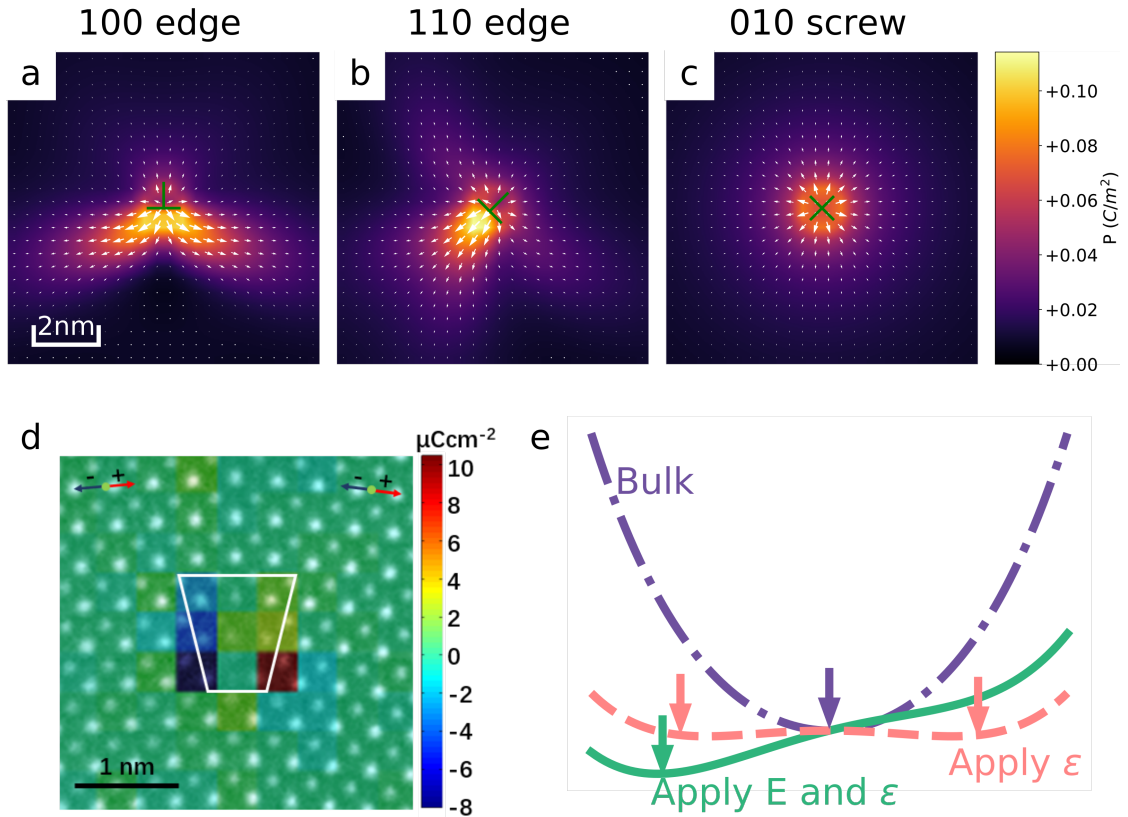


Figure 3.3. Polarization distribution for control group 1 (a) $b = a(100)$ edge, (b) $b = \frac{a}{2}(110)$ edge, (c) $b = a(010)$ screw. (d) Experimental polarization mapping around a $b = a(100)$ edge dislocation in 10° SrTiO₃ bicrystal, the direction of polarization is indicated by the illustration arrows on top, and the magnitude is shown by the color. The white trapezoid represents the dislocation core. (e) Illustration of the free energy profile with respect to the polarization value under different conditions. Red dash line shows energy profile of strong electrostrictive coupling. Solid green line shows the energy profile when both external electric field and applied strain exist. And the dot purple line shows the Landau part of the total free energy, which can be considered as a reference for the other two curves.

will modify the depth of free energy well, so the stress distribution will lead to non-uniform changes of the free energy profile at different positions relative to the dislocation core. The quadratic relationship will not break the symmetry of the paraelectric phase. However, when it is coupled with the external field, in our case, the centrifugal electric field due to the charges at dislocation core, the result is a local transition from paraelectric phase to ferroelectric phase in a deterministic manner. This can only happen at locations where the free energy barrier is lowered enough by the electrostrictive coupling. Figure 3.3(e)

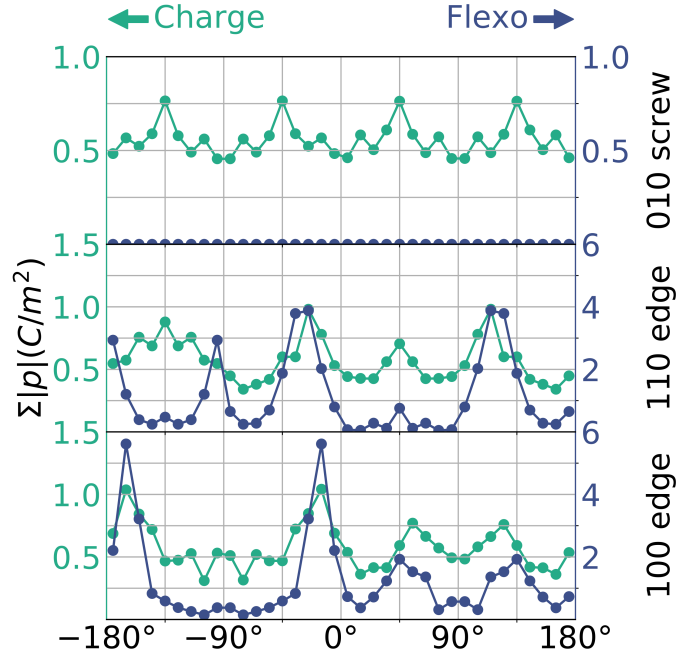


Figure 3.4. Angular distribution for the summation of total polarization for every 10° of orientational angle. X axis is the angle between polarization and (100) direction. Left green axis is for the results of control group 1, in which there is non zero defect charge but no flexoelectricity, and right blue axis is for the results of control group 2, in which flexoelectricity is considered but without defect charge. The three panels correspond to the three types of dislocation, as shown on the right of the figure.

illustrate how the electric field and electrostrictive coupling contributes to modifying the free energy profile. Figure 3.3(d) shows the experimental mapping of polarization. This HAADF-STEM image is overlaid by the unit scale mapping of polarization value perpendicular to the grain boundary from the extracted atomic positions. Clearly, the plotted x component of polarization around the dislocation is mirrored with respect to the dislocation inclusion plane, and the magnitude is significantly larger in the tensile region below the defect compared to the compressive region above the defect.

surprisingly, our simulation result in Figure 3.3(a) matches very well with experiment. The experimental image shows three features that are all qualitatively captured our simulation results, first, polarization is mirrored over (100) plane around the $b = a(100)$

edge dislocation core which sits on the small angle grain boundary in a bi-crystal setup. Second, the maximum polarization appears below the dislocation in the tensile region of about $0.1\text{C}/\text{m}^2$. Third, the maximum induced polarization appears in close vicinity to the dislocation core, about or less than 1nm. While in contrast, the simulation result that considered flexoelectricity in Figure 3.1(a) is quite different from the experiment, as the influential region is much larger, and the direction of polarization above the dislocation is the opposite compared to experiment. This indicates that in the experiment, at least around the dislocation core, the flexoelectric effect is not as strong as we expected. A possible explanation is that the flexoelectric coefficients may not be as accurate as we wanted, since the three coefficients are from a different batch of measurements [85, 107]. From Figure 2.8, we know that V_{1111} and V_{1212} have an opposite effect on induced polarization. Thus it is possible that a variation in the flexoelectric coefficient may lead to a different polarization distribution which resembles the experiment observation. In order to study whether flexoelectricity or electric effect dominates around the dislocation core, more experiments results for the $b = \frac{a}{2}(110)$ edge and $b = a(010)$ screw are needed, but that's beyond the scope of this simulation work.

The angular total polarization in Figure 3.4 shows the quantitative orientation distribution of polarization, in which peak means more noticeable polarization is aligned along such direction. For the charged $b = a(010)$ screw dislocation results in the upper panel, the profile tells us that the seemingly isotropic pattern of Figure 3.3(c) is actually larger along the diagonal direction and has a D_4 symmetry in 2D point group. For $b = a(100)$ edge, the peaks appear around 0° and 180° , which are the tensile direction for this dislocation. In the $b = \frac{a}{2}(110)$ edge cases, the peaks show up at different angles from the two control groups, as the polarization is reoriented towards the dislocation core

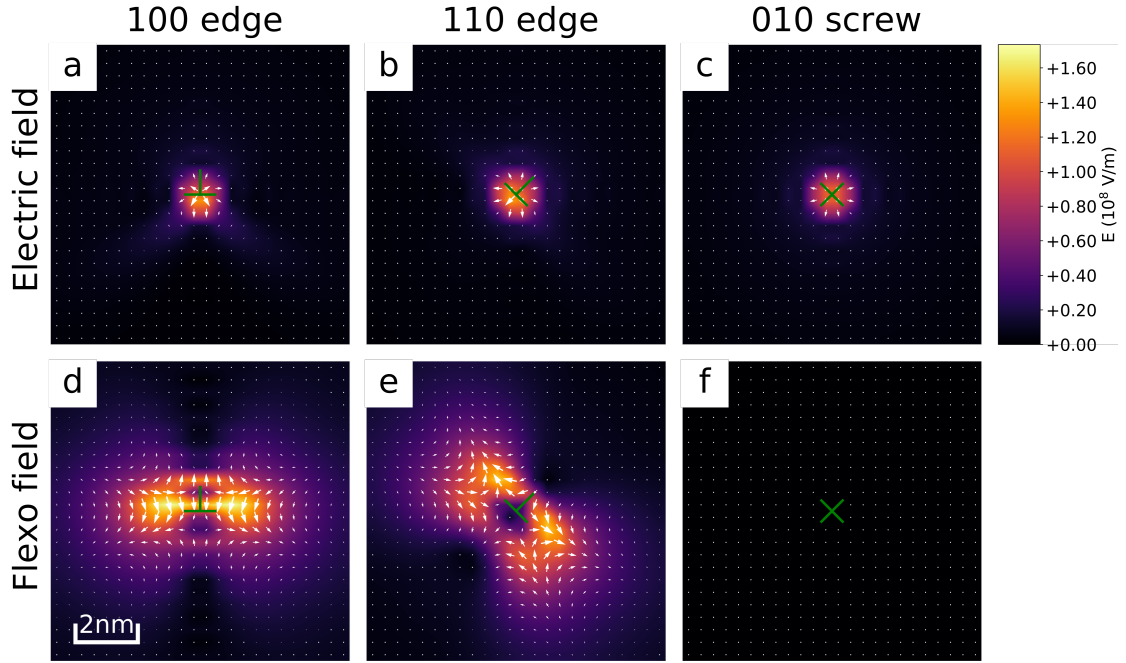


Figure 3.5. Electric field and flexoelectric field distribution for the three types of dislocations. (a), (b) and (c) electric field of control group 1, with defect charge, no flexoelectricity. (d), (e) and (f) the flexoelectric field of control group 2, with flexoelectricity, but 0 defect charge.

rather than the tensile direction when only defect charge is considered. For both the two edge dislocation cases, we can observe that the magnitude of total polarization for the peak orientation is 4 times larger when the flexoelectric effect is considered compared to cases only consider the defect charge. This again shows the dominance of flexoelectricity over defect charge around edge dislocations in SrTiO_3 , confirming the results in Figure 3.1 (d).

The minimum value, on the other hand is rather similar for control groups 1 and 2, which leads to a smaller peak to trough ratio for defect charges compared to flexoelectricity. The results show that the combination of defect charge and electrostriction is more permissive than flexoelectricity plus electrostriction in terms of the induced polarization orientation. This can be explained by Figure (3.5) using the following two arguments, first, defect charge is a point charge (in this 2D view, and line charge in 3D) which creates

a centrifugal electric field, while flexoelectricity can be considered as a highly anisotropic effective electric field, second, the effective electric field of flexoelectric effect is almost 2 times larger than the magnitude of defect charges' electric field with a vastly larger influential region.

There is a limitation of our current model. That is, we ignore the existence of free carriers in the system. Though SrTiO₃ is a very good insulator, some experiments have shown that threaded dislocation in SrTiO₃ may be considered as conduction filaments, indicating that higher local free carrier density is available around the dislocation core, which means charge screening of the dislocation nonstoichiometry will appear. This will definitely affect the defect charge induced electric field and thus the local polarization distribution, but due to lack of information for the band structure of dislocation core, we cannot have a good estimation of the screening charges and do an ad hoc simulation. This is something we need to address in the future by developing a new self-consistent model that includes both the ferroelectric polarization and the migration and recombination of free carriers in the system, which is beyond the scope of this dissertation and probably deserves a dedicated thesis work.

3.4 Conclusion

In summary, we studied the defect charges effects on local polarization around three types of dislocations in SrTiO₃ single crystal, $b = a(100)$ edge, $b = \frac{a}{2}(110)$ edge, and $b = a(010)$ screw. We found that the charge induced polarization exists mainly within 5 nm region around the dislocation core, and peaks in less than 2 nm distance from the core. The distribution of defect charge induced polarization is highly anisotropic in the two edge dislocation cases, whose pattern is related to the tensile stress region

around the edge dislocation. In the screw dislocation case, the defect charge leads to a D_4 symmetric pattern, with slightly larger polarization magnitude along the diagonal directions. In our simulation, the charge effect dominates in the screw dislocation case, while flexoelectricity plays a more important role in the two edge dislocation scenarios. But a comparison between our simulation result and the experimental characterization for $b = a(100)$ edge indicated that the polarization distribution is mainly due to defect charge, and flexoelectricity has a very limited effect around dislocation core. To obtain a more accurate estimation of the flexoelectric effect and the coefficients, more experimental measurements, especially the polarization mapping for the $b = \frac{a}{2}(110)$ edge and $b = a(010)$ screw, are needed.

These results provide a comprehensive understanding of the elastic and electric effect of dislocations in ferroic materials on stabilizing the local polarization around the dislocation cores.

Chapter 4 |

Control the 71° domain patterns in BiFeO₃ through defect engineering

4.1 Introduction

Ferroelectrics are materials with spontaneous polarization that can be switched by externally applied electric field. One of the most interesting properties of ferroelectric materials are the rich amount of polarization domain patterns and the evolution of them. After decades of exploration, various applications have been proposed utilizing the domain patterns in ferroelectrics that can be categorized into two categories, one using properties of the domain walls and the other using properties of the domain itself. The physics properties of domain walls are usually completely different from the bulk domain part, for example, the ferroelectric domain walls are in many cases electrically more conductive than the bulk part. Researchers have observed various levels of conductivity at the domain

wall in BiFeO₃ [121], anisotropic conductance depending on the domain wall orientation in YMnO₃ [122] and anisotropic conductance in terms of the measuring orientation in BiFeO₃ [123]. Several concepts for nanoelectronic devices have been proposed based on these domain wall properties, such as nonvolatile resistance switching ferroelectric memory that allows a non-destructive read-out through the highly conducting domain walls in BiFeO₃ [124, 125], and conformational domain wall switch that can transform between three states which enable new logic possibilities in nanoelectronic devices [126]. Another example of the domain wall property that is vastly different from the bulk is the thermoelectric conductivity [127], ferroelectric domain wall phonon polarizer has been predicted in PbTiO₃ that suppress transverse phonons and permit longitudinal phonons due to the huge structural inhomogeneity at the domain wall [128], significant phonon scattering has also been observed in BiFeO₃ and KH₂PO₄ that decreases the effective thermoconductivity of the material [129, 130].

On the other hand, bulk domains also have a variety of interesting properties, for example in BiFeO₃, the unassisted photocatalytic water splitting due to the local electric field induced by polarization bound charges at the interface/surface which facilitate the carrier separation and diffusion [64]. Another example is the spatially selective reduction of Ag on BiFeO₃ surface as the reaction only happens in regions with upward domains due to the difference in band bending of positive and negative domain at surface [131]. A more popular example is the switchable ferroelectric diode of single domain BiFeO₃ and the photovoltaic effect within visible light wavelength range [132].

A common demerit of ferroelectric domain wall devices is the scalability issue due to the physical limitation of minimum domain size. And one benefit of defect engineering is that the domain location is strongly affected by the defect configuration, which helps

to break the domain size limits imposed by domain wall energy in a predictable manner. Though it is still not able to compete with the Si based solution used in CPUs and memories that can scale down to several nanometers, it does broaden our possible choices of building nano devices on the scale of 10 to 100 nm.

In order to utilize the functionalities of the domain walls and domains stated above, researchers need to have full control over the domain patterns. The capability to control the polarization domain in ferroelectrics and thus obtaining the desired properties, thus, has always been one of the primary goals for ferroelectric researchers. Possible routes to achieve such a goal include domain engineering in bulk single-crystal and ceramic, strain engineering in epitaxial thin-film, defect engineering, etc. Chu et al. tried to control the as-grown state of BiFeO_3 , whether it is 71° or 109° domain strips, by varying the bottom electrode type and thickness [133]. Hong et al. constrained the dimension of the ferroelectric materials using a superlattices setup and stabilize the complex topological domain structures, such as vortices [134] and skyrmions [135]. Recently, a novel defect engineering method for BiFeO_3 has demonstrated its potential in controlling 71° domain strips through the introduction of charged defect during epitaxial thin film growth [2]. Experiments in [2] were done by our collaborator, Dr. Linzi Li, from Professor Xiaoqing Pan's group in University of California at Irvine, which inspired us to further investigate the defect engineering in BiFeO_3 thin film that is discussed in this chapter.

In this chapter, we will explore and explain in a more systematic manner how the defect configurations will result in different domain patterns in BiFeO_3 thin film. We study how defect engineering in BiFeO_3 , more specifically, controlling parameters of the non-stoichiometric charged defect such as defect width, interval, and location, may determine the thermodynamically most stable domain structure inside the thin film. From

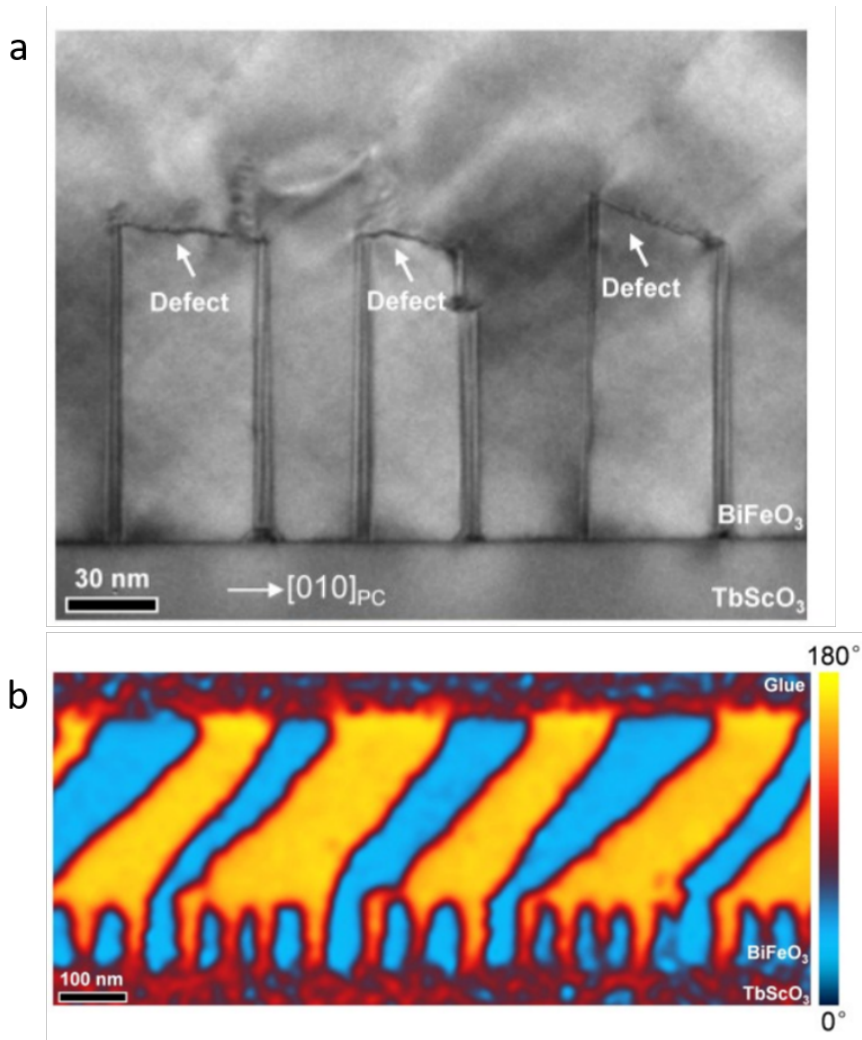


Figure 4.1. Experimental results. (a) Cross-sectional bright-field TEM image and corresponding schematic of polarization structures showing ordered 71° and 109° domains separated by an array of defects in a 400 nm BiFeO₃ film. (b) PFM phase image showing the same periodically ordered domain patterns in the same BiFeO₃ film. [2]

the transmission electron microscopy and piezoelectric force microscopy results in Figure 4.1 (a) and (b), we observe the defects have an average dimension of tens of nm, locating at the same height inside the BiFeO₃ thin film. They always have a planar shape, either parallel to a small angle to the film surface, and the 71° domain strip only appears above some of the defects, while remaining in a single domain state above others. We perform high-throughput simulations varying the defect width, defect interval, and defect height

Domain setup	Defect Width	Defect Interval	Defect Position	
Case 0 (Base)	40 nm	40 nm	25 nm	= 500 jobs
Case 1	60 nm	60 nm	50 nm	
Case 2	80 nm	80 nm	75 nm	
Case 3	100 nm	100 nm	100 nm	
Case 4	120 nm	120 nm		

Figure 4.2. The parameter space that is explored with our high-throughput simulations.

within a 200 nm BiFeO₃ thin film. The stability of the 71° domain strips above the charged defects is explained through the competition between elastic and domain wall energy. The trends for every energy term with respect to the defect configurations are explained and analyzed. From which, we obtained an empirical formula that relates the defect width, defect position, and thin film thickness with the final domain pattern, which can be used as a predictive tool for the occurrence of the 71° domain strips above the defects in BiFeO₃ thin film. Our conclusion is that there exists a minimal defect width that can stabilize 71° domain above the charged defect in favor of a single domain state. The threshold value is determined by the thin film thickness and the defect location.

4.2 Materials and method

The simulation method that we use to relax the domain structures that we prepared is called phase-field method. It is a mesoscale phenomenological model whose major feature or advantage over other model is the introduction of a diffused interface between phases instead of a sharp one, thus eliminating the needs to track the interface evolution explicitly.

For the phase-field model of ferroelectrics, we are using polarization as our order

parameter to describe the simulation system and differentiate between various polarization domains. We solve the TDGL equation (4.1) using a semi-implicit fourier spectral method along with the poisson equation (4.3) with short circuit boundary condition for thin film surface and film/substrate interface, and the mechanical equilibrium equation (4.4) with traction free boundary conditions on film surface and zero displacement somewhere inside the substrate. The parameters of BiFeO₃ that we are using can be found in Chapter 1.

$$\frac{\partial P_i}{\partial t} = \frac{\delta F}{\delta P_i}, (i = 1, 2, 3) \quad (4.1)$$

$$F = \int_V (f_{landau} + f_{elec} + f_{elas} + f_{grad}) dV \quad (4.2)$$

$$\nabla \cdot (\kappa \cdot \nabla \phi) = \frac{-P_{i,i} + q^D}{\epsilon_0} \phi|_{sur} = 0, \phi|_{int} = 0 \quad (4.3)$$

$$C_{ijkl}(u_{k,lj} - \epsilon_{kl,j}^0) = 0, \sigma_{i3}|_{sur} = 0, u_i|_{bot} = 0 \quad (4.4)$$

Charged defects are introduced into the simulation system by adding a fixed source of charges for the defect, q^D , in the Poisson equation (4.3). The amount of defect charges that we used is $-1.1 \times 10^9 C/m^3$, which is determined based on estimation of published experimental HRTEM observations [2].

Our simulations have periodic boundary condition for the in-plane directions, and thin film boundary conditions (stated above) for the out-of-plane direction, with a thin film thickness of 200 nm. As it is shown in Figure 4.2, we performed a total of 500 simulations jobs, considering 5 different defect width, 40nm, 60nm, 80nm, 100nm, 120nm, 5 different defect intervals, 40nm, 60nm, 80nm, 100nm, 120nm, 4 different defect positions, 25nm, 50nm, 75nm, 100nm, for all 5 domain configurations in Figure 4.3. The meaning of width, interval and height are illustrated in Figure 4.3a. The arrows and text in Figure 4.3c

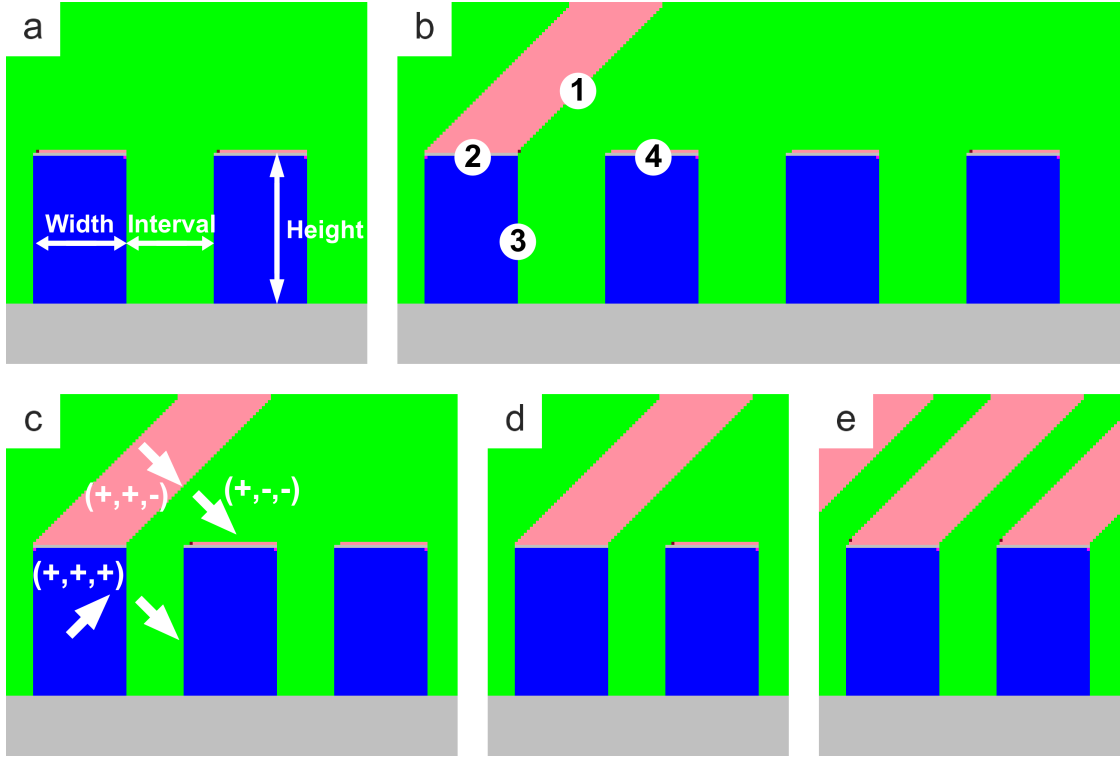


Figure 4.3. The 5 preset domain structures that we have studied. (a) Case 0, (b) Case 4, (c) Case 3, (d) Case 2, (e) Case 1. Case number means one 71 domain strip every n^{th} of defects. The meaning of width, interval and height are marked in (a). Each color represent one type of polarization domain, gray represents substrate, and the polarization directions are labeled in (c). All four types of domain walls are labeled in (b).

illustrates the polarization vector direction, green domain is R2- domain $(+,-,-)$, blue domain is R1+ domain $(+,+,+)$, pink domain is R3- domain $(+,+,-)$, and gray part is substrate. There are a total of 4 types of domain walls in our setup, marked in Figure 4.3b, type 1 is 71° neutral domain wall, type 2 is a 71° charged domain wall stabilized by the charged defect along the wall, type 3 is a 109° neutral domain wall, type 4 is a 109° charged domain wall also stabilized by the defect.

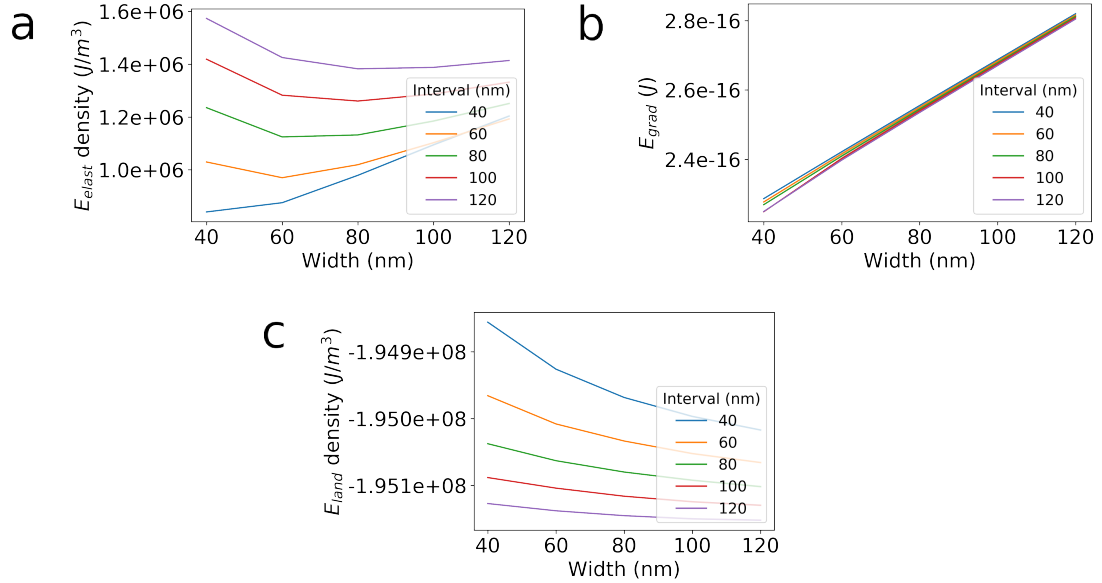


Figure 4.4. Free energy components for Case 2 (Figure 4.3d) varying defect width and interval. The defect height is fixed at 100 nm. (a) Elastic energy density. (b) Gradient energy. (c) Landau energy density.

4.3 Results and discussion

It is impossible and unnecessary to show all of the results for every case since the difference between the two setups is mainly the periodicity of the 71° domain above the charged defect. We will use the analysis of Case 2 as an example, and then summarize the relationship between elastic energy reduction, gradient energy, and the defects configurations based on all 500 simulations.

In Figure 4.4, we examine the different energy components for Case 2 with a defect height of 100 nm. Since the elastic and landau energy depend on the bulk volume of the domains, which means they will scale with size, energy density instead of energy is plotted for the comparison. While for the gradient energy, it only depends on the domain wall area and domain wall type, irrelevant to the size of the system, thus the energy rather than energy density is visualized. For a zero mismatch thin film setup, 71° or 109°

domain strips are always elastically more favorable compared to a single domain state. The reduction in elastic energy is related to the number of domain strips added to the system. The elastic energy reduction reaches a maximum value when the alternating domain strips are equal in width. This means for case 2, elastic energy will rise with the increase of defect interval, while keeping the defect width constant. Thus the highest elastic energy density is the case when the smallest amount of 71° domain exists. The reason curve in Figure 4.4a is not monotonous is because the elastic energy is related to not only the 71° domain above the defect, but also the 109° domains below the defect. Elastic energy favors thinner domain strips, since thinner strips will match the substrate lattice better, leading to a lower energy.

As shown in Figure 4.3b, there are 4 types of domain wall in the system, type 1 (71° charge neutral) and type 3 (109° charge neutral) walls depend on the defect height, while type 2 (71° charged) and type 4 (109° charged) walls depend on the defect width. Thus, at a given defect height, as shown in Figure 4.3b, the gradient energy increases as the defect becomes longer, while it remains unchanged when the defect interval varies. It is important to point out that gradient energy alone only accounts for half of the domain wall energy. The other half comes from the bulk part, the landau energy. This helps to explain the result of landau energy density in Figure 4.3c. As the defect interval increases under the same defect width and height, the bulk part of domain wall energy is constant. But, since the total system size increases, the landau energy density decreases. The reason that at a given defect interval and defect height, the landau energy density declines as the defect width expands is that type 1 and type 3 domain wall contribute a major part to the total domain wall energy which is a constant for all simulations in Figure 4.3c, so even though type 2 and type 4 domain wall has a linear relationship with the defect width,

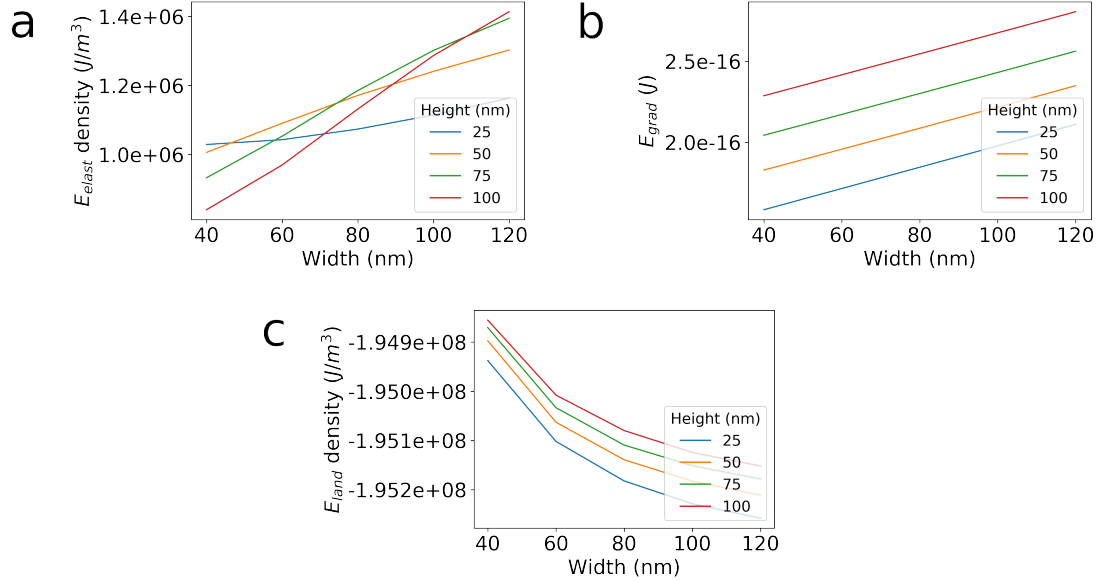


Figure 4.5. Free energy components for Case 2 varying defect height and width. The defect interval is chosen to be the same as defect width. (a) Elastic energy density. (b) Gradient energy. (c) Landau energy density.

the overall domain wall energy normalized by the system volume is still decreasing. We observe that the relative change of landau energy density is much smaller than the elastic and electric ones because except the domain wall parts, the majority of the simulation system are domains at their equilibrium.

Figure 4.5 shows results when defect heights and defect width are varying while keeping the defect interval the same as the defect width. The lowest elastic energy density in Figure 4.5a appears when defect width is the smallest and height is the largest. There are two reasons for this. First, the higher defect position is, the larger 109° domains are below the charged defect, which helps to release the elastic energy of single domain state. Second, elastic energy favors finer domains as thinner domain strips have smaller misfit with the substrate. For the gradient energy, since both defect height and width are changing, all 4 types of domain wall will vary under different conditions. The lowest energy case is when both defect height and width are the smallest, because in such setup, the area of type 3

domain wall is minimized (type 3 domain walls have larger total gradient energy than type 1 domain wall) and the area of type 2 and type 4 domain walls are also minimized. Analysis for the landau energy density is similar to Figure 4.5c, that it contributes to part of the domain wall energy and the relative changes are small due to that most of the domains are at equilibrium. The highest landau energy density is the case when defect width is the smallest while the defect height is the largest, because this condition gives us the finest domain strips and largest amount of 109° domain walls.

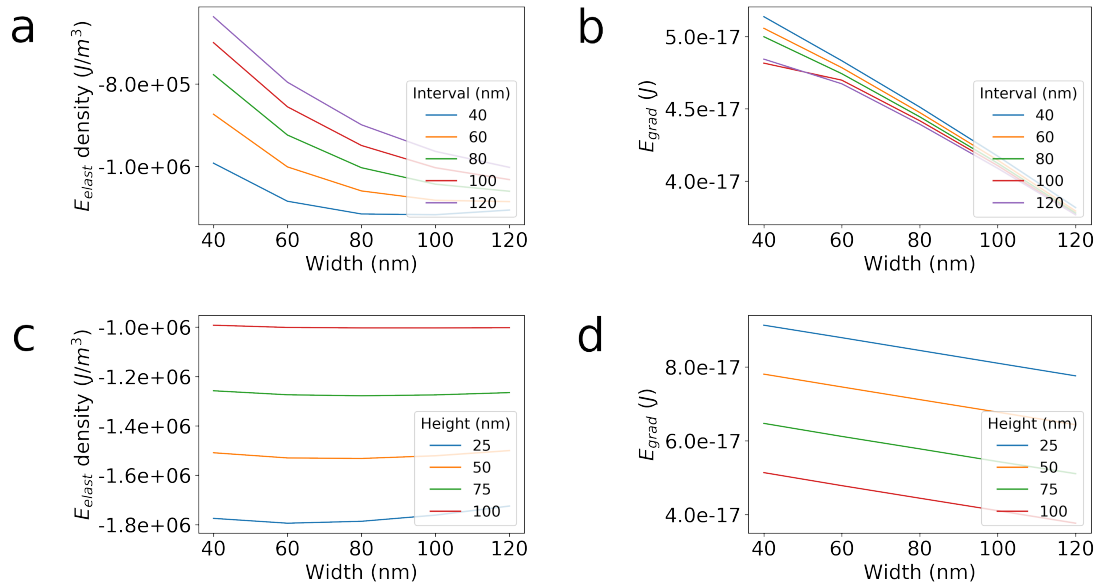


Figure 4.6. The elastic and gradient energy difference between Case 2 and Case 0. (a), (b) have the same setup as in Figure 4.4. (c), (d) have the same setup as in Figure 4.5.

The above analysis is for the domain setup Case 2, but to compare the relative stability of different domain configurations, we need to select a reference state and calculate the difference in energy between each of the configuration and the reference. The reference we choose is Case 0, in which no 71° domain appears above the charged defects. A subtraction of all other cases with Case 0 will give us the amount of elastic energy reduction due to the 71° strips over single domain state, as well as the amount of gradient energy increase

due to the type 1 and type 2 domain walls. Figure 4.6 shows the changes in elastic and gradient energy for Case 2 compared to Case 0. At a constant defect height, more elastic energy is released as the proportion of 71° domain increases. Thus the largest elastic energy reduction appears when width equals 120 nm, and interval equals 40 nm, as shown in Figure 4.6a. The energy difference in gradient part, as shown in Figure 4.6 b and d, is related to the two type 1, 71° , domain wall and one substitution of type 4, 109° , with type 2, 71° , charged domain wall. The gradient energy for type 1 domain wall is invariant as long as defect height is fixed, but the energies of type 4 and type 2 domain wall depend on the defect width. Since energy of type 2 wall is lower than type 4 wall, the lowest gradient energy in Figure 4.6b appears when defect width is the largest. In Figure 4.6c, when the defect width and interval ratio is kept constant, the elastic energy reduction is the same for a specific defect height, because the percentage of 71° domain is fixed. As the defect height increases, the volume of 71° above domain decreases, thus smaller elastic energy reduction. In Figure 4.6d, the trend in changes of gradient energy with defect width is the same as in Figure 4.6b. When defect height increases, the area of type 1 domain wall declines, thus the domain wall energy in Figure 4.6b becomes smaller.

Based on the previous analysis of different energy components and the difference between various setups with respect to the reference, there is a clear and direct relationship between the elastic energy, gradient energy and the defect width, interval, and height. To parameterize such relationships, we plot and fit all of the energies in Figure 4.7. In Figure 4.7a, a categorical scatter plot of all elastic energy difference between the studied cases (Case 1 to 4) and the reference state (Case 0). The fitting in the graph omits part of the data for Case 1, because some of the defect widths to interval ratio is larger than 1 which means the R3- (+,+, -) domain occupies more than 50% of the total width in x direction,

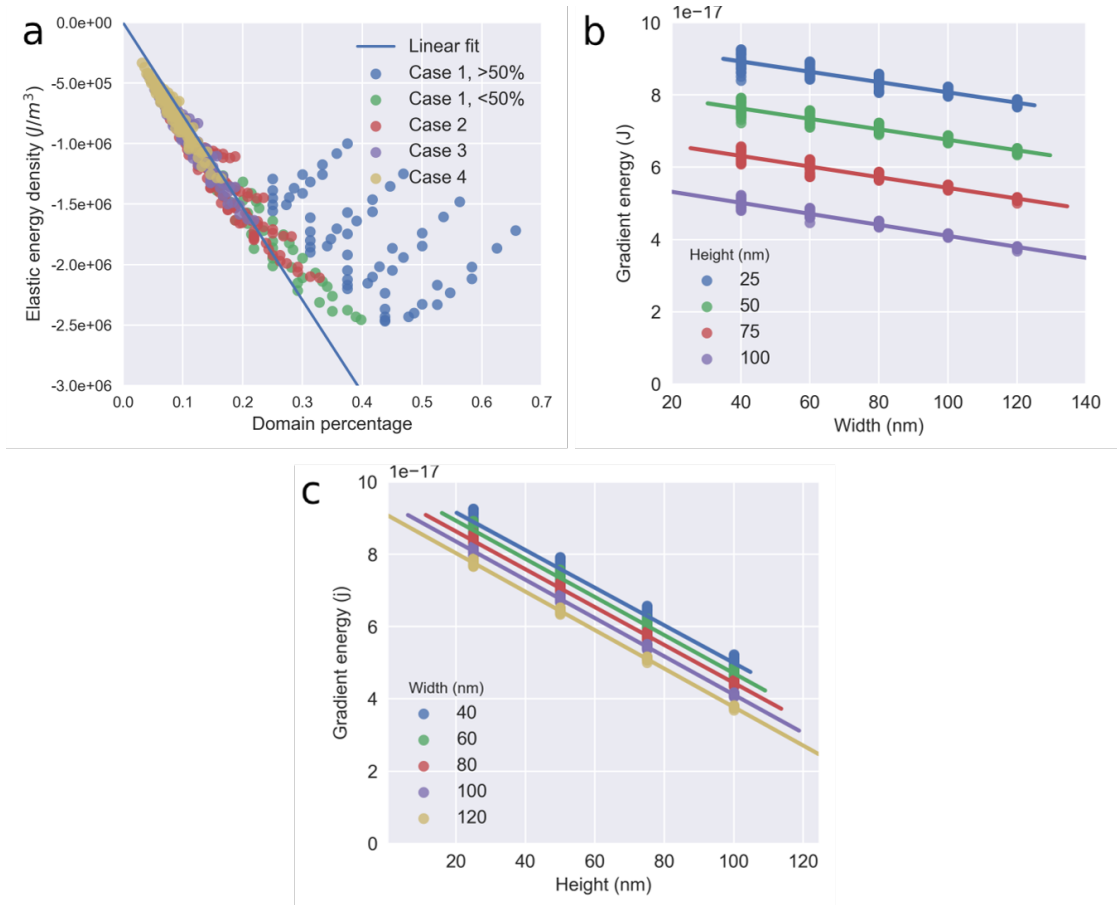


Figure 4.7. Linear fitting of energies for all simulation setups. (a) The linear relationship between elastic energy density and 71° domain percentage. (b) The gradient energy's relationship with defect width at various defect height. (c) The relationship between the gradient energy and the defect height at various defect width.

under which circumstances the elastic energy will increase as the defect width further rises. Thus, those blue points that represent cases when defect width is larger than half of the total width in Case 1 are not taken into account in our fitting. The function for the fitted line in Figure 4.7a is $\Delta E_E = -7.65 \times 10^6 * p(J/m^3)$, in which ΔE is the difference of elastic energy density with respect to the reference case and p is the percentage of R3-(+,+,-) domain in the system, the percentage is calculated by dividing the area of R3-domain with the cross-section area of the whole thin film. Figure 4.7b and c show the relationship between the gradient energy and the defect width and height, respectively.

The uniform shift between fitted lines in FIG 4.7b and c indicate that gradient energy is depending on both the width and the height linearly. If we plot the gradient energy on to the defect width and height coordinate, they should align on one plane. The expression for that plane is, $\Delta E_G = -0.685 \times 10^{-19} * w + 2.715 \times 10^{-19} * (h_f - h)(J)$, in which ΔE_G is the difference of gradient energy between the current configuration and the reference one, w is the defect width, h is the defect height, and h_f is the thickness of the thin film. Notice, the actual domain wall energy is twice of the gradient energy.

Knowing how the elastic energy, and domain wall energy changes with the defect configurations, we can easily predict what is the necessary defect setups that can lead to a 71° domain strip above the defect instead of a single domain, or vice versa. For example, if we want to obtain a 71° domain structure in a 200 nm BiFeO₃ thin film, what are the proper parameters for the defect? Let us assume the defect width and height is w and h , and we know film thickness is $h_f = 200$. Then $-7.65 \times 10^6 * w \times 10^{-9} * (200 - h) \times 10^{-9} + 2 * (-0.685 \times 10^{-19} * w + 2.715 \times 10^{-19} * (200 - h)) = 0$ will give you the condition when the elastic energy reduction equals the energy increase cause by additional 71° domain walls. The solution $w = \frac{-1.34407*(200-h)}{-0.0189195*(200-h)-0.339988}$ tells us that for a given defect height, which could be controlled by tuning the growth condition in the experiment, what is the minimal defect width to allow a 71° domain strips. If in experiment, we can control the defect to appear at the height of 100 nm, then the minimal defect width is about 60 nm, to allow the appearance of 71° domain above the defect.

We may also evaluate this problem based on a purely analytical model. To calculate the elastic energy release due to the introduction of 71° domain, we need to calculate the elastic energy for a single domain and 71° domain state and do a subtraction. The elastic energy reduction can be expressed as equation 4.5, capital W means the total width of

the whole system, P_s is the equilibrium polarization, for BiFeO₃ $P_s = 0.52$.

$$\begin{aligned}
& \left(\frac{1}{2} C_{44} (2Q_{44} P_s^2)^2 (W - w) (h_f - h) - \frac{1}{2} C_{44} (2Q_{44} P_s^2)^2 w (h_f - h) \right) \\
& - \frac{1}{2} C_{44} (2Q_{44} P_s^2)^2 W (h_f - h) \\
& = -\frac{1}{2} * C_{44} * (2Q_{44} P_s^2)^2 * 2w * (h_f - h)
\end{aligned} \tag{4.5}$$

Then, we can get energy density by normalizing the elastic energy with system size. Furthermore, if we put numerical values of the coefficients into the equation 4.5, we will get $-7.08 \times 10^6 * p(J/m^3)$, which is qualitatively consistent with the fitted equation from our simulation results.

For the domain wall energy increase due to the 71° domain, we can assume the domain wall thickness is 0.5 nm, and the energy can be expressed as equation 4.6.

$$\begin{aligned}
& 2 * \left[2 * \frac{1}{2} (G_{2323} (2P_s)^2 + G_{1212} (2P_s)^2) \sqrt{2} (h_f - h) \times 10^{-9} - \frac{1}{2} (G_{2323} (2P_s)^2) 2w \times 10^{-9} \right] \\
& = 2 * G (2P_s)^2 (2\sqrt{2} (h_f - h) - w)
\end{aligned} \tag{4.6}$$

If we put the numbers for the coefficients into equation 4.6, we will get $-1.465 \times 10^{-19} * w + 4.439 \times 10^{-19} * (h_f - h)(J)$. This is also qualitatively consistent with the relationship we fitted from phase-field calculations. The primary reason for the difference is that the domain wall thickness we used in the analytical model is oversimplified as previous publications have shown that the 71° domain wall may be thinner than 0.5 nm [136].

4.4 Conclusion

In summary, we perform high-throughput simulations varying the defect width, defect interval, and defect height within a 200 nm BiFeO₃ thin film. We explain the competition between elastic and domain wall energy through examining the difference for each free energy terms between various setups. We find that there is a linear relationship between the amount of elastic energy reduced, due to the introduction of twinning 71° domains above the defects, and the size of the 71° twinning domains, which is related to the defect width, interval, height, and film thickness. The gradient energy increase, that is due to the appearance of a pair of 71° domain walls between the twinning domains and the switching of 109° charged domain wall to 71° charged domain wall at the defect, is proportional to the area of the relevant domain walls, which is linearly depending on the defect height and width.

We obtain a criterion of defect configurations for the 71° domain strips to be stabilized above the planar charged defects in BiFeO₃ thin film, in other words, using the obtained equation, we can determine whether the system is dominated by elastic or domain wall energy given a specific defect width, interval, height, and film thickness. This work clearly demonstrates the possibility and capability of precise domain pattern control through defect engineering, which could be a viable route to the design and fabrication of more complicated ferroelectric nano-devices.

Chapter 5 |

The influence of defect topology on polarization distribution

5.1 Introduction

The primary characteristic of the ferroelectric material is a spontaneous polarization that can be switched by external applied field. Polarization domain structures can be formed in all ferroelectric materials, which determines the macroscopic piezoelectric and dielectric properties. This is a perfect example illustrating the microstructure and property relationship, and researchers have been testing a wide variety of techniques to obtain the correct polarization microstructure that has the optimum performance. Domain engineering, thus, becomes an important aspect for the usage of ferroelectric materials in real-life applications. Traditionally, domain engineering requires specific poling procedures at the macroscopic level [137]. Recently, researchers are exploring domain engineering at

nano-scale due to the increasing demand for novel nano-devices, as the semiconductor industry is approaching the physical limitation [2, 78]. For a similar reason, domain wall engineering is also proposed due to the domain wall's unique properties that are functionally different from the domains, such as the enhanced conductivity, photovoltaic, and ferroelectricity, etc. [121, 126, 138, 139]. The properties of different types of domain walls are also different. For example, in BiFeO_3 , the 71° domain wall is less conductive than the 109° domain wall [123], while 109° domain wall has a lower open circuit voltage in photovoltaic measurements [140]. To take the full advantage of the rich properties of the various domain walls, researchers are working on controlling the domain wall and the domain patterns as precisely as possible.

Among the multiple ways to perform domain or domain wall engineering at nano-scale, the one we focus on in this chapter is defect engineering [2, 78]. Defect exists universally across all materials, and according to the published researches, most defects have a significant influence on the performance of the ferroelectric material. For example, dislocations may interact and pin the domain walls leading to an increase in coercive field [120, 141–143], point defects may pin the domain wall [69, 144] and also may migrate according to the ferroelastic domain distribution and cause a shape change in P-E loop from single loop to double loop pattern [145], impurity defect or nonstoichiometry nano-regions may stabilize head-to-head domain wall and cause a complete change of the most stable domain patterns in thin film [2, 73]. The charged defect may not only influence the normal 109° and 71° domain wall, but also some novel topological polarization features, such as vortex, anti-vortex, hedgehog and anti-hedgehog [78]. These emergent domain states are previously only found to be stabilized through careful design of heterostructures and application of external electric field, and they exhibit novel properties different from

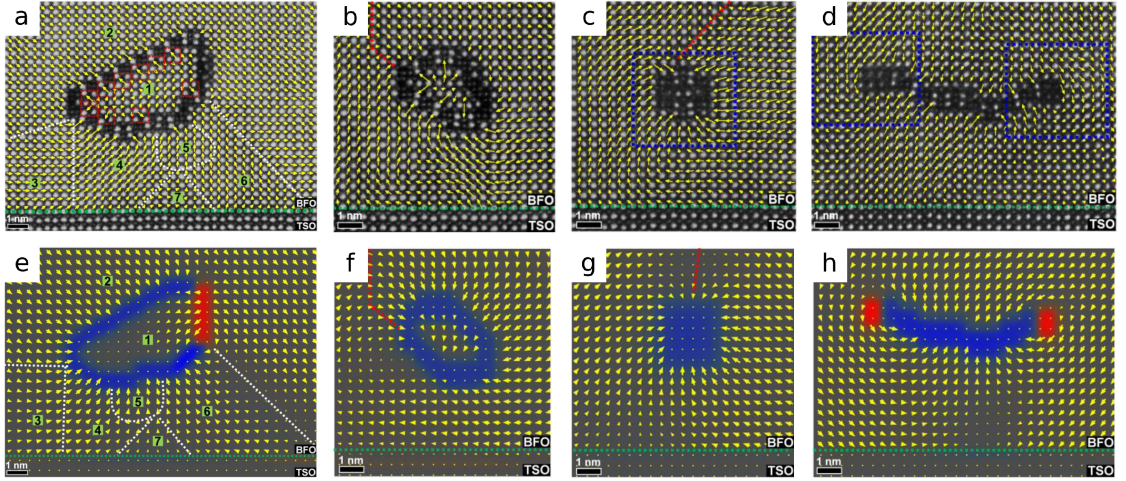


Figure 5.1. Comparison of polarization distribution around defects in experiment and simulation. (a, b, c, d) Polarization vector mapped from experimental HRTEM images. (e, f, g, h) the corresponding phase-field simulation results with the same setup as experimental observations.

a conventional domain wall [135, 146, 147].

This work is inspired by one of my collaborations with Dr. Linze Li from Dr. Xiaoqing Pan’s group, in which they manage to obtain HRTEM images with polarization mapping around several different charged nonstoichiometric nano-region, as it is shown in Figure 5.1. Through tuning of various parameters, I was able to verify our hypothesis about the charge distribution in experiment and reproduce almost perfectly results from the HRTEM data. It is during this process that I found polarization is very sensitive to some parameters, such as defect charge distribution, defect shape, electric boundary conditions, while insensitive to many other parameters, such as defect size and defect location.

Thus in this chapter, we investigate how the nonstoichiometry nano-region in BiFeO_3 thin film influences the local polarization distribution and try to answer the question of whether this is a viable way to control or engineer the occurrence of 109° domain and domain wall. We perform high-throughput simulations varying the defect width, defect location, defect thickness, electric boundary condition, and initial domain structure within a 100 nm BiFeO_3 thin film. We identify the factors that have the most significant effect on

polarization distribution and several configurations that can manipulate the 109° domain wall, thus could be useful for nanoscale domain engineering. Under the short circuit boundary condition, for a negative charged defect, we found that the defect thickness determines whether you can get a local hedgehog state around the defect. Varying the defect thickness also leads to a preference for the 180° or 109° domain below the defect. On the other hand, defect width and defect location have limited change on the final domain pattern. For net neutral charged defects, the domain pattern is relatively insensitive to defect location and defect thickness. It almost always favors a 109° domain above the defect except when the defect width is too small, and the final polarization state favors a single domain state. For those configurations that 109° domain wall is stabilized, the wall will be located precisely at the negative and positive junction of the defect, In the open circuit cases, we observe smaller domains and high density of domain walls compared to their short circuit counterparts, and interaction between the charged defect and the 109° domain wall or the flux closure triangular domain at the interface, We discovered that the initial domain structure, whether it is random noise or single domain, will affect the equilibrium polarization, indicating a possibility of experimental tricks such as small miscut angle or introduction of built-in potential may also contribute to the control of the as-grown domain pattern around the defect.

5.2 Materials and method

We used the phase-field method to evolve the polarization in BiFeO_3 thin film considering the existence of various types of charged defects. Phase-field is a mesoscale phenomenological model that excels in simulating microstructure evolution for all kinds of materials systems.

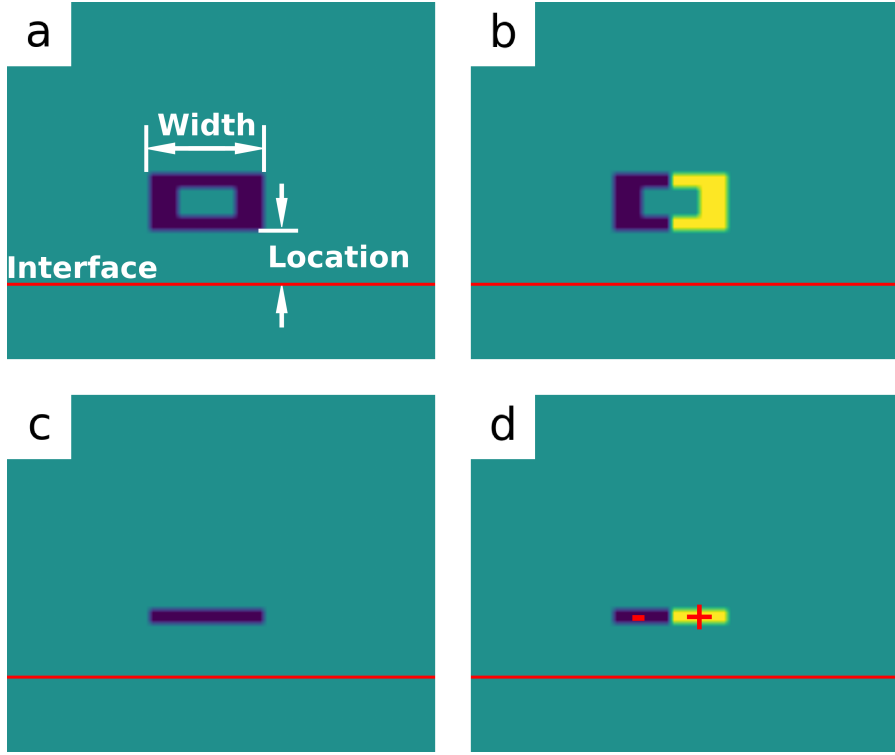


Figure 5.2. The 4 defect shapes that we have studied. Color represent the amount of defect charges we added, navy blue means negative charge, bright yellow means positive charge. (a) Case 1, loop shape, negatively charged defect. (b) Case 2, loop shape, neutrally charged defect. (c) Case 3, planar shape, negatively charged defect. (d) Case 4, planar shape, neutrally charged defect.

In the phase-field model for ferroelectrics, polarization is used as the order parameter that describes the whole simulation system. The Time Dependent Ginzburg Landau (TDGL) equation (5.1), Poisson equation (5.3), and mechanical equilibrium (5.5) are solved together considering the thin-film electrical and mechanical boundary conditions. All equations are solved using a semi-implicit fourier spectral method, and the boundary conditions are considered through a superposition method. We introduce charged defects into the simulation by adding a fixed source of charges, q^D , at the defect location to the right hand side of the Poisson equation (5.3). The amount of negative defect charges that we used is $-1.1 \times 10^9 C/m^3$. The defect is also a non-polar structure, so that the polarization within the defects are fixed as zero. Other BiFeO_3 materials coefficients that

we used can be found in Chapter 1.

$$\frac{\partial P_i}{\partial t} = \frac{\delta F}{\delta P_i}, (i = 1, 2, 3) \quad (5.1)$$

$$F = \int_V (f_{landau} + f_{elec} + f_{elas} + f_{grad}) dV \quad (5.2)$$

$$\nabla \cdot (\kappa \cdot \nabla \phi) = \frac{-P_{i,i} + q^D}{\epsilon_0} \quad (5.3)$$

$$\text{Short : } \phi|_{sur} = 0, \phi|_{int} = 0; \quad \text{Open : } D|_{sur} = 0, D|_{int} = 0 \quad (5.4)$$

$$C_{ijkl}(u_{k,lj} - \epsilon_{kl,j}^0) = 0, \sigma_{i3}|_{sur} = 0, u_i|_{bot} = 0 \quad (5.5)$$

In this work, the simulated thin film dimension is $lx = 102.4nm, ly = 0.4nm, lz = 100nm$, with a substrate thickness of $16nm$, and each the grid size used in simulation is $0.4nm$. We consider there is zero mismatch strain between the substrate and thin film with no built-in potential. As it is illustrated in Figure 5.2, we have a total of 4 different defect setups. Each defect is described by its type, position (distance from the interface), and width. For defect type 2 and 4 in Figure 5.2, the positive charged is chosen to be the same as the negative value which results in an overall zero charge for the whole defect. We performed a total of 360 high-throughput simulations varying the initial domain structure (random distribution with 3 different random seeds, and two single domain states, R1(+,+,+) and R2-(+,-)), defect position ($3.2nm, 6.4nm, 9.6nm$), defect width ($6.4nm, 9.6nm, 12.8nm$), defect type (4 types), and the electric boundary condition (open, short boundary condition, equation 5.4). All combinations are listed in Figure 5.3

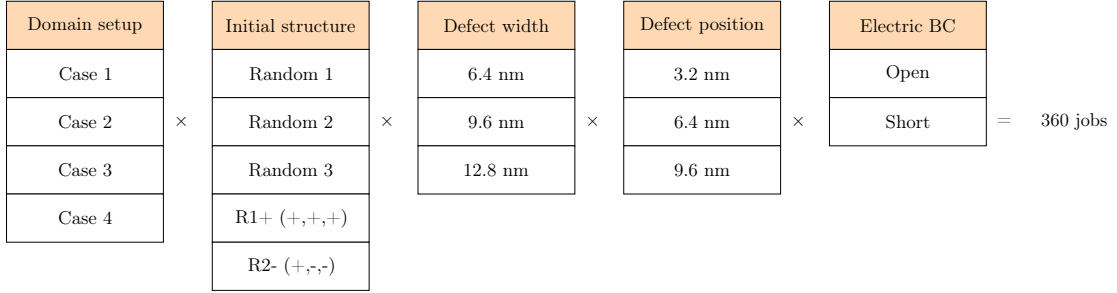


Figure 5.3. The parameter space that is explored with high-throughput simulations.

5.3 Results and discussion

The result in Figure 5.4 shows the influence of these defects on polarization under open and short electric boundary conditions. In general, due to the depolarization field, open circuit electric boundary condition will lead to 109° domain patterns with flux closure triangles near the surface and interface, while short circuit boundary condition will lead to a much large domain size. Thus we may expect to observe more domains in the open circuit cases than in the short circuit cases. For defect case 1, Figure 5.2(a), the polarization distribution for different initial random distribution of the same electric boundary condition resemble (or mirror with respect to $[100]$ plane) each other. Clearly, the upward and downward domain states are no longer degenerated, and the downward one is favored since the defect has a net negative charge. In the vicinity, a hedgehog type polarization pattern is formed in both open and short circuit case. In the open circuit case, the defect always appears between two 109° domain wall. In Figure 5.4 (a1, a2) the vortex formed by the 109° domain wall and triangle domain junction is 15 nm away from the defect. In the short circuit case, an anti-vortex core appears about 2 nm away from the defect, which is a byproduct of the hedgehog pattern.

For defect case 2, a loop defect with half positive and half negative charges, the most

obvious feature is the stabilization of a 109° domain wall right at the negative and positive charge junction. The stabilized 109° domain wall is universal in open circuit case, and occasional in the short circuit case. Depending on the initial random distribution, the 109° domain wall may not be able to go through to the top of the film, as shown in Figure 5.4(b4).

The results of defect case 3 and 4 under open circuit electric boundary condition also show some interaction with the 109° domain wall and the flux closure triangle domain near the interface but in a much less deterministic manner compared to the case 1 and 2. In the short circuit cases of defect type 3, due to the reduced defect thickness the hedgehog pattern and the anti-vortex core is no longer present, instead, only domain switching below the defect can be observed. While for defect type 4 short circuit condition, the domain around the defect remains approximately single domain with only local polarization rotation in the vicinity.

Figure 5.5 shows the results of all four defects with different initial polarization. For type 1 defect, the results can be classified into two groups, one is the R1+(+,+,+) initial type, that the defect causes domain on the left/right side and above the defect to switch, and an anti-vortex core appears above the defect. The other type is when starting from R2-(+,-,-) and random noises that the switched domain is below the defect with an anti-vortex core on its side. For defect case 2, the results can also be divided into two groups, one is starting from random initial, a 109° domain wall will be stabilized at the center above the defect and three 109° domain walls below the defect. Another group is starting from single domains and the polarization pattern will remain mostly single domain above the defect and a thin strip of 109° switched domain below the defect.

For defect case 3, the classification is similar to case 1, but due to the reduced thickness

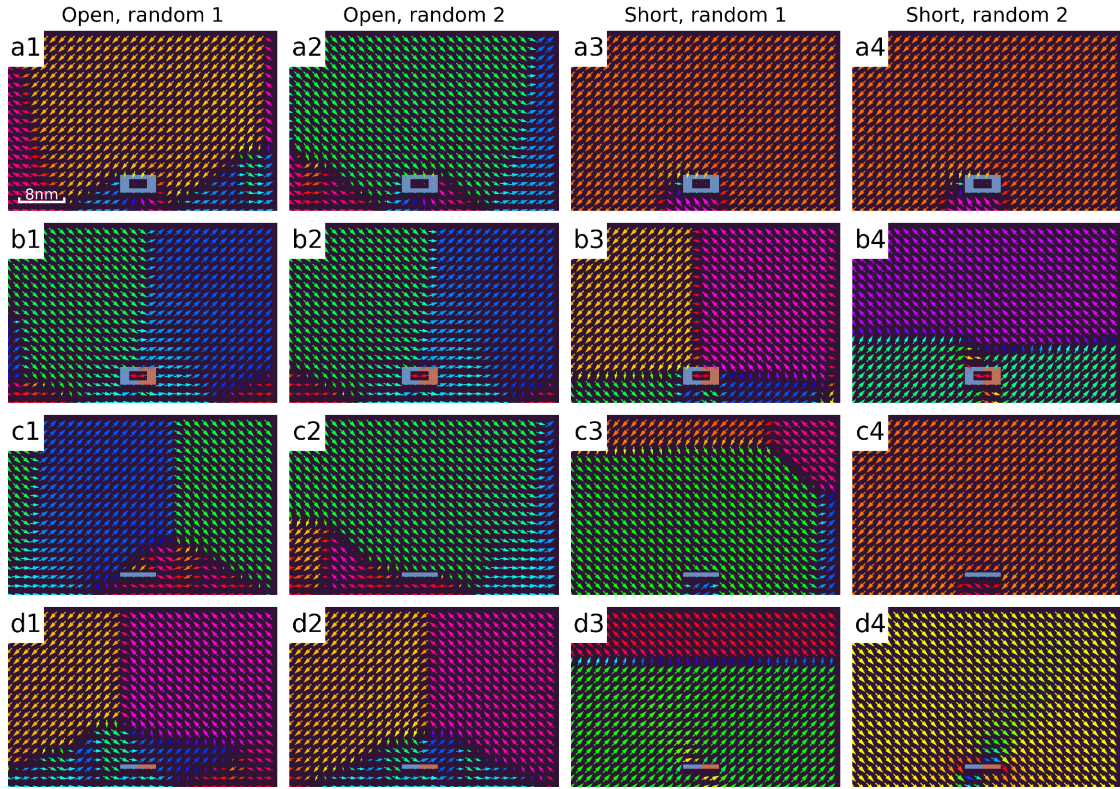


Figure 5.4. Simulation results under open circuit and short circuit electric boundary conditions. All other defect configurations are controlled to be the same. Defect width is 6.4 nm. Defect location is 3.2 nm away from the interface. All simulations are starting from random but with different random seeds. The arrows illustrate the direction and magnitude of the polarization, and the background color represent the defect charges.

of the defect, now in the R1+ case, polarization remains mostly in a single domain state. For other initial setups, the switched domain is strictly below the defect with no hedgehog or anti-vortex state. These results indicate that the thickness of the defect plays an important role which we will discuss later. For the defect case 4, the polarization is always in a single domain state for both above and below the defect in all different types of initial domain structure.

Figure 5.6 shows how the defect location, that is the distance from interface, is affecting the final domain structure. In all short circuit cases, there are no difference between various defect height except for the fact that everything is shifted upward when the

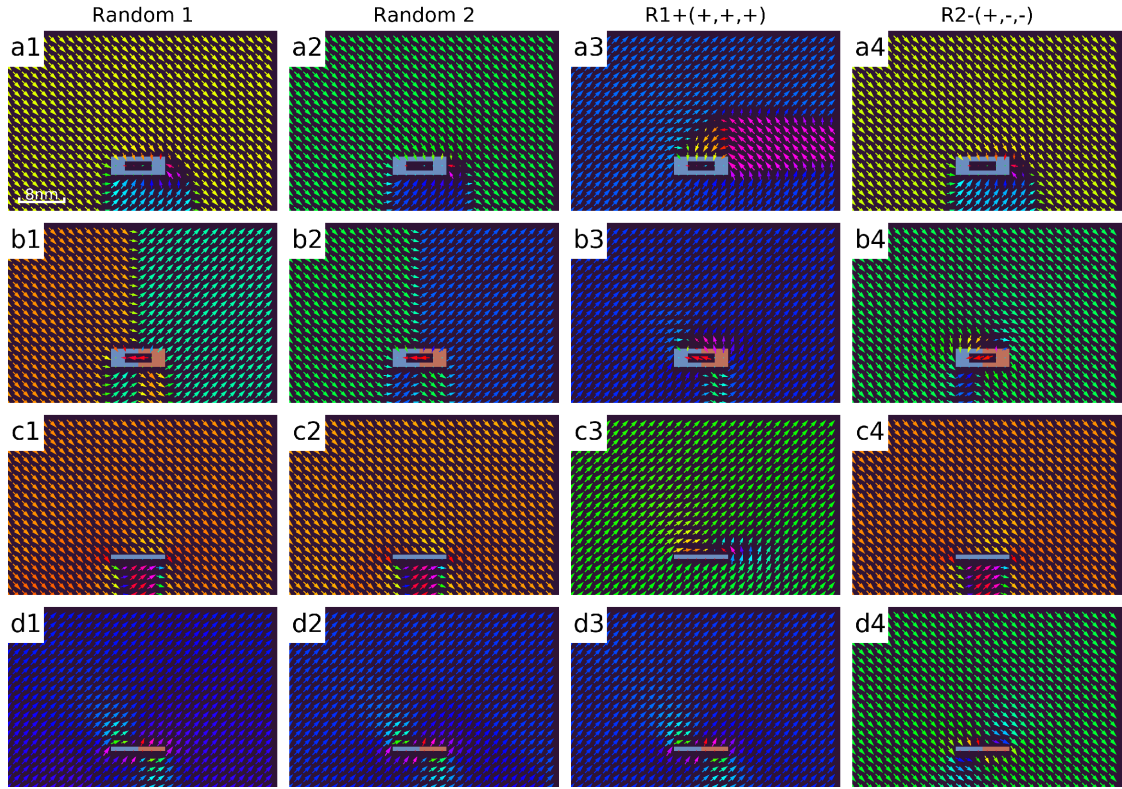


Figure 5.5. Phase-field simulation results starting from different initial conditions, two random polarization distribution, initial R1+ (+,+,+) domain, and initial R2- (+,-,-). All other defect configurations are controlled to be the same. Defect width is 9.6 nm. Defect height is 9.6 nm. Electric boundary condition is the short circuit boundary condition.

distance is larger. In the open circuit cases, for the thicker defects, type 1 and 2, the differences are still in the region below the defect that the switched domain becomes larger as the defect location rises. While for the two thinner defect cases, some more complicated changes appears. For defect case 3, it is clear that the negative defect is interacting with the flux closure triangle of 109° domain wall at the bottom interface, and when the defect location rises, it pushes the vortex core higher. For defect case 4, the 109° domain wall and the defect decoupled as the defect location decreases to 3.2 nm.

Figure 5.7 illustrates the role of defect width on determining the polarization distribution. For defect case 1, both short and long defect lead to a pattern qualitatively resemble each other. Under the open circuit condition, the flux closure core is about 4

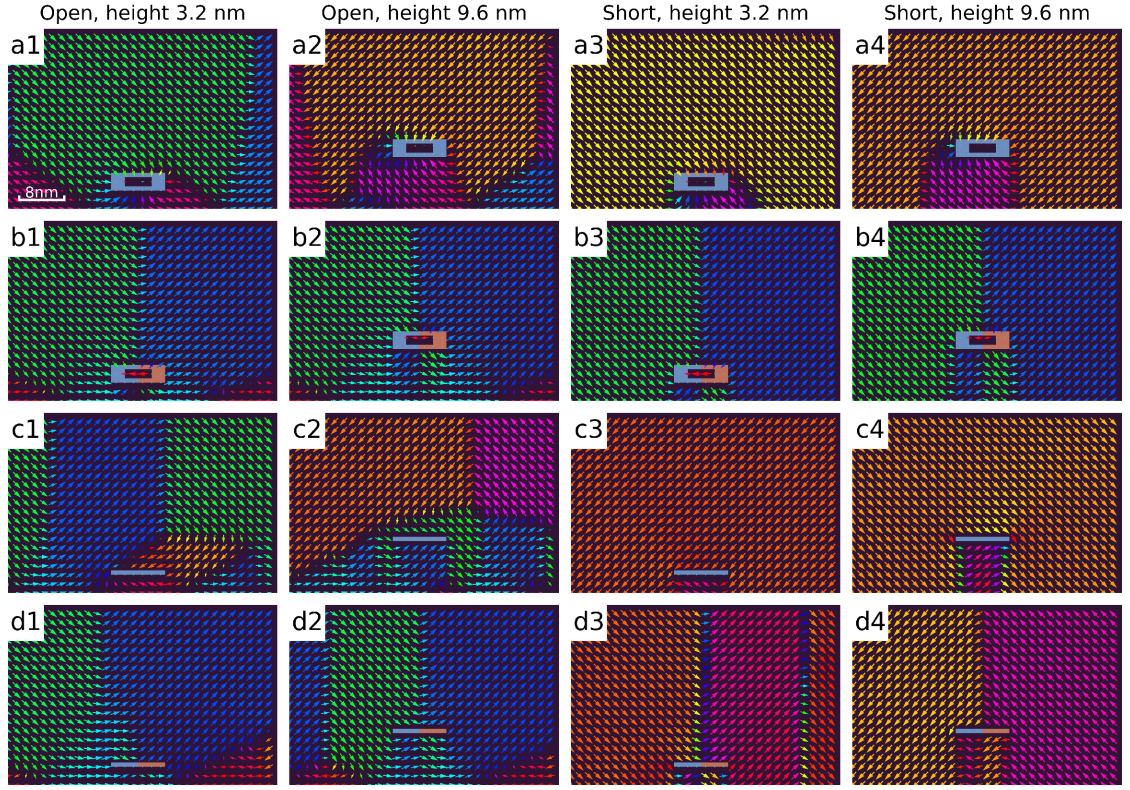


Figure 5.6. Polarization distribution for defects at various heights, 3.2 nm and 9.6 nm, and either open or short circuit electric boundary conditions. All simulations are starting from random initial polarization, with a defect width of 9.6 nm.

nm closer to the longer defect, and a small tetragonal region towards the defect can be observed below the defect in the 9.6 nm defect case. Under short circuit conditions, the difference is more trivial that longer defect simply leads to a wider 180° switched domain below the defect. For defect case 2, the primary feature, namely the 109° domain wall that is stabilized by the defect, can be observed regardless of the defect width and electric boundary condition. For defect case 3, open circuit condition, the 109° domain wall and the vortex core are fully decoupled with the defect as the it becomes longer. While under short circuit boundary condition, the polarization patterns near the defect are the same for the short and long defect. For defect case 4, open circuit condition, both the short and long defect can stabilize a 109° domain wall above them, while the 6.4 nm wide defect

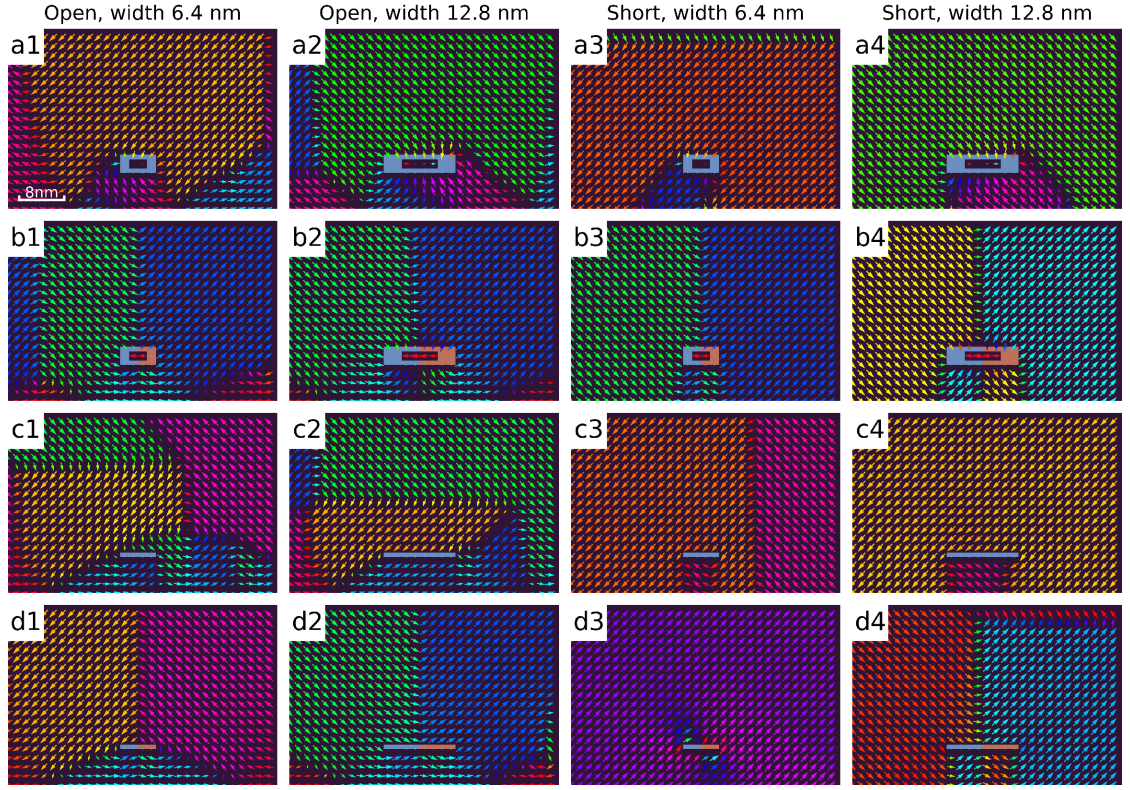


Figure 5.7. Polarization distribution for different defect width, 6.4 nm and 12.8 nm, and either open or short electric boundary conditions. All simulations are starting from random noise, with a defect height of 6.4 nm.

coincides with the flux closure core of the triangular domain and stabilize two sets of 109° domains, $R2-(+,-,-)/R1+(+,+,+)$ and $R1(-,-,-)/R2+(-,+,+)$. In the short circuit cases, 12.8 nm defect can stabilize a 109° domain wall above at the negative to positive charge junction, while 6.4 nm defect can only lead to local polarization rotation.

Another thing we would like to discuss is how the defect thickness is influencing the polarization distribution. Among all cases, the influence on polarization distribution is always stronger when the defect is thicker, features such as hedgehog domain state, anti-vortex core, and 109° domain wall are all strongly coupled to the thick defects. Thin defects, such as defect type 3 and 4, generally lead to a simpler domain states, without much topological polarization patterns. In the net negative charge cases, thick defect

results in a hedgehog pattern in the vicinity that is absent around the thin defect. In the open circuit cases, thicker defect has a more deterministic effect on the final polarization distribution, while in the short circuit cases, thick defect leads to both 180° and 109° domain switching and thin defect leads to only 109° domain switching. For the net zero charge cases, thickness of the defect doesn't affect the primary feature of the 109° domain wall above the defect, except for the 6.4 nm wide defect under short circuit conditions in which single domain is the most stable setup.

5.4 Conclusion

In summary, we have performed high-throughput simulations varying the defect width, defect location, defect thickness, electric boundary condition and initial domain structure within a 100 nm BiFeO_3 thin film. We identify the factors that has the most significant affect on local polarization distribution and overall domain patterns. These findings should be useful for nanoscale domain engineering in nano devices.

For net negative charged defect, type 1 and type 3, we found defect thickness determines whether you can get a locally hedgehog state around the defect. It also leads to different type of switching below the defect, 180° or 109° domain switching for the thick defect, and only 109° switching for the thin defect. The defect width and defect location have limited influence on the final domain pattern in the thick defect cases. While in the thin defect cases, the polarization distribution is completely different varying the defect width and location.

For net neutral charged defects, type 2 and 4, the domain pattern is relatively insensitive to defect location and defect thickness, while if the defect width is below some critical value, such as in the 3.2 nm cases, the final polarization states favors a single

domain rather than 109° domains.

We found that open circuit boundary condition will result in smaller domains and more domain walls than the short circuit counterpart. The initial domain structure will affect the equilibrium polarization, indicating the experimental tricks such as small miscut angle or introduction of built in potential may also help to obtain the desired local polarization distribution.

We have identified multiple ways to achieve the control of long range 109° domain walls, such as defect type 1 with open circuit boundary condition, defect type 2 under both open or short circuit condition, and defect type 4 that are longer than 6.4 nm under both open or short circuit condition. For defect type 1, the 109° domain wall is located at 5 to 15 nm away from the defect, while for defect type 2 and 4, the 109° domain wall always appears at the negative to positive charge junction of the defect. Thus, our simulation results of defect engineering enable researchers to gain control over the location of 109° domain wall which potentially could be one the tools for nanoscale domain and domain wall engineering.

Chapter 6 |

Conclusions and Future works

6.1 Conclusion

In this dissertation, we explore the polarization distribution with the presence of two types of defects in ferroelectrics, more specifically, dislocations in SrTiO₃ and nonstoichiometric nanoregion in BiFeO₃. We study how the elastic and electric effects due to the defects may contribute to the control of both local and long-range polarization distribution at the nanoscale, which will provide useful guidance to the future experimental studies of using defect to achieve domain and domain wall engineering in ferroelectric materials.

We study the role of flexoelectricity in inducing polarization at the dislocation core in SrTiO₃. Three types of dislocations, $b = a(100)$ edge dislocation, $b = \frac{a}{2}(110)$ edge dislocation, and $b = a(010)$ screw dislocation are considered. We find that flexoelectricity can stabilize orthorhombic-type polarization around $b = \frac{a}{2}(110)$ edge dislocation, and enhance the magnitude of the already existing tetragonal-type polarization in $b = a(100)$ edge dislocation case. Polarization value of about $0.18C/m^2$ and $0.14C/m^2$ can be obtained for the $b = a(100)$ edge dislocation and $b = \frac{a}{2}(110)$ edge dislocation case respectively. Our

study identifies the shear component of flexoelectric tensor contributes the most to the flexoelectric induce polarization around the edge dislocation cores. For $b = a(010)$ screw dislocation, we find neither electrostriction nor flexoelectricity is able to stabilize any polar state. Our simulation results complement existing experimental works for $b = a(100)$ edge dislocation by demonstrating explicitly the contribution of flexoelectricity and electrostriction and predict the polarization pattern around $b = \frac{a}{2}(110)$ edge dislocation and $b = a(010)$ screw dislocation that awaits future experimental verification.

We then study the defect charges effects on local polarization around the same three types of dislocations in SrTiO₃ single crystal. Using a negative defect charge estimated by experimental observations, we find that the charge induced polarization exists mainly within 5 nm region around the dislocation core, and peaks in less than 2 nm distance from the core. In the two edge dislocation cases, the flexoelectric and electrostrictive effects dominate over the defect charge's influences with a much large impacting region and large induced polarization magnitude. We find that the distribution of the defect charge induced polarization is highly anisotropic whose pattern is related to the tensile stress region around the edge dislocation. In the screw dislocation case, the situation reverses, as neither electrostriction nor flexoelectricity is able to stabilize any polar state, while the defect charges have similar effects as in the two edge dislocation cases. Since the screw dislocation stress only has shear components, the induced polarization pattern becomes almost isotropic D_4 symmetric pattern, with slightly larger polarization magnitude along the diagonal directions.

For the research of nonstoichiometric nano-region in BiFeO₃, we perform high-throughput simulations varying the defect width, defect interval, and defect height within a 200 nm BiFeO₃ thin film. We explain the reason why 71° domain strips may

form above the charged defect through a competition between elastic and domain wall energy. An empirical formula that describes the criteria of defect configurations for the 71° domain strips to appear above the defects in BiFeO_3 thin film is obtained. These simulations demonstrate the possibility of precise 71° domain pattern control through defect engineering, which could be a viable route to the design and fabrication of more ferroelectric nano-devices.

Next, we extend our simulation with more nonstoichiometric charged defect configurations, including the defect shape, such as planar defect and loop defect, the defect charge distribution, such as net negatively charged and neutrally charged, the initial domain structures, and the electric boundary conditions of the thin film. We investigate the domain patterns of the whole parameter space and identify multiple setups that stabilize 109° domain strips in thin film, such as thick negative charged defect with open circuit boundary condition, thick neutral charged defect under both open or short circuit condition, and planar neutral charged defect longer than 6.4 nm under both open or short circuit condition. These findings provide insights into the control of the location of 109° domain wall and thus may potentially be used as a building block towards the more complicated domain engineered nanoelectronic device.

Based on these simulation results, this dissertation expands the researcher's understanding of the nanoscale domain engineering through defects in ferroic materials. We demonstrate the possibilities of using dislocations in SrTiO_3 to stabilize a polar state and nonstoichiometric charged defects in BiFeO_3 to obtain either 71° or 109° domain patterns. We discuss the mechanism behind the defect's interaction with local and long-range polarization, thus providing a solid basis for designing more complicated domain engineering approaches. This work also demonstrates the capability of precise domain pattern control

through defect engineering, which could be a viable route to the design and fabrication of future ferroelectric nanoelectronic devices.

6.2 Future works

The current phase-field model and simulation provide a solid basis for the study of defect engineering in ferroelectrics. However, there is still a large room for improvement in terms of additional physical phenomenon, more complex defect setups, and switching dynamics. Several future directions are discussed below.

6.2.1 Dislocation dynamics in SrTiO₃

In our current model, we deliberately isolate a single static dislocation and study its influence on local polar states in SrTiO₃. Such simplification is based on the assumption that dislocations density in SrTiO₃ is low and immobile. This is fine in usual cases since SrTiO₃ is brittle, which means it will break if the dislocation can easily be generated, and the density becomes high. Our collaborators in Germany are now trying to make SrTiO₃ ductile and introduce more dislocations into the system. Nevertheless, our collaborators from Dr. Peng Gao's group at Peking University, Beijing, China, have confirmed in HRTEM that the dislocation due to plastic deformation ($\langle 110 \rangle$ partial dislocation) always comes in pairs. All of these experimental efforts urge us to extend our current phase-field model to include dislocation dynamics and couple with the polarization evolution. Researchers have proposed a phase-field model for dislocation dynamics of metal [119], but nobody has applied it to ferroelectric complex oxide yet. In situ temporal observation of 3D dislocation dynamics is already very difficult and can only be achieved using dark-field XRD according to several very recent publications [148]. The task to

characterize the dislocation movement and polarization evolution at the same time is currently impossible. Thus, the mesoscale phase-field simulation will play an important role in investigating this problem. It is interesting to know how the dislocations multiply, migrate, and react with each other in SrTiO_3 while the local polarization also coupled with the dislocation evolution through both electrostrictive and flexoelectric effect.

6.2.2 Free carrier evolution in SrTiO_3

In this dissertation, we considered the bound charges due to nonstoichiometry at the dislocation core and studied its interaction with local polarization. Here we made an assumption that the dislocation core is as insulating as the bulk crystal, which is not very accurate since several experimental works have claimed that the dislocation core can be viewed as a conducting filament in the insulating matrix. A more physically accurate and comprehensive phase-field model will need to take the free carrier generation, recombination, and migration into consideration. For SrTiO_3 , the free carrier species include electron, hole, and oxygen vacancy, all of which will interact with the dislocation core since the defects have both a charged core and locally distorted lattices. It will be very interesting if we can study how the defect's mechanical effect may affect the defect local charge density and thus the conductivity at dislocation core in SrTiO_3 .

Appendix |

Bulk, thin film and membrane elastic solver

1 Bulk homogeneous system

For a system that contains eigenstrains, the stress and strain relationship is as follows

$$\sigma_{ij} = C_{ijkl}\epsilon_{kl} = C_{ijkl}(\epsilon_{kl}^{tot} - \epsilon_{kl}^0) \quad (.1)$$

And the mechanical equilibrium conditions are

$$\sigma_{ij,j} = 0 \quad (.2)$$

These are 3 sets of equations with 6 unknowns (stresses).

We separate the solution into two parts, a homogeneous part that correspond to the macroscopic deformations, and a heterogeneous part correspond to the local deformation,

which means integration of η over space should equals to 0.

$$\epsilon_{kl}^{tot} = \bar{\epsilon}_{kl} + \eta_{ij} \quad (.3)$$

$$\sigma_{ij} = \bar{\sigma}_{ij} + s_{ij} \quad (.4)$$

Write out the expression for the homogeneous and heterogeneous stress

$$\bar{\sigma}_{ij} = C_{ijkl} \bar{\epsilon}_{kl} \quad (.5)$$

$$s_{ij} = C_{ijkl} (\eta_{kl} - \epsilon_{kl}^0) \quad (.6)$$

The original mechanical equilibrium equation (.2) becomes two.

$$C_{ijkl} \bar{\epsilon}_{kl,j} = 0 \quad (.7)$$

$$C_{ijkl} (\eta_{kl,j} - \epsilon_{kl,j}^0) = 0 \quad (.8)$$

The equation (.7) is the homogeneous part, and equation (.8) is the heterogeneous part.

1.1 The homogeneous(macroscopic) part

If user is controlling the average strain of the bulk system, then nothing needs to be solved.

If user is controlling the average stress of the bulk system, then the homogeneous strain needs to be calculated by applying the elastic compliance tensor to the homogeneous stress and plus the average eigenstrain.

1.2 The heterogeneous(microscopic) part

For the heterogeneous part, we substitute the strain with displacement, $\eta_{kl} = \frac{1}{2}(u_{k,l} + u_{l,k})$, to make it easier for us to solve. So now the equation that we are solving becomes:

$$C_{ijkl}u_{k,lj}(x, y, z) = C_{ijkl}\epsilon_{kl,j}^0(x, y, z) \quad (.9)$$

$$\Rightarrow -\zeta_l \zeta_j C_{ijkl} \tilde{u}_k(q_x, q_y, q_z) = I \zeta_j C_{ijkl} \tilde{\epsilon}_{kl}^0(q_x, q_y, q_z) \quad (.10)$$

To solve it numerically, we need to write out the matrix form of equation (.9)

$$g_{3 \times 3} \begin{pmatrix} \tilde{u}_1^A \\ \tilde{u}_2^A \\ \tilde{u}_3^A \end{pmatrix} = T_{3 \times 3 \times 3} \begin{bmatrix} \tilde{\epsilon}_{11}^0 & \tilde{\epsilon}_{12}^0 & \tilde{\epsilon}_{13}^0 \\ \tilde{\epsilon}_{22}^0 & \tilde{\epsilon}_{22}^0 & \tilde{\epsilon}_{23}^0 \\ \tilde{\epsilon}_{33}^0 & \tilde{\epsilon}_{32}^0 & \tilde{\epsilon}_{33}^0 \end{bmatrix} \quad (.11)$$

In which $g_{3 \times 3}$ is $g_{ik} = \zeta_l \zeta_j C_{ijkl}$ using the einstein summation. $T_{3 \times 3 \times 3}$ is $T_{ikl} = -I \zeta_j C_{ijkl}$ using einstein summation.

For those cases g matrix is invertable.

$$\begin{pmatrix} \tilde{u}_1 \\ \tilde{u}_2 \\ \tilde{u}_3 \end{pmatrix} = (g_{3 \times 3})^{-1} T_{3 \times 3 \times 3} \begin{bmatrix} \tilde{\epsilon}_{11}^0 & \tilde{\epsilon}_{12}^0 & \tilde{\epsilon}_{13}^0 \\ \tilde{\epsilon}_{22}^0 & \tilde{\epsilon}_{22}^0 & \tilde{\epsilon}_{23}^0 \\ \tilde{\epsilon}_{33}^0 & \tilde{\epsilon}_{32}^0 & \tilde{\epsilon}_{33}^0 \end{bmatrix} \quad (.12)$$

Notice that the blue and red 3s are different. We may define a tensor $H_{3 \times 3 \times 3}$ that $H_{ikl} = g_{ij}^{-1} T_{jkl}$, which is only related to stiffness, so can be calculated ahead of the main loop and save some time.

$$H_{3 \times 3 \times 3} = g_{3 \times 3}^{-1} T_{3 \times 3 \times 3} \quad (.13)$$

Since the strain tensor is symmetric, we may reduce it to a 6 component vector, and

$$\begin{pmatrix} \tilde{u}_1^A \\ \tilde{u}_2^A \\ \tilde{u}_3^A \end{pmatrix} = H_{3 \times 6} \begin{pmatrix} \tilde{\epsilon}_{11}^0 \\ \tilde{\epsilon}_{22}^0 \\ \tilde{\epsilon}_{33}^0 \\ \tilde{\epsilon}_{23}^0 \\ \tilde{\epsilon}_{13}^0 \\ \tilde{\epsilon}_{12}^0 \end{pmatrix} \quad (.14)$$

$$H_{3 \times 6} = \begin{bmatrix} g_{i1} \zeta_j C_{ij11} & g_{i1} \zeta_j C_{ij22} & g_{i1} \zeta_j C_{ij33} & 2g_{i1} \zeta_j C_{ij23} & 2g_{i1} \zeta_j C_{ij13} & 2g_{i1} \zeta_j C_{ij12} \\ g_{i2} \zeta_j C_{ij11} & g_{i2} \zeta_j C_{ij22} & g_{i2} \zeta_j C_{ij33} & 2g_{i2} \zeta_j C_{ij23} & 2g_{i2} \zeta_j C_{ij13} & 2g_{i2} \zeta_j C_{ij12} \\ g_{i3} \zeta_j C_{ij11} & g_{i3} \zeta_j C_{ij22} & g_{i3} \zeta_j C_{ij33} & 2g_{i3} \zeta_j C_{ij23} & 2g_{i3} \zeta_j C_{ij13} & 2g_{i3} \zeta_j C_{ij12} \end{bmatrix} \quad (.15)$$

Once the value of \mathbf{u} in fourier space is obtained, the final result can be easily calculated with a backward fourier transformation.

When at the origin point in the reciprocal space $\zeta_1^2 + \zeta_2^2 + \zeta_3^2 = 0$, the g matrix is not invertable, we need to treat it slightly differently. Since for the reciprocal origin point, it correspond to the uniform displacement of the whole object, which we already considered in the homogeneous (macroscopic) part, so here we will directly considered the $\tilde{\mathbf{u}} = 0$

2 Thin film homogeneous system

The thin film solver is an extension of the bulk solver, which is also made up of homogeneous and heterogeneous parts. The only difference is that for the heterogeneous part, now we need to have some boundary condition in the out-of-plane direction.

And the mechanical equilibrium condition along with boundary conditions are

$$\begin{cases} \sigma_{ij,j} & = 0 \\ \sigma_{i3}|_{x_3=h_f} & = \sigma_{i3}^{app} \\ u_i|_{x_3=-h_s} & = 0 \end{cases} \quad (.16)$$

2.1 The homogeneous(macroscopic) part

Different from the bulk case, in thin film scenario the homogeneous part must also satisfy the stress free boundary condition for free surface. Thus

$$\begin{cases} C_{ijkl}\bar{\epsilon}_{kl,j} = 0 \\ C_{i3kl}\bar{\epsilon}_{kl} = 0 \end{cases} \quad (.17)$$

The first equation of equation (.17) is always satisfied since the strain is uniform, so we only need to find a solution for the second equation. To solve it in computer, we need the matrix form and equation (.17) becomes

$$\begin{bmatrix} C_{1313} & C_{1323} & C_{1333} \\ C_{2313} & C_{2323} & C_{2333} \\ C_{3313} & C_{3323} & C_{3333} \end{bmatrix} \begin{pmatrix} \bar{\epsilon}_{13} \\ \bar{\epsilon}_{23} \\ \bar{\epsilon}_{33} \end{pmatrix} = - \begin{pmatrix} C_{1311}\bar{\epsilon}_{11} + C_{1322}\bar{\epsilon}_{22} + 2C_{1312}\bar{\epsilon}_{12} \\ C_{2311}\bar{\epsilon}_{11} + C_{2322}\bar{\epsilon}_{22} + 2C_{2312}\bar{\epsilon}_{12} \\ C_{3311}\bar{\epsilon}_{11} + C_{3322}\bar{\epsilon}_{22} + 2C_{3312}\bar{\epsilon}_{12} \end{pmatrix} \quad (.18)$$

Since we already know $\bar{\epsilon}_{11} = \bar{\epsilon}_{22} = \frac{a_s - a_f}{a_s}$ and $\bar{\epsilon}_{12} = 0$. We can easily solve it by multiplying the matrix inverse.

2.2 The heterogeneous(microscopic) part

Next is the heterogeneous part, equation (.9) plus the boundary conditions is what we are solving

$$\begin{cases} C_{ijkl}u_{k,lj} = C_{ijkl}\epsilon_{kl,j}^0 \\ C_{i3kl}(u_{k,l} - \epsilon_{kl}^0)|_{x_3=h_f} = \sigma_{i3}^{app} \\ u_i|_{x_3=-h_s} = 0 \end{cases} \quad (.19)$$

Equation (.19) are 3 sets of equations with 3 unknowns. To solve it, we will use the superposition method that split the equation and solution into two parts, first part takes care of the none-zero right-hand-side with 3D periodic boundary conditions that we are going to use 3D fourier transform to solve which we may call is part A, and second part with zero right-hand-side which we will apply 2D fourier transform of the in-plane direction and keep the third direction in real space to takes care of the specific thin film boundary conditions, and we may call it part B.

2.2.1 Part A: Non-zero rhs, periodic BC

For part A, it is simple, the equation to be solved is exactly the same as equation (.9), so we may reuse the code and results of the bulk heterogeneous part.

2.2.2 Part B: Zero-rhs, thin film BC

For part B, the boundary condition is now depending on the solution of part A.

$$\left\{ \begin{array}{l} C_{ijkl}u_{k,l}^B = 0 \\ C_{i3kl}u_{k,l}^B|_{x_3=h_f} = \sigma_{i3}^{app} - C_{i3kl}(u_{k,l}^A - \epsilon_{kl}^0)|_{x_3=h_f} \\ u_i^B|_{x_3=-h_s} = -u_i^A|_{x_3=-h_s} \end{array} \right. \quad (.20)$$

We perform a 2D fourier transform to the equation, $i, k = 1, 2, 3$ and $m, n = 1, 2$

$$C_{i3k3}u_{k,33}^{\tilde{B}} + I\zeta_m C_{i3km}u_{k,3}^{\tilde{B}} + I\zeta_n C_{ink3}u_{k,3}^{\tilde{B}} - \zeta_m \zeta_n C_{inkm}u_k^{\tilde{B}} = 0 \quad (.21)$$

This is a second order equation. When at the origin point of reciprocal space, the equation will have different general solution compared to not origin points. Here let's first dicuss when not at the origin point, what the solution will be. For each coordinate, since \mathbf{u} is a 3 dimension vector, so we are expecting a total of 6 solutions, and we need 6 boundary conditions. The general solutions to this equation are $u_k^{\tilde{B}}(q_1, q_2, x_3) = a_k e^{Ip\zeta x_3}$, $\zeta = \sqrt{\zeta_1^2 + \zeta_2^2}$. If we put the general solution back into the equation (.21) we will get the following equation, an eigenvalue problem, from which we can find the value for a and p. These are 3 independent equations of $i = 1, 2, 3$.

$$(-p^2\zeta^2 C_{i3k3} - p\zeta\zeta_m C_{i3km} - p\zeta\zeta_n C_{ink3} - \zeta_m \zeta_n C_{inkm})\mathbf{a}e^{Ip\zeta x_3} = 0 \quad (.22)$$

$$\Rightarrow (p^2 C_{i3k3} + p\frac{\zeta_m}{\zeta} C_{i3km} + p\frac{\zeta_n}{\zeta} C_{ink3} + \frac{\zeta_m}{\zeta} \frac{\zeta_n}{\zeta} C_{inkm})\mathbf{a} = 0 \quad (.23)$$

The part before \mathbf{a} is a 3 by 3 matrix. Solving its determinant equals 0 gives you the 6 eigenvalues.

There are other relatively easier way to solve this eigen value problem by introducing a second unknown that is related to the derivative of $\tilde{\mathbf{u}}$, thus augmenting the 3 by 3 matrix to 6 by 6 and treat it as a normal first order eigenvalue problem, which we can easily

solve using lapack.

There are multiple ways you can use to create the second unknown, and the most common one is simply define the new variable as $\tilde{\mathbf{s}} = \frac{\partial \mathbf{u}^B}{\partial x_3}$, then you can establish the following equations, in which $A = C_{i3k3}$, $B = I(\zeta_m C_{i3km} + \zeta_n C_{ink3})$, and $C = -\zeta_m \zeta_n C_{inkm}$

$$\begin{pmatrix} \frac{\partial \mathbf{u}^B}{\partial x_3} \\ \frac{\partial \tilde{\mathbf{s}}}{\partial x_3} \end{pmatrix} = \begin{bmatrix} 0 & I \\ A^{-1}C & -A^{-1}B \end{bmatrix} \begin{pmatrix} \mathbf{u}^B \\ \tilde{\mathbf{s}} \end{pmatrix} \quad (.24)$$

This is just $y' = Ay$, which you can insert the general solution into it and transform it into an eigenvalue problem.

The second way to create the unknown is to use a more meaningful value, that is the stress, which is also related to the derivative of displacement, and this is what we did in the program as well as Dr. Li's 2002 paper. Subscript $i, k = 1, 2, 3$ and $m, n = 1, 2$

$$\sigma_{i3}^B = C_{i3k3} u_{k,3}^B + C_{i3k1} u_{k,1}^B + C_{i3k2} u_{k,2}^B \quad (.25)$$

$$\Rightarrow \tilde{\sigma}_{i3}^B = C_{i3k3} \tilde{u}_{k,3}^B + I \zeta_m C_{i3km} \tilde{u}_k^B \quad (.26)$$

$$\Rightarrow \tilde{u}_{k,3}^B = C_{i3k3}^{-1} \tilde{\sigma}_{i3}^B - I C_{i3k3}^{-1} \zeta_m C_{i3km} \tilde{u}_k^B \quad (.27)$$

And the derivative of σ_{i3} is

$$\sigma_{i3,3}^B = C_{i3k3} u_{k,33}^B + C_{i3k1} u_{k,13}^B + C_{i3k2} u_{k,23}^B \quad (.28)$$

$$\Rightarrow \tilde{\sigma}_{i3,3}^B = C_{i3k3} \tilde{u}_{k,33}^B + I \zeta_m C_{i3km} \tilde{u}_{k,3}^B \quad (.29)$$

$$\begin{aligned} \Rightarrow \tilde{\sigma}_{i3,3}^B &= -(I \zeta_m C_{i3km} \tilde{u}_{k,3}^B + I \zeta_n C_{ink3} \tilde{u}_{k,3}^B - \zeta_m \zeta_n C_{inkm} \tilde{u}_k^B) \\ &\quad + I \zeta_m C_{i3km} \tilde{u}_{k,3}^B \end{aligned} \quad (.30)$$

$$\Rightarrow \tilde{\sigma}_{i3,3}^B = \zeta_m \zeta_n C_{inkm} \tilde{u}_k^B - I \zeta_n C_{ink3} \tilde{u}_{k,3}^B \quad (.31)$$

$$\Rightarrow \sigma_{i3,3}^{\tilde{B}} = \zeta_m \zeta_n C_{inkm} u_k^{\tilde{B}} - I \zeta_n C_{ink3} (C_{i3k3}^{-1} \sigma_{13}^{\tilde{B}} - I C_{i3k3}^{-1} \zeta_m C_{i3km} u_k^{\tilde{B}}) \quad (.32)$$

$$\Rightarrow \sigma_{i3,3}^{\tilde{B}} = (\zeta_m \zeta_n C_{inkm} - \zeta_n C_{ink3} C_{i3k3}^{-1} \zeta_m C_{i3km}) u_k^{\tilde{B}} - I \zeta_n C_{ink3} C_{i3k3}^{-1} \sigma_{i3}^{\tilde{B}} \quad (.33)$$

Combining equation (.27) and equation (.33) gives us

$$\begin{pmatrix} \frac{\partial u^{\tilde{B}}}{\partial x_3} \\ \frac{\partial \sigma^{\tilde{B}}}{\partial x_3} \end{pmatrix} = \begin{bmatrix} -I C_{13k3}^{-1} \zeta_m C_{i3km} & C_{i3k3}^{-1} \\ \zeta_m \zeta_n C_{inkm} - \zeta_n C_{ink3} C_{i3k3}^{-1} \zeta_m C_{i3km} & -I \zeta_n C_{ink3} C_{i3k3}^{-1} \end{bmatrix} \begin{pmatrix} u^{\tilde{B}} \\ \sigma^{\tilde{B}} \end{pmatrix} \quad (.34)$$

Insert the general solution of $u_k^{\tilde{B}}(q_1, q_2, x_3) = a_k e^{Ip\zeta x_3}$, $\zeta = \sqrt{\zeta_1^2 + \zeta_2^2}$ into the expression of $\sigma_{i3}^{\tilde{B}}$ and we will get

$$\sigma_{i3}^{\tilde{B}} = (p C_{i3k3} + \frac{\zeta_m}{\zeta} C_{i3km}) I \zeta a_k e^{Ip\zeta x_3} \quad (.35)$$

$$\sigma_{i3}^{\tilde{B}} = I \zeta b_i e^{Ip\zeta x_3}, \quad b_i = (p C_{i3k3} + \frac{\zeta_m}{\zeta} C_{i3km}) a_k \quad (.36)$$

We may use W, R, U to represent those tensor coefficients for our convenience.

$$U_{ik} = C_{i3k3}, \quad R_{ik} = C_{ink3} \frac{\zeta_n}{\zeta}, \quad W_{ik} = C_{inkm} \frac{\zeta_m}{\zeta} \frac{\zeta_n}{\zeta}.$$

Insert the general solution for $u^{\tilde{B}}$ and $\sigma^{\tilde{B}}$ into equation (.34)

$$\begin{pmatrix} Ip\zeta \mathbf{a} \\ -p\zeta^2 \mathbf{b} \end{pmatrix} = \begin{bmatrix} -IU^{-1}R^T\zeta & U^{-1} \\ (W\zeta^2 - \zeta RU^{-1}\zeta R^T) & -I\zeta RU^{-1} \end{bmatrix} \begin{pmatrix} \tilde{\mathbf{a}} \\ I\tilde{\zeta} \mathbf{b} \end{pmatrix} \quad (.37)$$

$$p \begin{pmatrix} \tilde{\mathbf{a}} \\ \tilde{\mathbf{b}} \end{pmatrix} = \begin{bmatrix} -U^{-1}R^T & U^{-1} \\ -W + RU^{-1}R^T & -RU^{-1} \end{bmatrix} \begin{pmatrix} \tilde{\mathbf{a}} \\ \tilde{\mathbf{b}} \end{pmatrix} \quad (.38)$$

For better numerical accuracy, you may want to rescale the W, R and U matrix before solving for eigenvalues and eigenvectors, than scale the solution back at the end. We choose

$\frac{1}{C_{44}}$ or $\frac{1}{C_{2323}}$ as the rescaling factor. $W_D = W/C_{2323}$, $U_D = U/C_{2323}$, $R_D = R/C_{2323}$ and equation (.38) becomes

$$p \begin{pmatrix} \tilde{\mathbf{a}} \\ C_{2323}\tilde{\mathbf{b}} \end{pmatrix} = \begin{bmatrix} -U_D^{-1}R_D^T & U_D^{-1} \\ -W_D + R_DU_D^{-1}R_D^T & -R_DU_D^{-1} \end{bmatrix} \begin{pmatrix} \tilde{\mathbf{a}} \\ C_{2323}\tilde{\mathbf{b}} \end{pmatrix} \quad (.39)$$

\mathbf{b} is related to \mathbf{a} , $\tilde{\mathbf{b}} = (pU + R^T)\tilde{\mathbf{a}}$. This is a normal eigenvalue problem, which we can call lapack to solve. Since it is a second order three component equation, we know the 6 sets of eigenvalues and eigenvectors, must be three pairs of conjugated complex numbers and vectors.

Solution to this eigenvalue problem is something we can do ahead of main loop. Now suppose we have got the eigenvalue p_i and eigenvector $\mathbf{v}_i = (\mathbf{a}_i, \mathbf{b}_i)$. Linear combination of the general solutions gives you the final solution for equation (.34)

$$\tilde{\mathbf{u}}^B = \sum_{i=1}^3 q_i \mathbf{a}_i e^{I\zeta p_i x_3} \quad (.40)$$

$$\tilde{\mathbf{s}}^B = \sum_{i=4}^6 q_i I\zeta C_{2323} \mathbf{b}_i e^{I\zeta p_i x_3} \quad (.41)$$

Put the boundary conditions into it, and we consider $x_3 = 0$ is at the interface of substrate and thin film, so thin film surface is at $x_3 = h_f$, and the boundary in substrate

is at $x_3 = -h_s$.

$$\begin{pmatrix} \tilde{u}_1^B|_{x_3=-h_s} \\ \tilde{u}_2^B|_{x_3=-h_s} \\ \tilde{u}_3^B|_{x_3=-h_s} \\ \frac{\tilde{\sigma}_{13}^B}{I\zeta C_{2323}}|_{x_3=h_f} \\ \frac{\tilde{\sigma}_{23}^B}{I\zeta C_{2323}}|_{x_3=h_f} \\ \frac{\tilde{\sigma}_{33}^B}{I\zeta C_{2323}}|_{x_3=h_f} \end{pmatrix} = \mathbf{P} \begin{pmatrix} q_1 \\ q_2 \\ q_3 \\ q_4 \\ q_5 \\ q_6 \end{pmatrix} \quad (.42)$$

Expression of \mathbf{P} is as follows, $a_i(j)$ is the j th component of the i th eigenvector (but only part of the eigenvector, b is the other part).

$$\begin{bmatrix} a_1(1)e^{-I\zeta P_1 h_s} & a_2(1)e^{-I\zeta P_2 h_s} & a_3(1)e^{-I\zeta P_3 h_s} & a_4(1)e^{-I\zeta P_4 h_s} & a_5(1)e^{-I\zeta P_5 h_s} & a_6(1)e^{-I\zeta P_6 h_s} \\ a_1(2)e^{-I\zeta P_1 h_s} & a_2(2)e^{-I\zeta P_2 h_s} & a_3(2)e^{-I\zeta P_3 h_s} & a_4(2)e^{-I\zeta P_4 h_s} & a_5(2)e^{-I\zeta P_5 h_s} & a_6(2)e^{-I\zeta P_6 h_s} \\ a_1(3)e^{-I\zeta P_1 h_s} & a_2(3)e^{-I\zeta P_2 h_s} & a_3(3)e^{-I\zeta P_3 h_s} & a_4(3)e^{-I\zeta P_4 h_s} & a_5(3)e^{-I\zeta P_5 h_s} & a_6(3)e^{-I\zeta P_6 h_s} \\ b_1(1)e^{I\zeta P_1 h_f} & b_2(1)e^{I\zeta P_2 h_f} & b_3(1)e^{I\zeta P_3 h_f} & b_4(1)e^{I\zeta P_4 h_f} & b_5(1)e^{I\zeta P_5 h_f} & b_6(1)e^{I\zeta P_6 h_f} \\ b_1(2)e^{I\zeta P_1 h_f} & b_2(2)e^{I\zeta P_2 h_f} & b_3(2)e^{I\zeta P_3 h_f} & b_4(2)e^{I\zeta P_4 h_f} & b_5(2)e^{I\zeta P_5 h_f} & b_6(2)e^{I\zeta P_6 h_f} \\ b_1(3)e^{I\zeta P_1 h_f} & b_2(3)e^{I\zeta P_2 h_f} & b_3(3)e^{I\zeta P_3 h_f} & b_4(3)e^{I\zeta P_4 h_f} & b_5(3)e^{I\zeta P_5 h_f} & b_6(3)e^{I\zeta P_6 h_f} \end{bmatrix} \quad (.43)$$

In real practice, you may need to rescale matrix \mathbf{P} for numerically better accuracy, and then after the matrix inversion times the scaling factor back to get the real answer. The one we used is $e^{-\zeta h w_0}$ in which $h = \max(h_s, h_f)$, $w_0 = \max(|p_i|)$. Now we may use lapack to solve for value of q . We can create the $e^{-\zeta h w_0} \mathbf{P}$ matrix in the setup phase, and only solve for the inverse inside main loop.

$$\begin{pmatrix} q'_1 \\ q'_2 \\ q'_3 \\ q'_4 \\ q'_5 \\ q'_6 \end{pmatrix} = (e^{-\zeta h w_0} \mathbf{P})^{-1} \begin{pmatrix} \tilde{u}_1^B \\ \tilde{u}_2^B \\ \tilde{u}_3^B \\ \frac{\sigma_{13}^B}{I\zeta C_{2323}} \\ \frac{\sigma_{23}^B}{I\zeta C_{2323}} \\ \frac{\sigma_{33}^B}{I\zeta C_{2323}} \end{pmatrix} \quad (.44)$$

Once we get the coefficient q , we can put it back into equation (.40) and derivative of (.40), also don't forget to apply the rescaling factor back.

$$\begin{pmatrix} \tilde{u}_1^B \\ \tilde{u}_2^B \\ \tilde{u}_3^B \\ \tilde{u}_{1,3}^B \\ \tilde{u}_{2,3}^B \\ \tilde{u}_{3,3}^B \end{pmatrix} = e^{-\zeta h w_0} \mathbf{Q} \begin{pmatrix} q_1 \\ q_2 \\ q_3 \\ q_4 \\ q_5 \\ q_6 \end{pmatrix} \quad (.45)$$

Expression for \mathbf{Q} is as follows, x_3 is the coordinate in out-of-plane direction with substrate and film interface as 0.

$$\begin{bmatrix} a_1(1)e^{I\zeta p_1 x_3} & a_2(1)e^{I\zeta p_2 x_3} & a_3(1)e^{I\zeta p_3 x_3} & a_4(1)e^{I\zeta p_4 x_3} & a_5(1)e^{I\zeta p_5 x_3} & a_6(1)e^{I\zeta p_6 x_3} \\ a_1(2)e^{I\zeta p_1 x_3} & a_2(2)e^{I\zeta p_2 x_3} & a_3(2)e^{I\zeta p_3 x_3} & a_4(2)e^{I\zeta p_4 x_3} & a_5(2)e^{I\zeta p_5 x_3} & a_6(2)e^{I\zeta p_6 x_3} \\ a_1(3)e^{I\zeta p_1 x_3} & a_2(3)e^{I\zeta p_2 x_3} & a_3(3)e^{I\zeta p_3 x_3} & a_4(3)e^{I\zeta p_4 x_3} & a_5(3)e^{I\zeta p_5 x_3} & a_6(3)e^{I\zeta p_6 x_3} \\ I\zeta p_1 a_1(1)e^{I\zeta p_1 x_3} & I\zeta p_2 a_2(1)e^{I\zeta p_2 x_3} & I\zeta p_3 a_3(1)e^{I\zeta p_3 x_3} & I\zeta p_4 a_4(1)e^{I\zeta p_4 x_3} & I\zeta p_5 a_5(1)e^{I\zeta p_5 x_3} & I\zeta p_6 a_6(1)e^{I\zeta p_6 x_3} \\ I\zeta p_1 a_1(2)e^{I\zeta p_1 x_3} & I\zeta p_2 a_2(2)e^{I\zeta p_2 x_3} & I\zeta p_3 a_3(2)e^{I\zeta p_3 x_3} & I\zeta p_4 a_4(2)e^{I\zeta p_4 x_3} & I\zeta p_5 a_5(2)e^{I\zeta p_5 x_3} & I\zeta p_6 a_6(2)e^{I\zeta p_6 x_3} \\ I\zeta p_1 a_1(3)e^{I\zeta p_1 x_3} & I\zeta p_2 a_2(3)e^{I\zeta p_2 x_3} & I\zeta p_3 a_3(3)e^{I\zeta p_3 x_3} & I\zeta p_4 a_4(3)e^{I\zeta p_4 x_3} & I\zeta p_5 a_5(3)e^{I\zeta p_5 x_3} & I\zeta p_6 a_6(3)e^{I\zeta p_6 x_3} \end{bmatrix} \quad (.46)$$

The full strain tensor in reciprocal space is

$$\tilde{\epsilon}_{11}^B = I\zeta_1 \tilde{u}_1^B \quad (.47)$$

$$\tilde{\epsilon}_{22}^B = I\zeta_2 \tilde{u}_2^B \quad (.48)$$

$$\tilde{\epsilon}_{33}^B = \tilde{u}_{3,3}^B \quad (.49)$$

$$\tilde{\epsilon}_{23}^B = 0.5(\tilde{u}_{2,3}^B + I\zeta_2 \tilde{u}_3^B) \quad (.50)$$

$$\tilde{\epsilon}_{13}^B = 0.5(\tilde{u}_{1,3}^B + I\zeta_1 \tilde{u}_3^B) \quad (.51)$$

$$\tilde{\epsilon}_{12}^B = 0.5(I\zeta_2 \tilde{u}_1^B + I\zeta_1 \tilde{u}_2^B) \quad (.52)$$

Above is only solution for cases not at the fourier space origin point. If at the origin point, things are a lot more easier. The equation (.21) becomes

$$C_{i3k3} \tilde{u}_{k,33}^B = 0 \quad (.53)$$

The general solution for equation (.53) is a linear function $\tilde{u}_k^B = A_k x_3 + B_k$. Apply the boundary conditions in (.20), \mathbf{BC}^u is the displacement boundary condition and \mathbf{BC}^σ is the stress boundary condition.

$$\left\{ \begin{array}{l} B\tilde{C}_1^u = A_1(-h_s) + B_1 \\ B\tilde{C}_2^u = A_2(-h_s) + B_2 \\ B\tilde{C}_3^u = A_3(-h_s) + B_3 \\ B\tilde{C}_{13}^\sigma = C_{1313}A_1 + C_{1323}A_2 + C_{1333}A_3 \\ B\tilde{C}_{23}^\sigma = C_{2313}A_1 + C_{2323}A_2 + C_{2333}A_3 \\ B\tilde{C}_{33}^\sigma = C_{3313}A_1 + C_{3323}A_2 + C_{3333}A_3 \end{array} \right. \quad (.54)$$

$$\Rightarrow \begin{pmatrix} A_1 \\ A_2 \\ A_3 \end{pmatrix} = U^{-1} \begin{pmatrix} B\tilde{C}_{13}^\sigma \\ B\tilde{C}_{23}^\sigma \\ B\tilde{C}_{33}^\sigma \end{pmatrix} \quad (.55)$$

$$\Rightarrow \left\{ \begin{array}{l} B_1 = B\tilde{C}_1^u - A_1(-h_s) \\ B_2 = B\tilde{C}_2^u - A_2(-h_s) \\ B_3 = B\tilde{C}_3^u - A_3(-h_s) \end{array} \right. \quad (.56)$$

Put the values back into the general solution, and we get

$$\begin{pmatrix} \tilde{u}_1^B \\ \tilde{u}_2^B \\ \tilde{u}_3^B \end{pmatrix} = \frac{U_D^{-1}}{C_{2323}} \begin{pmatrix} B\tilde{C}_{13}^\sigma \\ B\tilde{C}_{23}^\sigma \\ B\tilde{C}_{33}^\sigma \end{pmatrix} (x_3 - h_s) + \begin{pmatrix} B\tilde{C}_1^u \\ B\tilde{C}_2^u \\ B\tilde{C}_3^u \end{pmatrix} \quad (.57)$$

The strain is

$$\tilde{\epsilon}_{11}^B = 0 \quad (.58)$$

$$\tilde{\epsilon}_{22}^B = 0 \quad (.59)$$

$$\tilde{\epsilon}_{12}^B = 0 \quad (.60)$$

$$\begin{pmatrix} \tilde{\epsilon}_{33}^B \\ \tilde{\epsilon}_{23}^B \\ \tilde{\epsilon}_{13}^B \end{pmatrix} = U^{-1} \begin{pmatrix} B\tilde{C}_{13}^\sigma \\ B\tilde{C}_{23}^\sigma \\ B\tilde{C}_{33}^\sigma \end{pmatrix} = \frac{U_D^{-1}}{C_{2323}} \begin{pmatrix} B\tilde{C}_{13}^\sigma \\ B\tilde{C}_{23}^\sigma \\ B\tilde{C}_{33}^\sigma \end{pmatrix} \quad (.61)$$

Perform an inverse Fourier transform, and we get the part B of the heterogeneous displacement. Adding up all three parts, the homogeneous part, the heterogeneous part A and heterogeneous part B will give us the final solution. Notice, if you're using the denominator U_D , then remember to time the denominator back.

3 Membrane homogeneous system

For a membrane, the procedure of how to solve mechanical equilibrium is very similar to the thin film case, split the whole system into homogeneous and heterogeneous part, and then further separate the heterogeneous part into A and B.

Membrane is different from thin film in that there is either no substrate (free standing) or the substrate is not bonded to the film and only for a supporting purpose. From coding or solver point of view, the major differences lie in the homogeneous part, and the heterogeneous part B.

3.1 The homogeneous(macroscopic) part

Different from the thin film case, which we use the three mismatch strain as input to calculate the macroscopic deformation(strain), for membrane (or beam) it is a lot more complicated. In order to keep a good generality for our library solver, I think pass in the

deflection distribution is a good choice, as we can use it to further calculate the stress and strain distribution.

Suppose we have the plate deflection of w , for thin membrane (thickness less than $1/5$ of the curvature), we can use the Kirchhoff-love plate theory, with the two assumption, a material segment which is initially normal to the mid-surface remains straight and normal to the deformed middle surface; and the plate is inextensible in the z direction.

$$\left\{ \begin{array}{l} \epsilon_{11} = -z \frac{\partial^2 w}{\partial x^2} \\ \epsilon_{22} = -z \frac{\partial^2 w}{\partial y^2} \\ \epsilon_{33} = 0 \\ \epsilon_{23} = 0 \\ \epsilon_{13} = 0 \\ \epsilon_{12} = -2z \frac{\partial^2 w}{\partial x \partial y} \end{array} \right. \quad (.62)$$

For the thick plate case, there is the Mindlin theory, which extends the Kirchhoff-love theory but requires more input, deflection w , rotation of cross-section along x and y axes θ_x, θ_y . You may notice that (.62) is a special case of (.63) that $\theta_x = \frac{\partial w}{\partial y}$ and $\theta_y = -\frac{\partial w}{\partial x}$, which is true when the curvature of the bended plate is very large.

$$\left\{ \begin{array}{l} \epsilon_{11} = z \frac{\partial \theta_y}{\partial x} \\ \epsilon_{22} = -z \frac{\partial \theta_x}{\partial y} \\ \epsilon_{33} = 0 \\ \epsilon_{23} = -\theta_x + \frac{\partial w}{\partial y} \\ \epsilon_{13} = \theta_y + \frac{\partial w}{\partial x} \\ \epsilon_{12} = z \left(\frac{\partial \theta_y}{\partial y} - \frac{\partial \theta_x}{\partial x} \right) \end{array} \right. \quad (.63)$$

Use the simply supported center load beam as an example

$$\delta = -\frac{Fx}{48EI} (3L^2 - 4x^2) \quad (.64)$$

$$\theta_y = -\frac{F}{16EI} (L^2 - 4x^2) \quad (.65)$$

$$\theta_x = 0 \quad (.66)$$

3.2 The heterogeneous(microscopic) part

Next is the heterogeneous part, The reason we still define the boundary at $-h_s$ and h_f is for the purpose of reusing most part of our thin film solver.

$$\left\{ \begin{array}{l} C_{ijkl} u_{k,lj} = C_{ijkl} \epsilon_{kl,j}^0 \\ C_{i3kl} (u_{k,l} - \epsilon_{kl}^0)|_{x_3=h_f} = \sigma_{i3}^{app} \\ C_{i3kl} (u_{k,l} - \epsilon_{kl}^0)|_{x_3=-h_s} = 0 \end{array} \right. \quad (.67)$$

To solve equation (.67), we will use the superposition method that split the equation and solution into two parts exactly the same way as in the thin film case. Notice the σ_{i3}^{app} is not what cause the macroscopic deformation, it is the part in addition to any load that

cause the macroscopic deformation.

3.2.1 Part A: Zero rhs, periodic BC

Exactly the same as in the thin film case.

3.2.2 Part B: Non-zero rhs, membrane BC

Same until equation (.42), since the boundary conditions are different, so now the following equations are needed to solve for the linear combination coefficients.

$$\begin{pmatrix} \frac{\tilde{\sigma}_{13}^B}{I\zeta C_{2323}} \Big|_{x_3=-h_s} \\ \frac{\tilde{\sigma}_{23}^B}{I\zeta C_{2323}} \Big|_{x_3=-h_s} \\ \frac{\tilde{\sigma}_{33}^B}{I\zeta C_{2323}} \Big|_{x_3=-h_s} \\ \frac{\tilde{\sigma}_{13}^B}{I\zeta C_{2323}} \Big|_{x_3=h_f} \\ \frac{\tilde{\sigma}_{23}^B}{I\zeta C_{2323}} \Big|_{x_3=h_f} \\ \frac{\tilde{\sigma}_{33}^B}{I\zeta C_{2323}} \Big|_{x_3=h_f} \end{pmatrix} = \mathbf{P} \begin{pmatrix} q_1 \\ q_2 \\ q_3 \\ q_4 \\ q_5 \\ q_6 \end{pmatrix} \quad (.68)$$

Expression of \mathbf{P} is as follows, $b_i(j)$ is the j th component of the i th eigenvector.

$$\begin{bmatrix} b_1(1)e^{I\zeta P_1 - h_s} & b_2(1)e^{I\zeta P_2 - h_s} & b_3(1)e^{I\zeta P_3 - h_s} & b_4(1)e^{I\zeta P_4 - h_s} & b_5(1)e^{I\zeta P_5 - h_s} & b_6(1)e^{I\zeta P_6 - h_s} \\ b_1(2)e^{I\zeta P_1 - h_s} & b_2(2)e^{I\zeta P_2 - h_s} & b_3(2)e^{I\zeta P_3 - h_s} & b_4(2)e^{I\zeta P_4 - h_s} & b_5(2)e^{I\zeta P_5 - h_s} & b_6(2)e^{I\zeta P_6 - h_s} \\ b_1(3)e^{I\zeta P_1 - h_s} & b_2(3)e^{I\zeta P_2 - h_s} & b_3(3)e^{I\zeta P_3 - h_s} & b_4(3)e^{I\zeta P_4 - h_s} & b_5(3)e^{I\zeta P_5 - h_s} & b_6(3)e^{I\zeta P_6 - h_s} \\ b_1(1)e^{I\zeta P_1 h_f} & b_2(1)e^{I\zeta P_2 h_f} & b_3(1)e^{I\zeta P_3 h_f} & b_4(1)e^{I\zeta P_4 h_f} & b_5(1)e^{I\zeta P_5 h_f} & b_6(1)e^{I\zeta P_6 h_f} \\ b_1(2)e^{I\zeta P_1 h_f} & b_2(2)e^{I\zeta P_2 h_f} & b_3(2)e^{I\zeta P_3 h_f} & b_4(2)e^{I\zeta P_4 h_f} & b_5(2)e^{I\zeta P_5 h_f} & b_6(2)e^{I\zeta P_6 h_f} \\ b_1(3)e^{I\zeta P_1 h_f} & b_2(3)e^{I\zeta P_2 h_f} & b_3(3)e^{I\zeta P_3 h_f} & b_4(3)e^{I\zeta P_4 h_f} & b_5(3)e^{I\zeta P_5 h_f} & b_6(3)e^{I\zeta P_6 h_f} \end{bmatrix} \quad (.69)$$

In real practice, you may need to rescale matrix \mathbf{P} for numerically better accuracy, and then after the matrix inversion times the scaling factor back to get the real answer. The one we used is $e^{-\zeta h w_0}$ in which $h = \max(h_s, h_f)$, $w_0 = \max(|p_i|)$. Now we may use lapack to solve for value of q . We can create the $e^{-\zeta h w_0} \mathbf{P}$ matrix in the setup phase, and

only solve for the inverse inside main loop.

$$\begin{pmatrix} q'_1 \\ q'_2 \\ q'_3 \\ q'_4 \\ q'_5 \\ q'_6 \end{pmatrix} = (e^{-\zeta h w_0} \mathbf{P})^{-1} \begin{pmatrix} \frac{\tilde{\sigma}_{13}^B}{I\zeta C_{2323}} \Big|_{x_3=-h_s} \\ \frac{\tilde{\sigma}_{23}^B}{I\zeta C_{2323}} \Big|_{x_3=-h_s} \\ \frac{\tilde{\sigma}_{33}^B}{I\zeta C_{2323}} \Big|_{x_3=-h_s} \\ \frac{\tilde{\sigma}_{13}^B}{I\zeta C_{2323}} \Big|_{x_3=h_f} \\ \frac{\tilde{\sigma}_{23}^B}{I\zeta C_{2323}} \Big|_{x_3=h_f} \\ \frac{\tilde{\sigma}_{33}^B}{I\zeta C_{2323}} \Big|_{x_3=h_f} \end{pmatrix} \quad (.70)$$

Then everything afterwards are exactly the same as the thin film heterogeneous part B, that is put the coefficient q back to calculation the displacement and strain expression. $q'_i = e^{-\zeta h w_0} q_i$, so remember to time the scaling factor back for the final answer.

Notice for the origin point of fourier space, we also need to treat it separately. The equation (.21) becomes

$$C_{i3k3} \tilde{u}_{k,33}^B = 0 \quad (.71)$$

The general solution for equation (.71) is a linear function $\tilde{u}_k^B = A_k x_3 + B_k$. Apply the boundary conditions in (.20), \mathbf{BC}^σ is the stress boundary condition, since now both two boundaries are Neumann condition, the constant B_k cannot be determined, thus solution is not unique, meaning any translation in 3D space is acceptable, and we can simply use $B_k = 0$ as our result.

$$\begin{cases} B\tilde{C}_{13}^\sigma = C_{1313}A_1 + C_{1323}A_2 + C_{1333}A_3 \\ B\tilde{C}_{23}^\sigma = C_{2313}A_1 + C_{2323}A_2 + C_{2333}A_3 \\ B\tilde{C}_{33}^\sigma = C_{3313}A_1 + C_{3323}A_2 + C_{3333}A_3 \end{cases} \quad (.72)$$

$$\Rightarrow \begin{pmatrix} A_1 \\ A_2 \\ A_3 \end{pmatrix} = U^{-1} \begin{pmatrix} B\tilde{C}_{13}^\sigma \\ B\tilde{C}_{23}^\sigma \\ B\tilde{C}_{33}^\sigma \end{pmatrix} \quad (.73)$$

Put the values back into the general solution, and we get

$$\begin{pmatrix} \tilde{u}_1^B \\ \tilde{u}_2^B \\ \tilde{u}_3^B \end{pmatrix} = \frac{U_D^{-1}}{C_{2323}} \begin{pmatrix} B\tilde{C}_{13}^\sigma \\ B\tilde{C}_{23}^\sigma \\ B\tilde{C}_{33}^\sigma \end{pmatrix} x_3 \quad (.74)$$

The strain is

$$\tilde{\epsilon}_{11}^B = 0 \quad (.75)$$

$$\tilde{\epsilon}_{22}^B = 0 \quad (.76)$$

$$\tilde{\epsilon}_{12}^B = 0 \quad (.77)$$

$$\begin{pmatrix} \tilde{\epsilon}_{33}^B \\ \tilde{\epsilon}_{23}^B \\ \tilde{\epsilon}_{13}^B \end{pmatrix} = U^{-1} \begin{pmatrix} B\tilde{C}_{13}^\sigma \\ B\tilde{C}_{23}^\sigma \\ B\tilde{C}_{33}^\sigma \end{pmatrix} = \frac{U_D^{-1}}{C_{2323}} \begin{pmatrix} B\tilde{C}_{13}^\sigma \\ B\tilde{C}_{23}^\sigma \\ B\tilde{C}_{33}^\sigma \end{pmatrix} \quad (.78)$$

Perform an inverse Fourier transform, and we get the part B of the heterogeneous displacement. Adding up all three parts, the homogeneous part, the heterogeneous part A and heterogeneous part B will give us the final solution. Notice, if you're using the denominated U_D , then remember to time the denominator back.

4 Bulk inhomogeneous system

We call a system inhomogeneous, indicating that the elastic modulus is no longer a constant but a spatial distribution. In this case, if we still want to use the fourier spectral method to solve the mechanical equilibrium equation, then an iterative method will be needed.

We are still solving for this equation

$$\sigma_{ij,j} = 0 \quad (.79)$$

and the stress strain relationship is still valid.

$$\sigma_{ij} = C_{ijkl}\epsilon_{kl} = C_{ijkl}(\epsilon_{kl}^{tot} - \epsilon_{kl}^0) \quad (.80)$$

We still need to split the solution into two parts the macroscopic and microscopic part.

$$\epsilon_{kl}^{tot} = \bar{\epsilon}_{kl} + \eta_{ij} \quad (.81)$$

$$\sigma_{ij} = \bar{\sigma}_{ij} + s_{ij} \quad (.82)$$

But now the C_{ijkl} is no longer a number (or tensor) but a distribution, and the way we split the problem into homogeneous and heterogeneous part is different from the bulk homogeneous system in section (1).

$$C_{ijkl} = C_{ijkl}^0 + \delta C_{ijkl} \quad (.83)$$

$$\bar{\sigma}_{ij} = C_{ijkl}^0 \bar{\epsilon}_{kl} \quad (.84)$$

$$s_{ij} = C_{ijkl}(\eta_{kl} - \epsilon_{kl}^0) + \delta C_{ijkl} \bar{\epsilon}_{kl} \quad (.85)$$

The (.79) becomes

$$C_{ijkl}^0 \epsilon_{kl,j} = 0 \quad (.86)$$

$$C_{ijkl}^0 (\eta_{kl,j} - \epsilon_{kl,j}^0) = - \frac{\partial [\delta C_{ijkl} (\bar{\epsilon}_{kl} + \eta_{kl} - \epsilon_{kl}^0)]}{\partial x_j} \quad (.87)$$

For the bulk inhomogeneous system, choosing C_{ijkl}^0 is a tricky task, you can choose what ever you want, but it will influence the stability of your solver. Two common choice of C_{ijkl}^0 is the average and maximum value.

4.1 The homogeneous (macroscopic) part

Similar to section (1.1), you don't really need to solve for the homogeneous part for this bulk case. One thing we need to pay attention is that integration of our heterogeneous solution η no longer guarantee to be 0, which means each time we get the solution of total strain and we need to modify it so that constraint of average strain or stress still holds valid.

If we are controlling the average strain, then we need to calculate the current average total strain, compute its difference from the constraint value, and add such difference to the current total strain. If we are controlling the average stress, we need to calculate the current average stress, compute its difference from the constraint stress and calculate the corresponding changes of strain needed to keep average stress at the constraint value, then modify the total strain accordingly. Notice here the elastic modulus used is the average

value, which could be different from the C_{ijkl}^0 .

$$\delta\sigma_{ij} = \sigma_{ij}^{app} - \bar{\sigma}_{ij} \quad (.88)$$

$$\delta\epsilon_{kl} = (C_{ijkl}^-)^{-1}\delta\sigma_{ij} \quad (.89)$$

$$\epsilon_{kl}^{tot} = \epsilon_{kl}^{tot} + \delta\epsilon_{kl} \quad (.90)$$

4.2 The heterogeneous (microscopic) part

For the heterogeneous part, we will also substitute the strain with displacement in (.87),

$\eta_{kl} = \frac{1}{2}(u_{k,l} + u_{l,k})$, and we get:

$$C_{ijkl}^0 u_{k,lj} = C_{ijkl}^0 \epsilon_{kl,j}^0 - \frac{\partial[\delta C_{ijkl}(\bar{\epsilon}_{kl} + u_{k,lj} - \epsilon_{kl}^0)]}{\partial x_j} \quad (.91)$$

$$C_{ijkl}^0 u_{k,lj} = \frac{\partial[C_{ijkl}^0 \epsilon_{kl}^0 - \delta C_{ijkl}(\bar{\epsilon}_{kl} + u_{k,lj})]}{\partial x_j} \quad (.92)$$

$$\Rightarrow -\zeta_l \zeta_j C_{ijkl}^0 \tilde{u}_k = I \zeta_j \tilde{\sigma}_{ij}^\dagger \quad (.93)$$

$$\sigma_{ij}^\dagger = C_{ijkl}^0 \epsilon_{kl}^0 - \delta C_{ijkl}(\bar{\epsilon}_{kl} + u_{k,lj}) \quad (.94)$$

The u on the left side is unknown of current iteration, and the u on the right side is the displacement from last iteration. To write it more clearly:

$$-\zeta_l \zeta_j C_{ijkl}^0 \tilde{u}_k^n = I \zeta_j \tilde{\sigma}_{ij}^{\dagger,n-1} \quad (.95)$$

$$\sigma_{ij}^{\dagger,n-1} = C_{ijkl}^0 \epsilon_{kl}^0 - \delta C_{ijkl}(\bar{\epsilon}_{kl} + u_{k,lj}^{n-1}) \quad (.96)$$

We can write out the matrix form of equation (.91)

$$g_{3 \times 3} \begin{pmatrix} \tilde{u}_1^A \\ \tilde{u}_2^A \\ \tilde{u}_3^A \end{pmatrix} = T_{1 \times 3} \begin{bmatrix} \tilde{\sigma}_{11}^\dagger & \tilde{\sigma}_{12}^\dagger & \tilde{\sigma}_{13}^\dagger \\ \tilde{\sigma}_{21}^\dagger & \tilde{\sigma}_{22}^\dagger & \tilde{\sigma}_{23}^\dagger \\ \tilde{\sigma}_{31}^\dagger & \tilde{\sigma}_{32}^\dagger & \tilde{\sigma}_{33}^\dagger \end{bmatrix} \quad (.97)$$

In which $g_{3 \times 3}$ is $g_{ik} = \zeta_l \zeta_j C_{ijkl}^0$ using the einstein summation. $T_{1 \times 3} = -I[\zeta_1, \zeta_2, \zeta_3]$.

For those cases g matrix that is invertable.

$$\begin{pmatrix} \tilde{u}_1 \\ \tilde{u}_2 \\ \tilde{u}_3 \end{pmatrix} = (g_{3 \times 3})^{-1} T_{1 \times 3} \begin{bmatrix} \tilde{\sigma}_{11}^\dagger & \tilde{\sigma}_{12}^\dagger & \tilde{\sigma}_{13}^\dagger \\ \tilde{\sigma}_{21}^\dagger & \tilde{\sigma}_{22}^\dagger & \tilde{\sigma}_{23}^\dagger \\ \tilde{\sigma}_{31}^\dagger & \tilde{\sigma}_{32}^\dagger & \tilde{\sigma}_{33}^\dagger \end{bmatrix} \quad (.98)$$

We may define a tensor $H_{3 \times 3 \times 3}$ that $H_{ikl} = g_{ij}^{-1} T_k$, which can be calculated ahead of the main loop and save some time.

$$H_{3 \times 3 \times 3} = g_{3 \times 3}^{-1} T_3 \quad (.99)$$

Since the strain tensor is symmetric, we may reduce it to a 6 component vector, and

$$\begin{pmatrix} \tilde{u}_1^A \\ \tilde{u}_2^A \\ \tilde{u}_3^A \end{pmatrix} = H_{3 \times 6} \begin{pmatrix} \tilde{\sigma}_{11}^\dagger \\ \tilde{\sigma}_{22}^\dagger \\ \tilde{\sigma}_{33}^\dagger \\ \tilde{\sigma}_{23}^\dagger \\ \tilde{\sigma}_{13}^\dagger \\ \tilde{\sigma}_{12}^\dagger \end{pmatrix} \quad (.100)$$

$$H_{3 \times 6} = \begin{bmatrix} g_{11}\zeta_1 & g_{12}\zeta_2 & g_{13}\zeta_3 & 2g_{12}\zeta_3 & 2g_{11}\zeta_3 & 2g_{11}\zeta_2 \\ g_{21}\zeta_1 & g_{22}\zeta_2 & g_{23}\zeta_3 & 2g_{22}\zeta_3 & 2g_{21}\zeta_3 & 2g_{21}\zeta_2 \\ g_{31}\zeta_1 & g_{32}\zeta_2 & g_{33}\zeta_3 & 2g_{32}\zeta_3 & 2g_{31}\zeta_3 & 2g_{31}\zeta_2 \end{bmatrix} \quad (.101)$$

Once the value of u in fourier space is obtained, the final result can be easily calculated with a backward fourier transformation.

When at the origin point in the reciprocal space $\zeta_1^2 + \zeta_2^2 + \zeta_3^2 = 0$, the g matrix is not invertible, we need to treat it slightly differently. Similar to the bulk homogeneous case, we have $\tilde{\mathbf{u}} = 0$

This is only one iteration of the iterative solver, we need to loop until the solution converge.

5 Thin film inhomogeneous system

The equation and boundary condition that we are solving are the Same as the thin film homogeneous case. And we will split the homogeneous and heterogeneous strain in the same fashion as the bulk inhomogeneous case.

5.1 The homogeneous (macroscopic) part

Solving

$$\begin{cases} C_{ijkl}^0 \epsilon_{kl,j} = 0 \\ C_{i3kl}^0 \epsilon_{kl} = 0 \end{cases} \quad (.102)$$

is exactly in the same way as section (2.1), except using C_{ijkl}^0 instead of C_{ijkl} .

5.2 The heterogeneous (microscopic) part

Equation is the same as the bulk inhomogeneous case but with two boundary conditions, and remember we need to solve things iteratively

$$\begin{cases} C_{ijkl}^0 u_{kl}^n = C_{ijkl} \epsilon_{kl}^0 - \delta C_{ijkl} (\bar{\epsilon}_{kl} + u_{k,l}^{n-1}) \\ C_{i3kl} (\bar{\epsilon}_{kl} + u_{k,l} - \epsilon_{kl}^0)|_{x_3=h_f} = \sigma_{i3}^{app} \\ u_i|_{x_3=-h_s} = 0 \end{cases} \quad (.103)$$

5.2.1 Part A: Non-zero rhs, periodic BC

This is the same as bulk inhomogeneous case, section (4.2).

5.2.2 Part B: Zero rhs, thin film BC

$$\begin{cases} C_{ijkl}^0 u_{k,l}^B = 0 \\ C_{i3kl} u_{k,l}^B|_{x_3=h_f} = \sigma_{i3}^{app} - C_{i3kl} (u_{k,l}^A - \epsilon_{kl}^0)|_{x_3=h_f} \\ u_i^B|_{x_3=-h_s} = -u_i^A|_{x_3=-h_s} \end{cases} \quad (.104)$$

$$\Rightarrow \begin{cases} C_{ijkl}^0 u_{k,l}^{B,n} = 0 \\ C_{i3kl} u_{k,l}^{B,n}|_{x_3=h_f} = \sigma_{i3}^{app} - \delta C_{i3kl} u_{k,l}^{B,n-1} - C_{i3kl} (u_{k,l}^A - \epsilon_{kl}^0) + \delta C_{i3kl} \bar{\epsilon}_{kl}|_{x_3=h_f} \\ u_i^B|_{x_3=-h_s} = -u_i^A|_{x_3=-h_s} \end{cases} \quad (.105)$$

In our code, there is a special treatment that we split $C_{i3kl} u_{k,l}^A$ into $C_{i3kl}^0 u_{k,l}^{A,n}$ and

$\delta C_{i3kl} u_{k,l}^{A,n-1}$ and thus the above equations becomes

$$\begin{cases} C_{ijkl}^0 u_{k,lj}^{B,n} = 0 \\ C_{i3kl}^0 u_{k,l}^{B,n} |_{x_3=h_f} = \sigma_{i3}^{app} + C_{i3kl} \epsilon_{kl}^0 - \delta C_{i3kl} u_{k,l}^{n-1} - C_{i3kl}^0 u_{k,l}^{A,n} + \delta C_{i3kl} \bar{\epsilon}_{kl} |_{x_3=h_f} \\ u_i^B |_{x_3=-h_s} = -u_i^A |_{x_3=-h_s} \end{cases} \quad (.106)$$

The way we solve this is exactly the same as thin film homogeneous case Part B.

6 Membrane inhomogeneous system

6.1 The homogeneous (macroscopic) part

The same as homogeneous membrane in section (3.1), and nothing needs to be solved.

6.2 The heterogeneous (microscopic) part

$$\begin{cases} C_{ijkl} \epsilon_{kl}^0 - \delta C_{ijkl} (\bar{\epsilon}_{kl} + u_{k,lj}^{n-1}) \\ C_{i3kl} (u_{k,l} - \epsilon_{kl}^0) |_{x_3=h_f} = \sigma_{i3}^{app} \\ C_{i3kl} (u_{k,l} - \epsilon_{kl}^0) |_{x_3=-h_s} = 0 \end{cases} \quad (.107)$$

6.2.1 Part A: None-zero rhs, periodic BC

The same as bulk inhomogeneous case, section (4.2)

6.2.2 Part B: Zero rhs, membrane BC

Similar to the thin film case,

$$\begin{cases} C_{ijkl}^0 u_{k,lj}^{B,n} = 0 \\ C_{i3kl}^0 u_{k,l}^{B,n} |_{x_3=h_f} = \sigma_{i3}^{app} + C_{i3kl}^0 \epsilon_{kl}^0 - \delta C_{i3kl} u_{k,l}^{n-1} - C_{i3kl}^0 u_{k,l}^{A,n} + \delta C_{i3kl} \bar{\epsilon}_{kl} |_{x_3=h_f} \\ C_{i3kl}^0 u_{k,l}^{B,n} |_{x_3=-h_s} = C_{i3kl}^0 \epsilon_{kl}^0 - \delta C_{i3kl} u_{k,l}^{n-1} - C_{i3kl}^0 u_{k,l}^{A,n} + \delta C_{i3kl} \bar{\epsilon}_{kl} |_{x_3=-h_s} \end{cases} \quad (.108)$$

And then we can solve it using the same solver for homogeneous membrane case, heterogeneous part B, section (3.2.2)

Bibliography

- [1] GAO, P., S. YANG, R. ISHIKAWA, N. LI, B. FENG, A. KUMAMOTO, N. SHIBATA, P. YU, and Y. IKUHARA (2018) “Atomic-Scale Measurement of Flexoelectric Polarization at SrTiO₃ Dislocations,” *Physical Review Letters*, **120**(26), p. 267601.
<https://link.aps.org/doi/10.1103/PhysRevLett.120.267601>
- [2] LI, L., J. R. JOKISAARI, Y. ZHANG, X. CHENG, X. YAN, C. HEIKES, Q. LIN, C. GADRE, D. G. SCHLOM, L.-Q. CHEN, and X. PAN (2018) “Control of Domain Structures in Multiferroic Thin Films through Defect Engineering,” *Advanced Materials*, **30**(38), p. 1802737.
<https://onlinelibrary.wiley.com/doi/full/10.1002/adma.201802737>
- [3] MATSUNAGA, T. and H. SAKA (2000) “Transmission Electron Microscopy of Dislocations in SrTiO₃,” *Philosophical Magazine Letters*, **80**(9), pp. 597–604.
<https://doi.org/10.1080/09500830050134309>
- [4] VALASEK, J. (1921) “Piezo-Electric and Allied Phenomena in Rochelle Salt,” *Physical Review*, **17**(4), pp. 475–481.
<https://link.aps.org/doi/10.1103/PhysRev.17.475>
- [5] SLATER, J. C. (1941) “Theory of the Transition in KH₂PO₄,” *The Journal of Chemical Physics*, **9**(1), pp. 16–33.
<https://aip.scitation.org/doi/abs/10.1063/1.1750821>
- [6] MERZ, W. J. (1954) “Domain Formation and Domain Wall Motions in Ferroelectric BaTiO₃ Single Crystals,” *Physical Review*, **95**(3), pp. 690–698.
<https://link.aps.org/doi/10.1103/PhysRev.95.690>
- [7] SHIRANE, G. and A. TAKEDA (1952) “Phase Transitions in Solid Solutions of PbZrO₃ and PbTiO₃ (I) Small Concentrations of PbTiO₃,” *Journal of the Physical Society of Japan*, **7**(1), p. 5.
- [8] WANG, J., J. B. NEATON, H. ZHENG, V. NAGARAJAN, S. B. OGALE, B. LIU, D. VIEHLAND, V. VAITHYANATHAN, D. G. SCHLOM, U. V. WAGHMARE, N. A. SPALDIN, K. M. RABE, M. WUTTIG, and R. RAMESH (2003) “Epitaxial BiFeO₃ Multiferroic Thin Film Heterostructures,” *Science*, **299**(5613), pp. 1719–1722, 12637741.
<https://science.sciencemag.org/content/299/5613/1719>

- [9] OUCHI, H., K. NAGANO, and S. HAYAKAWA (1965) “Piezoelectric Properties of $\text{Pb}(\text{Mg}_{1/3}\text{Nb}_{2/3})\text{O}_3\text{-PbTiO}_3\text{-PbZrO}_3$ Solid Solution Ceramics,” *Journal of the American Ceramic Society*, **48**(12), p. 630.
<https://ceramics.onlinelibrary.wiley.com/doi/abs/10.1111/j.1151-2916.1965.tb14694.x>
- [10] DEVONSHIRE, A. F. (1949) “XCVI. Theory of Barium Titanate,” *The London, Edinburgh, and Dublin Philosophical Magazine and Journal of Science*, **40**(309), pp. 1040–1063.
<https://doi.org/10.1080/14786444908561372>
- [11] BUIXADERAS, E., S. KAMBA, and J. PETZELT (2004) “Lattice Dynamics and Central-Mode Phenomena in the Dielectric Response of Ferroelectrics and Related Materials,” *Ferroelectrics*, **308**(1), pp. 131–192.
<https://doi.org/10.1080/00150190490508909>
- [12] AHART, M., M. SOMAYAZULU, R. E. COHEN, P. GANESH, P. DERA, H.-K. MAO, R. J. HEMLEY, Y. REN, P. LIERMANN, and Z. WU (2008) “Origin of Morphotropic Phase Boundaries in Ferroelectrics,” *Nature*, **451**(7178), pp. 545–548.
<https://www.nature.com/articles/nature06459>
- [13] SHUR, V., E. RUMYANTSEV, R. BATCHKO, G. MILLER, M. FEJER, and R. BYER (1999) “Physical Basis of the Domain Engineering in the Bulk Ferroelectrics,” *Ferroelectrics*, **221**(1), pp. 157–167.
<https://doi.org/10.1080/00150199908016450>
- [14] VON HIPPEL, A., R. G. BRECKENRIDGE, F. G. CHESLEY, and L. TISZA (1946) “High Dielectric Constant Ceramics,” *Industrial & Engineering Chemistry*, **38**(11), pp. 1097–1109.
<https://doi.org/10.1021/ie50443a009>
- [15] HO, J.-J., Y. FANG, K. WU, W. HSIEH, C. CHU, C. HUANG, M. JU, and C. CHANG (1998) “A High Sensitivity Lead-Titanate (PbTiO_3) Pyroelectric Thin-Film Infrared Sensor with Temperature Isolation Improvement Structure,” *IEEE Electron Device Letters*, **19**(6), pp. 189–191.
- [16] LIAO, W.-Q., Y. ZHANG, C.-L. HU, J.-G. MAO, H.-Y. YE, P.-F. LI, S. D. HUANG, and R.-G. XIONG (2015) “A Lead-Halide Perovskite Molecular Ferroelectric Semiconductor,” *Nature Communications*, **6**(1), pp. 1–7.
<https://www.nature.com/articles/ncomms8338>
- [17] YE, H.-Y., Y.-Y. TANG, P.-F. LI, W.-Q. LIAO, J.-X. GAO, X.-N. HUA, H. CAI, P.-P. SHI, Y.-M. YOU, and R.-G. XIONG (2018) “Metal-Free Three-Dimensional Perovskite Ferroelectrics,” *Science*, **361**(6398), pp. 151–155, 30002249.
<https://science.sciencemag.org/content/361/6398/151>
- [18] CATALAN, G., J. SEIDEL, R. RAMESH, and J. F. SCOTT (2012) “Domain Wall Nanoelectronics,” *Reviews of Modern Physics*, **84**(1), pp. 119–156.
<https://link.aps.org/doi/10.1103/RevModPhys.84.119>

- [19] QIU, C., B. WANG, N. ZHANG, S. ZHANG, J. LIU, D. WALKER, Y. WANG, H. TIAN, T. R. SHROUT, Z. XU, L.-Q. CHEN, and F. LI (2020) “Transparent Ferroelectric Crystals with Ultrahigh Piezoelectricity,” *Nature*, **577**(7790), pp. 350–354.
<https://www.nature.com/articles/s41586-019-1891-y>
- [20] VAN BENTHEM, K., C. ELSÄSSER, and R. H. FRENCH (2001) “Bulk Electronic Structure of SrTiO₃: Experiment and Theory,” *Journal of Applied Physics*, **90**(12), pp. 6156–6164.
<https://aip.scitation.org/doi/10.1063/1.1415766>
- [21] RIMAI, L. and G. A. DEMARS (1962) “Electron Paramagnetic Resonance of Trivalent Gadolinium Ions in Strontium and Barium Titanates,” *Physical Review*, **127**(3), pp. 702–710.
<https://link.aps.org/doi/10.1103/PhysRev.127.702>
- [22] FLEURY, P. A., J. F. SCOTT, and J. M. WORLOCK (1968) “Soft Phonon Modes and the 110K Phase Transition in SrTiO₃,” *Physical Review Letters*, **21**(1), pp. 16–19.
<https://link.aps.org/doi/10.1103/PhysRevLett.21.16>
- [23] SHIRANE, G. and Y. YAMADA (1969) “Lattice-Dynamical Study of the 110K Phase Transition in SrTiO₃,” *Physical Review*, **177**(2), pp. 858–863.
<https://link.aps.org/doi/10.1103/PhysRev.177.858>
- [24] GLAZER, A. M. (1972) “The Classification of Tilted Octahedra in Perovskites,” *Acta Crystallographica Section B: Structural Crystallography and Crystal Chemistry*, **28**(11), pp. 3384–3392.
[//scripts.iucr.org/cgi-bin/paper?a09401](https://scripts.iucr.org/cgi-bin/paper?a09401)
- [25] UNOKI, H. and T. SAKUDO (1967) “Electron Spin Resonance of Fe³⁺ in SrTiO₃ with Special Reference to the 110K Phase Transition,” *Journal of the Physical Society of Japan*, **23**(3), pp. 546–552.
<https://journals.jps.jp/doi/abs/10.1143/JPSJ.23.546>
- [26] FLEURY, P. A. and J. M. WORLOCK (1968) “Electric-Field-Induced Raman Scattering in SrTiO₃ and KTaO₃,” *Physical Review*, **174**(2), pp. 613–623.
<https://link.aps.org/doi/10.1103/PhysRev.174.613>
- [27] YAMADA, Y. and G. SHIRANE (1969) “Neutron Scattering and Nature of the Soft Optical Phonon in SrTiO₃,” *Journal of the Physical Society of Japan*, **26**(2), pp. 396–403.
<https://journals.jps.jp/doi/abs/10.1143/JPSJ.26.396>
- [28] NOZAWA, S., T. IWAZUMI, and H. OSAWA (2005) “Direct Observation of the Quantum Fluctuation Controlled by Ultraviolet Irradiation in SrTiO₃,” *Physical Review B*, **72**(12), p. 121101.
<https://link.aps.org/doi/10.1103/PhysRevB.72.121101>

- [29] COLLIGNON, C., X. LIN, C. W. RISCHAU, B. FAUQUÉ, and K. BEHNIA (2019) “Metallicity and Superconductivity in Doped Strontium Titanate,” *Annual Review of Condensed Matter Physics*, **10**(1), p. 25.
<https://doi.org/10.1146/annurev-conmatphys-031218-013144>
- [30] MÜLLER, K. A. and H. BURKARD (1979) “SrTiO₃: An Intrinsic Quantum Paraelectric below 4 K,” *Physical Review B*, **19**(7), pp. 3593–3602.
<https://link.aps.org/doi/10.1103/PhysRevB.19.3593>
- [31] BEDNORZ, J. G. and K. A. MÜLLER (1984) “Sr_{1-x}Ca_xTiO₃: An XY Quantum Ferroelectric with Transition to Randomness,” *Physical Review Letters*, **52**(25), pp. 2289–2292.
<https://link.aps.org/doi/10.1103/PhysRevLett.52.2289>
- [32] ANG, C., Z. YU, P. M. VILARINHO, and J. L. BAPTISTA (1998) “Bi:SrTiO₃: A Quantum Ferroelectric and a Relaxor,” *Physical Review B*, **57**(13), pp. 7403–7406.
<https://link.aps.org/doi/10.1103/PhysRevB.57.7403>
- [33] RANJAN, R., R. HACKL, A. CHANDRA, E. SCHMIDBAUER, D. TROTS, and H. BOYSEN (2007) “High-Temperature Relaxor Ferroelectric Behavior in Pr-Doped SrTiO₃,” *Physical Review B*, **76**(22), p. 224109.
<https://link.aps.org/doi/10.1103/PhysRevB.76.224109>
- [34] KUMAR, A. S., P. SURESH, M. M. KUMAR, H. SRIKANTH, M. L. POST, K. SAHNER, R. MOOS, and S. SRINATH (2010) “Magnetic and Ferroelectric Properties of Fe Doped SrTiO_{3-δ} Films,” *Journal of Physics: Conference Series*, **200**(9), p. 092010.
<http://stacks.iop.org/1742-6596/200/i=9/a=092010?key=crossref.a4e4e2f3cf01f44c8ae790309c075f7b>
- [35] ITOH, M., R. WANG, Y. INAGUMA, T. YAMAGUCHI, Y.-J. SHAN, and T. NAKAMURA (1999) “Ferroelectricity Induced by Oxygen Isotope Exchange in Strontium Titanate Perovskite,” *Physical Review Letters*, **82**(17), pp. 3540–3543.
<https://link.aps.org/doi/10.1103/PhysRevLett.82.3540>
- [36] UWE, H. and T. SAKUDO (1976) “Stress-Induced Ferroelectricity and Soft Phonon Modes in SrTiO₃,” *Physical Review B*, **13**(1), pp. 271–286.
<https://link.aps.org/doi/10.1103/PhysRevB.13.271>
- [37] HAENI, J. H., P. IRVIN, W. CHANG, R. UECKER, P. REICHE, Y. L. LI, S. CHOUDHURY, W. TIAN, M. E. HAWLEY, B. CRAIGO, A. K. TAGANTSEV, X. Q. PAN, S. K. STREIFFER, L. Q. CHEN, S. W. KIRCHOEFER, J. LEVY, and D. G. SCHLOM (2004) “Room-Temperature Ferroelectricity in Strained SrTiO₃,” *Nature*, **430**(7001), p. 758.
<https://www.nature.com/articles/nature02773>
- [38] HEMBERGER, J., P. LUNKENHEIMER, R. VIANA, R. BÖHMER, and A. LOIDL (1995) “Electric-Field-Dependent Dielectric Constant and Nonlinear Susceptibility

- in SrTiO₃,” *Physical Review B*, **52**(18), pp. 13159–13162.
<https://link.aps.org/doi/10.1103/PhysRevB.52.13159>
- [39] KOONCE, C. S., M. L. COHEN, J. F. SCHOOLEY, W. R. HOSLER, and E. R. PFEIFFER (1967) “Superconducting Transition Temperatures of Semiconducting SrTiO₃,” *Physical Review*, **163**(2), pp. 380–390.
<https://link.aps.org/doi/10.1103/PhysRev.163.380>
- [40] PAI, Y.-Y., A. TYLAN-TYLER, P. IRVIN, and J. LEVY (2018) “Physics of SrTiO₃-Based Heterostructures and Nanostructures: A Review,” *Reports on Progress in Physics*, **81**(3), p. 036503.
<https://doi.org/10.1088%2F1361-6633%2Faa892d>
- [41] BIN ADNAN, M. A., K. ARIFIN, L. J. MINGGU, and M. B. KASSIM (2018) “Titanate-Based Perovskites for Photochemical and Photoelectrochemical Water Splitting Applications: A Review,” *International Journal of Hydrogen Energy*, **43**(52), pp. 23209–23220.
<http://www.sciencedirect.com/science/article/pii/S0360319918334062>
- [42] SIGLE, W., C. SARBU, D. BRUNNER, and M. RUHLE (2006) “Dislocations in Plastically Deformed SrTiO₃,” *Philosophical Magazine*, **86**(29), pp. 4809–4821.
<://WOS:000239756100018>
- [43] ZHANG, Z. L., W. SIGLE, W. KURTZ, and M. RUHLE (2002) “Electronic and Atomic Structure of a Dissociated Dislocation in SrTiO₃,” *Physical Review B*, **66**(21).
<://WOS:000180318800041>
- [44] ZHANG, Z. L., W. SIGLE, and M. RUHLE (2002) “Atomic and Electronic Characterization of the a[100] Dislocation Core in SrTiO₃,” *Physical Review B*, **66**(9).
<://WOS:000178383200036>
- [45] ZHANG, Z. L., W. SIGLE, and W. KURTZ (2004) “HRTEM and EELS Study of Screw Dislocation Cores in SrTiO₃,” *Physical Review B*, **69**(14).
<://WOS:000221426200020>
- [46] HLINKA, J. and P. MÁRTON (2006) “Phenomenological Model of a 90° Domain Wall in BaTiO₃-Type Ferroelectrics,” *Physical Review B*, **74**(10), p. 104104.
<https://link.aps.org/doi/10.1103/PhysRevB.74.104104>
- [47] SHENG, G., Y. L. LI, J. X. ZHANG, S. CHOUDHURY, Q. X. JIA, V. GOPALAN, D. G. SCHLOM, Z. K. LIU, and L. Q. CHEN (2010) “A Modified Landau-Devonshire Thermodynamic Potential for Strontium Titanate,” *Applied Physics Letters*, **96**(23), p. 232902.
<https://aip.scitation.org/doi/abs/10.1063/1.3442915>
- [48] SANDO, D., A. BARTHÉLÉMY, and M. BIBES (2014) “BiFeO₃ Epitaxial Thin Films and Devices: Past, Present and Future,” *Journal of Physics: Condensed Matter*, **26**(47), p. 473201.
<https://doi.org/10.1088%2F0953-8984%2F26%2F47%2F473201>

- [49] PALAI, R., R. S. KATIYAR, H. SCHMID, P. TISSOT, S. J. CLARK, J. ROBERTSON, S. A. T. REDFERN, G. CATALAN, and J. F. SCOTT (2008) “ β Phase and γ - β Metal-Insulator Transition in Multiferroic BiFeO₃,” *Physical Review B*, **77**(1), p. 014110.
<https://link.aps.org/doi/10.1103/PhysRevB.77.014110>
- [50] MOREAU, J. M., C. MICHEL, R. GERSON, and W. J. JAMES (1971) “Ferroelectric BiFeO₃ X-Ray and Neutron Diffraction Study,” *Journal of Physics and Chemistry of Solids*, **32**(6), pp. 1315–1320.
<http://www.sciencedirect.com/science/article/pii/S0022369771801890>
- [51] KUBEL, F. and H. SCHMID (1990) “Structure of a Ferroelectric and Ferroelastic Monodomain Crystal of the Perovskite BiFeO₃,” *Acta Crystallographica Section B: Structural Science*, **46**(6), pp. 698–702.
[//scripts.iucr.org/cgi-bin/paper?du0188](https://scripts.iucr.org/cgi-bin/paper?du0188)
- [52] CLARK, S. J. and J. ROBERTSON (2007) “Band Gap and Schottky Barrier Heights of Multiferroic BiFeO₃,” *Applied Physics Letters*, **90**(13), p. 132903.
<https://aip.scitation.org/doi/full/10.1063/1.2716868>
- [53] MEGAW, H. D. and C. N. W. DARLINGTON (1975) “Geometrical and Structural Relations in the Rhombohedral Perovskites,” *Acta Crystallographica Section A: Crystal Physics, Diffraction, Theoretical and General Crystallography*, **31**(2), pp. 161–173.
[//scripts.iucr.org/cgi-bin/paper?a11672](https://scripts.iucr.org/cgi-bin/paper?a11672)
- [54] PALEWICZ, A., R. PRZENIOŚŁO, I. SOSNOWSKA, and A. W. HEWAT (2007) “Atomic Displacements in BiFeO₃ as a Function of Temperature: Neutron Diffraction Study,” *Acta Crystallographica Section B: Structural Science*, **63**(4), pp. 537–544.
<http://scripts.iucr.org/cgi-bin/paper?ck5024>
- [55] RIVERA, J.-P. and H. SCHMID (1997) “On the Birefringence of Magnetoelectric BiFeO₃,” *Ferroelectrics*, **204**(1), pp. 23–33.
<https://doi.org/10.1080/00150199708222185>
- [56] MICHEL, C., J.-M. MOREAU, G. D. ACHENBACH, R. GERSON, and W. J. JAMES (1969) “The Atomic Structure of BiFeO₃,” *Solid State Communications*, **7**(9), pp. 701–704.
<http://www.sciencedirect.com/science/article/pii/0038109869905973>
- [57] ZAVALICHE, F., S. Y. YANG, T. ZHAO, Y. H. CHU, M. P. CRUZ, C. B. EOM, and R. RAMESH (2006) “Multiferroic BiFeO₃ Films: Domain Structure and Polarization Dynamics,” *Phase Transitions*, **79**(12), pp. 991–1017.
<https://doi.org/10.1080/01411590601067144>
- [58] EDERER, C. and N. A. SPALDIN (2005) “Weak Ferromagnetism and Magnetoelectric Coupling in Bismuth Ferrite,” *Physical Review B*, **71**(6), p. 060401.
<https://link.aps.org/doi/10.1103/PhysRevB.71.060401>

- [59] SOSNOWSKA, I., T. P. NEUMAIER, and E. STEICHELE (1982) “Spiral Magnetic Ordering in Bismuth Ferrite,” *Journal of Physics C: Solid State Physics*, **15**(23), pp. 4835–4846.
<https://doi.org/10.1088%2F0022-3719%2F15%2F23%2F020>
- [60] LEBEUGLE, D., D. COLSON, A. FORGET, M. VIRET, A. M. BATAILLE, and A. GUKASOV (2008) “Electric-Field-Induced Spin Flop in BiFeO₃ Single Crystals at Room Temperature,” *Physical Review Letters*, **100**(22), p. 227602.
<https://link.aps.org/doi/10.1103/PhysRevLett.100.227602>
- [61] RUETTE, B., S. ZVYAGIN, A. P. PYATAKOV, A. BUSH, J. F. LI, V. I. BELOTELOV, A. K. ZVEZDIN, and D. VIEHLAND (2004) “Magnetic-Field-Induced Phase Transition in BiFeO₃ Observed by High-Field Electron Spin Resonance: Cycloidal to Homogeneous Spin Order,” *Physical Review B*, **69**(6), p. 064114.
<https://link.aps.org/doi/10.1103/PhysRevB.69.064114>
- [62] BÉA, H., M. BIBES, S. PETIT, J. KREISEL, and A. BARTHÉLÉMY (2007) “Structural Distortion and Magnetism of BiFeO₃ Epitaxial Thin Films: A Raman Spectroscopy and Neutron Diffraction Study,” *Philosophical Magazine Letters*, **87**(3-4), pp. 165–174.
<https://doi.org/10.1080/09500830701235802>
- [63] KREISEL, J., M. ALEXE, and P. A. THOMAS (2012) “A Photoferroelectric Material Is More than the Sum of Its Parts,” *Nature Materials*, **11**(4), pp. 260–260.
<https://www.nature.com/articles/nmat3282>
- [64] JI, W., K. YAO, Y.-F. LIM, Y. C. LIANG, and A. SUWARDI (2013) “Epitaxial Ferroelectric BiFeO₃ Thin Films for Unassisted Photocatalytic Water Splitting,” *Applied Physics Letters*, **103**(6), p. 062901.
<https://aip.scitation.org/doi/full/10.1063/1.4817907>
- [65] VALANT, M., A.-K. AXELSSON, and N. ALFORD (2007) “Peculiarities of a Solid-State Synthesis of Multiferroic Polycrystalline BiFeO₃,” *Chemistry of Materials*, **19**(22), pp. 5431–5436.
<https://doi.org/10.1021/cm071730+>
- [66] LEBEUGLE, D., D. COLSON, A. FORGET, M. VIRET, P. BONVILLE, J. F. MARUCCO, and S. FUSIL (2007) “Room-Temperature Coexistence of Large Electric Polarization and Magnetic Order in BiFeO₃ Single Crystals,” *Physical Review B*, **76**(2), p. 024116.
<https://link.aps.org/doi/10.1103/PhysRevB.76.024116>
- [67] CAZAYOUS, M., D. MALKA, D. LEBEUGLE, and D. COLSON (2007) “Electric Field Effect on BiFeO₃ Single Crystal Investigated by Raman Spectroscopy,” *Applied Physics Letters*, **91**(7), p. 071910.
<https://aip.scitation.org/doi/full/10.1063/1.2771380>

- [68] QI, X., J. DHO, R. TOMOV, M. G. BLAMIRE, and J. L. MACMANUS-DRISCOLL (2005) “Greatly Reduced Leakage Current and Conduction Mechanism in Aliovalent-Ion-Doped BiFeO₃,” *Applied Physics Letters*, **86**(6), p. 062903.
<https://aip.scitation.org/doi/10.1063/1.1862336>
- [69] ROJAC, T., M. KOSEC, B. BUDIC, N. SETTER, and D. DAMJANOVIC (2010) “Strong Ferroelectric Domain-Wall Pinning in BiFeO₃ Ceramics,” *Journal of Applied Physics*, **108**(7), p. 074107.
<https://aip.scitation.org/doi/full/10.1063/1.3490249>
- [70] BRETOS, I., R. JIMÉNEZ, C. GUTIÉRREZ-LÁZARO, I. MONTERO, and M. L. CALZADA (2014) “Defect-Mediated Ferroelectric Domain Depinning of Polycrystalline BiFeO₃ Multiferroic Thin Films,” *Applied Physics Letters*, **104**(9), p. 092905.
<https://aip.scitation.org/doi/full/10.1063/1.4867703>
- [71] BAEK, S.-H., C. M. FOLKMAN, J.-W. PARK, S. LEE, C.-W. BARK, T. TYBELL, and C.-B. EOM (2011) “The Nature of Polarization Fatigue in BiFeO₃,” *Advanced Materials*, **23**(14), pp. 1621–1625.
<https://onlinelibrary.wiley.com/doi/full/10.1002/adma.201003612>
- [72] ZOU, X., L. YOU, W. CHEN, H. DING, D. WU, T. WU, L. CHEN, and J. WANG (2012) “Mechanism of Polarization Fatigue in BiFeO₃,” *ACS Nano*, **6**(10), pp. 8997–9004.
<https://doi.org/10.1021/nn303090k>
- [73] MACLAREN, I., L. Q. WANG, B. SCHAFFER, Q. M. RAMASSE, A. J. CRAVEN, S. M. SELBACH, N. A. SPALDIN, S. MIAO, K. KALANTARI, and I. M. REANEY (2013) “Novel Nanorod Precipitate Formation in Neodymium and Titanium Codoped Bismuth Ferrite,” *Advanced Functional Materials*, **23**(6), p. 683.
<https://onlinelibrary.wiley.com/doi/abs/10.1002/adfm.201201835>
- [74] WANG, L. Q., B. SCHAFFER, I. MACLAREN, S. MIAO, A. J. CRAVEN, and I. M. REANEY (2012) “Atomic Scale Structure and Chemistry of Anti-Phase Boundaries in (Bi_{0.85}Nd_{0.15})(Fe_{0.9}Ti_{0.1})O₃ Ceramics,” *Journal of Physics: Conference Series*, **371**, p. 012036.
<https://doi.org/10.1088%2F1742-6596%2F371%2F1%2F012036>
- [75] MACLAREN, I., L. WANG, O. MORRIS, A. J. CRAVEN, R. L. STAMPS, B. SCHAFFER, Q. M. RAMASSE, S. MIAO, K. KALANTARI, I. STERIANOU, and I. M. REANEY (2013) “Local Stabilisation of Polar Order at Charged Antiphase Boundaries in Antiferroelectric (Bi_{0.85}Nd_{0.15})(Ti_{0.1}Fe_{0.9})O₃,” *APL Materials*, **1**(2), p. 021102.
<https://aip.scitation.org/doi/abs/10.1063/1.4818002>
- [76] SALIH, J. M., L. Q. WANG, Q. M. RAMASSE, L. JONES, J. BARTHEL, I. M. REANEY, A. J. CRAVEN, and I. MACLAREN (2016) “Maghemite-like Regions at the Crossing of Two Antiphase Boundaries in Doped BiFeO₃,” *Materials Science and Technology*, **32**(3), pp. 242–247.
<https://doi.org/10.1179/1743284715Y.0000000115>

- [77] LI, L., Y. ZHANG, L. XIE, J. R. JOKISAARI, C. BEEKMAN, J.-C. YANG, Y.-H. CHU, H. M. CHRISTEN, and X. PAN (2017) “Atomic-Scale Mechanisms of Defect-Induced Retention Failure in Ferroelectrics,” *Nano Letters*, **17**(6), pp. 3556–3562.
<https://doi.org/10.1021/acs.nanolett.7b00696>
- [78] LI, L., X. CHENG, J. R. JOKISAARI, P. GAO, J. BRITSON, C. ADAMO, C. HEIKES, D. G. SCHLOM, L.-Q. CHEN, and X. PAN (2018) “Defect-Induced Hedgehog Polarization States in Multiferroics,” *Physical Review Letters*, **120**(13), p. 137602.
<https://link.aps.org/doi/10.1103/PhysRevLett.120.137602>
- [79] VASUDEVAN, R. K., A. N. MOROZOVSKA, E. A. ELISEEV, J. BRITSON, J.-C. YANG, Y.-H. CHU, P. MAKSYMOVYCH, L. Q. CHEN, V. NAGARAJAN, and S. V. KALININ (2012) “Domain Wall Geometry Controls Conduction in Ferroelectrics,” *Nano Letters*, **12**(11), pp. 5524–5531.
<https://doi.org/10.1021/nl302382k>
- [80] LI, Y. L., S. CHOUDHURY, J. H. HAENI, M. D. BIEGALSKI, A. VASUDEVARAO, A. SHARAN, H. Z. MA, J. LEVY, V. GOPALAN, S. TROLIER-MCKINSTRY, D. G. SCHLOM, Q. X. JIA, and L. Q. CHEN (2006) “Phase Transitions and Domain Structures in Strained Pseudocubic (100) SrTiO₃ Thin Films,” *Physical Review B*, **73**(18), p. 184112.
<https://link.aps.org/doi/10.1103/PhysRevB.73.184112>
- [81] CHEN, L.-Q. (2008) “Phase-Field Method of Phase Transitions/Domain Structures in Ferroelectric Thin Films: A Review,” *Journal of the American Ceramic Society*, **91**(6), p. 1835.
<https://ceramics.onlinelibrary.wiley.com/doi/abs/10.1111/j.1551-2916.2008.02413.x>
- [82] HU, S. Y. and L. Q. CHEN (2002) “Diffuse-Interface Modeling of Composition Evolution in the Presence of Structural Defects,” *Computational Materials Science*, **23**(1), pp. 270–282.
<http://www.sciencedirect.com/science/article/pii/S0927025601002063>
- [83] GU, Y., M. LI, A. N. MOROZOVSKA, Y. WANG, E. A. ELISEEV, V. GOPALAN, and L.-Q. CHEN (2014) “Flexoelectricity and Ferroelectric Domain Wall Structures: Phase-Field Modeling and DFT Calculations,” *Physical Review B*, **89**(17), p. 174111.
<https://link.aps.org/doi/10.1103/PhysRevB.89.174111>
- [84] GU, Y., Z. HONG, J. BRITSON, and L.-Q. CHEN (2015) “Nanoscale Mechanical Switching of Ferroelectric Polarization via Flexoelectricity,” *Applied Physics Letters*, **106**(2), p. 022904.
<https://aip.scitation.org/doi/abs/10.1063/1.4905837>
- [85] ZUBKO, P., G. CATALAN, and A. K. TAGANTSEV (2013) “Flexoelectric Effect in Solids,” *Annual Review of Materials Research*, **43**(1), p. 387.
<https://doi.org/10.1146/annurev-matsci-071312-121634>

- [86] NEVILLE, R. C., B. HOENEISEN, and C. A. MEAD (1972) “Permittivity of Strontium Titanate,” *Journal of Applied Physics*, **43**(5), pp. 2124–2131.
<https://aip.scitation.org/doi/10.1063/1.1661463>
- [87] JANG, H. W., A. KUMAR, S. DENEV, M. D. BIEGALSKI, P. MAKSYMOVYCH, C. W. BARK, C. T. NELSON, C. M. FOLKMAN, S. H. BAEK, N. BALKE, C. M. BROOKS, D. A. TENNE, D. G. SCHLOM, L. Q. CHEN, X. Q. PAN, S. V. KALININ, V. GOPALAN, and C. B. EOM (2010) “Ferroelectricity in Strain-Free SrTiO₃ Thin Films,” *Physical Review Letters*, **104**(19), p. 197601.
<https://link.aps.org/doi/10.1103/PhysRevLett.104.197601>
- [88] TENNE, D. A., A. K. FARRAR, C. M. BROOKS, T. HEEG, J. SCHUBERT, H. W. JANG, C. W. BARK, C. M. FOLKMAN, C. B. EOM, and D. G. SCHLOM (2010) “Ferroelectricity in Nonstoichiometric SrTiO₃ Films Studied by Ultraviolet Raman Spectroscopy,” *Applied Physics Letters*, **97**(14), p. 142901.
<https://aip.scitation.org/doi/abs/10.1063/1.3499273>
- [89] BIEGALSKI, M. D., E. VLAHOS, G. SHENG, Y. L. LI, M. BERNHAGEN, P. REICHE, R. UECKER, S. K. STREIFFER, L. Q. CHEN, V. GOPALAN, D. G. SCHLOM, and S. TROLIER-MCKINSTRY (2009) “Influence of Anisotropic Strain on the Dielectric and Ferroelectric Properties of SrTiO₃ Thin Films on DyScO₃ Substrates,” *Physical Review B*, **79**(22), p. 224117.
<https://link.aps.org/doi/10.1103/PhysRevB.79.224117>
- [90] WÖRDENWEBER, R., E. HOLLMANN, R. KUTZNER, and J. SCHUBERT (2007) “Induced Ferroelectricity in Strained Epitaxial SrTiO₃ Films on Various Substrates,” *Journal of Applied Physics*, **102**(4), p. 044119.
<https://aip.scitation.org/doi/abs/10.1063/1.2773680>
- [91] ITOH, M. and H. TANIGUCHI (2007) “Ferroelectricity of SrTiO₃ Induced by Oxygen Isotope Exchange,” in *Ferro- and Antiferroelectricity: Order/Disorder versus Displacive* (N. S. Dalal and A. Bussmann-Holder, eds.), Structure and Bonding, Springer Berlin Heidelberg, p. 89.
https://doi.org/10.1007/430_2006_046
- [92] WANG, B., Y. GU, S. ZHANG, and L.-Q. CHEN (2019) “Flexoelectricity in Solids: Progress, Challenges, and Perspectives,” *Progress in Materials Science*.
<http://www.sciencedirect.com/science/article/pii/S0079642519300465>
- [93] FOUSEK, J., L. E. CROSS, and D. B. LITVIN (1999) “Possible Piezoelectric Composites Based on the Flexoelectric Effect,” *Materials Letters*, **39**(5), pp. 287–291.
<http://www.sciencedirect.com/science/article/pii/S0167577X99000208>
- [94] MA, W. and L. E. CROSS (2002) “Flexoelectric Polarization of Barium Strontium Titanate in the Paraelectric State,” *Applied Physics Letters*, **81**(18), pp. 3440–3442.
<https://aip.scitation.org/doi/abs/10.1063/1.1518559>

- [95] ——— (2005) “Flexoelectric Effect in Ceramic Lead Zirconate Titanate,” *Applied Physics Letters*, **86**(7), p. 072905.
<https://aip.scitation.org/doi/abs/10.1063/1.1868078>
- [96] CATALAN, G., A. LUBK, A. H. G. VLOOSWIJK, E. SNOECK, C. MAGEN, A. JANSSENS, G. RISPENS, G. RIJNDERS, D. H. A. BLANK, and B. NOHEDA (2011) “Flexoelectric Rotation of Polarization in Ferroelectric Thin Films,” *Nature Materials*, **10**(12), pp. 963–967.
<https://www.nature.com/articles/nmat3141>
- [97] LEE, D., A. YOON, S. Y. JANG, J.-G. YOON, J.-S. CHUNG, M. KIM, J. F. SCOTT, and T. W. NOH (2011) “Giant Flexoelectric Effect in Ferroelectric Epitaxial Thin Films,” *Physical Review Letters*, **107**(5), p. 057602.
<https://link.aps.org/doi/10.1103/PhysRevLett.107.057602>
- [98] MASUDA, K., L. VAN LICH, T. SHIMADA, and T. KITAMURA (2019) “Periodically-Arrayed Ferroelectric Nanostructures Induced by Dislocation Structures in Strontium Titanate,” *Physical Chemistry Chemical Physics*, **21**(41), p. 22756.
<https://pubs.rsc.org/en/content/articlelanding/2019/cp/c9cp04147h>
- [99] SZOT, K., C. RODENBÜCHER, G. BIHLMAYER, W. SPEIER, R. ISHIKAWA, N. SHIBATA, and Y. IKUHARA (2018) “Influence of Dislocations in Transition Metal Oxides on Selected Physical and Chemical Properties,” *Crystals*, **8**(6), p. 241.
<https://www.mdpi.com/2073-4352/8/6/241>
- [100] JIANG, W., M. NOMAN, Y. M. LU, J. A. BAIN, P. A. SALVADOR, and M. SKOWRONSKI (2011) “Mobility of Oxygen Vacancy in SrTiO₃ and Its Implications for Oxygen-Migration-Based Resistance Switching,” *Journal of Applied Physics*, **110**(3), p. 034509.
<https://aip.scitation.org/doi/abs/10.1063/1.3622623>
- [101] MARROCHELLI, D., L. SUN, and B. YILDIZ (2015) “Dislocations in SrTiO₃: Easy to Reduce but Not so Fast for Oxygen Transport,” *Journal of the American Chemical Society*, **137**(14), pp. 4735–4748.
<https://doi.org/10.1021/ja513176u>
- [102] GAO, P., R. ISHIKAWA, B. FENG, A. KUMAMOTO, N. SHIBATA, and Y. IKUHARA (2018) “Atomic-Scale Structure Relaxation, Chemistry and Charge Distribution of Dislocation Cores in SrTiO₃,” *Ultramicroscopy*, **184**, pp. 217–224.
<http://www.sciencedirect.com/science/article/pii/S0304399116304132>
- [103] MAO, Z. and K. M. KNOWLES (1996) “Dissociation of Lattice Dislocations in SrTiO₃,” *Philosophical Magazine A*, **73**(3), pp. 699–708.
<https://doi.org/10.1080/01418619608242991>
- [104] KONDO, S., T. MITSUMA, N. SHIBATA, and Y. IKUHARA (2016) “Direct Observation of Individual Dislocation Interaction Processes with Grain Boundaries,” *Science Advances*, **2**(11), p. e1501926.
<https://advances.sciencemag.org/content/2/11/e1501926>

- [105] HIREL, P., P. CARREZ, and P. CORDIER (2016) “From Glissile to Sessile: Effect of Temperature on $\langle 110 \rangle$ Dislocations in Perovskite Materials,” *Scripta Materialia*, **120**, pp. 67–70.
<http://www.sciencedirect.com/science/article/pii/S135964621630121X>
- [106] TAERI, S., D. BRUNNER, W. SIGLE, and M. RÜHLE (2004) “Deformation Behaviour of Strontium Titanate between Room Temperature and 1800 K under Ambient Pressure,” *Zeitschrift für Metallkunde*, **95**(6), pp. 433–446.
<https://www.hanser-elibrary.com/doi/abs/10.3139/146.017984>
- [107] ZUBKO, P., G. CATALAN, A. BUCKLEY, P. R. L. WELCHE, and J. F. SCOTT (2007) “Strain-Gradient-Induced Polarization in SrTiO₃ Single Crystals,” *Physical Review Letters*, **99**(16), p. 167601.
<https://link.aps.org/doi/10.1103/PhysRevLett.99.167601>
- [108] LIN, F.-Y., X. CHENG, L.-Q. CHEN, and S. B. SINNOTT (2018) “Strain Effects on Domain Structures in Ferroelectric Thin Films from Phase-field Simulations,” *Journal of the American Ceramic Society*, **101**(10), pp. 4783–4790.
<https://ceramics.onlinelibrary.wiley.com/doi/abs/10.1111/jace.15705>
- [109] LYMPERAKIS, L., J. NEUGEBAUER, M. ALBRECHT, T. REMMELE, and H. P. STRUNK (2004) “Strain Induced Deep Electronic States around Threading Dislocations in GaN,” *Physical Review Letters*, **93**(19), p. 196401.
<https://link.aps.org/doi/10.1103/PhysRevLett.93.196401>
- [110] ADEPALLI, K. K., J. YANG, J. MAIER, H. L. TULLER, and B. YILDIZ (2017) “Tunable Oxygen Diffusion and Electronic Conduction in SrTiO₃ by Dislocation-Induced Space Charge Fields,” *Advanced Functional Materials*, **27**(22), p. 1700243.
<https://onlinelibrary.wiley.com/doi/abs/10.1002/adfm.201700243>
- [111] STEREN, L. B., M. SIRENA, and J. GUIMPEL (2000) “Substrate Influence on the Magnetoresistance and Magnetic Order in La_{0.6}Sr_{0.4}MnO₃ Films,” *Journal of Magnetism and Magnetic Materials*, **211**(1), pp. 28–34.
<http://www.sciencedirect.com/science/article/pii/S030488539900709X>
- [112] IKUHARA, Y. (2009) “Nanowire Design by Dislocation Technology,” *Progress in Materials Science*, **54**(6), pp. 770–791.
<http://www.sciencedirect.com/science/article/pii/S0079642509000127>
- [113] WASER, R. and M. AONO (2007) “Nanoionics-Based Resistive Switching Memories,” *Nature Materials*, **6**(11), pp. 833–840.
 ://WOS:000250615400020
- [114] JIA, C. L., S. B. MI, K. URBAN, I. VREJOIU, M. ALEXE, and D. HESSE (2009) “Effect of a Single Dislocation in a Heterostructure Layer on the Local Polarization of a Ferroelectric Layer,” *Physical Review Letters*, **102**(11).
 ://WOS:000264380200063

- [115] MISIRLIOGLU, I. B., A. L. VASILIEV, M. AINDOW, and S. P. ALPAY (2005) “Strong Degradation of Physical Properties and Formation of a Dead Layer in Ferroelectric Films Due to Interfacial Dislocations,” *Integrated Ferroelectrics*, **71**(1), pp. 67–80.
<https://doi.org/10.1080/10584580590964709>
- [116] CHU, M.-W., I. SZAFRANIAK, R. SCHOLZ, C. HARNAGEA, D. HESSE, M. ALEXE, and U. GÖSELE (2004) “Impact of Misfit Dislocations on the Polarization Instability of Epitaxial Nanostructured Ferroelectric Perovskites,” *Nature Materials*, **3**(2), pp. 87–90.
<https://www.nature.com/articles/nmat1057>
- [117] NAGARAJAN, V., S. PRASERTCHOUNG, T. ZHAO, H. ZHENG, J. OUYANG, R. RAMESH, W. TIAN, X. Q. PAN, D. M. KIM, C. B. EOM, H. KOHLSTEDT, and R. WASER (2004) “Size Effects in Ultrathin Epitaxial Ferroelectric Heterostructures,” *Applied Physics Letters*, **84**(25), pp. 5225–5227.
<https://aip.scitation.org/doi/abs/10.1063/1.1765742>
- [118] CANEDY, C. L., H. LI, S. P. ALPAY, L. SALAMANCA-RIBA, A. L. ROYTBURD, and R. RAMESH (2000) “Dielectric Properties in Heteroepitaxial Ba_{0.6}Sr_{0.4}TiO₃ Thin Films: Effect of Internal Stresses and Dislocation-Type Defects,” *Applied Physics Letters*, **77**(11), pp. 1695–1697.
<https://aip.scitation.org/doi/abs/10.1063/1.1308531>
- [119] WANG, Y. U., Y. M. JIN, A. M. CUITIÑO, and A. G. KHACHATURYAN (2001) “Nanoscale Phase Field Microelasticity Theory of Dislocations: Model and 3D Simulations,” *Acta Materialia*, **49**(10), pp. 1847–1857.
<http://www.sciencedirect.com/science/article/pii/S1359645401000751>
- [120] HU, S. Y., Y. L. LI, and L. Q. CHEN (2003) “Effect of Interfacial Dislocations on Ferroelectric Phase Stability and Domain Morphology in a Thin Film - a Phase-Field Model,” *Journal of Applied Physics*, **94**(4), pp. 2542–2547.
[://WOS:000184469800064](http://www.sciencedirect.com/science/article/pii/S0021899503000064)
- [121] SEIDEL, J., L. W. MARTIN, Q. HE, Q. ZHAN, Y.-H. CHU, A. ROTHER, M. E. HAWKRIDGE, P. MAKSYMOVYCH, P. YU, M. GAJEK, N. BALKE, S. V. KALININ, S. GEMMING, F. WANG, G. CATALAN, J. F. SCOTT, N. A. SPALDIN, J. ORENSTEIN, and R. RAMESH (2009) “Conduction at Domain Walls in Oxide Multiferroics,” *Nature Materials*, **8**(3), pp. 229–234.
<https://www.nature.com/articles/nmat2373>
- [122] MEIER, D., J. SEIDEL, A. CANO, K. DELANEY, Y. KUMAGAI, M. MOSTOVOY, N. A. SPALDIN, R. RAMESH, and M. FIEBIG (2012) “Anisotropic Conductance at Improper Ferroelectric Domain Walls,” *Nature Materials*, **11**(4), pp. 284–288.
<https://www.nature.com/articles/nmat3249>
- [123] ZHANG, Y., H. LU, X. YAN, X. CHENG, L. XIE, T. AOKI, L. LI, C. HEIKES, S. P. LAU, D. G. SCHLOM, L. CHEN, A. GRUVERMAN, and X. PAN (2019) “Intrinsic

- Conductance of Domain Walls in BiFeO₃,” *Advanced Materials*, **31**(36), p. 1902099.
<https://onlinelibrary.wiley.com/doi/abs/10.1002/adma.201902099>
- [124] JIANG, J., Z. L. BAI, Z. H. CHEN, L. HE, D. W. ZHANG, Q. H. ZHANG, J. A. SHI, M. H. PARK, J. F. SCOTT, C. S. HWANG, and A. Q. JIANG (2018) “Temporary Formation of Highly Conducting Domain Walls for Non-Destructive Read-out of Ferroelectric Domain-Wall Resistance Switching Memories,” *Nature Materials*, **17**(1), pp. 49–56.
<https://www.nature.com/articles/nmat5028>
- [125] BAI, Z. L., X. X. CHENG, D. F. CHEN, D. W. ZHANG, L.-Q. CHEN, J. F. SCOTT, C. S. HWANG, and A. Q. JIANG (2018) “Hierarchical Domain Structure and Extremely Large Wall Current in Epitaxial BiFeO₃ Thin Films,” *Advanced Functional Materials*, **28**(31), p. 1801725.
<https://onlinelibrary.wiley.com/doi/abs/10.1002/adfm.201801725>
- [126] SHARMA, P., D. SANDO, Q. ZHANG, X. CHENG, S. PROSANDEEV, R. BULANADI, S. PROKHORENKO, L. BELLAICHE, L.-Q. CHEN, V. NAGARAJAN, and J. SEIDEL (2019) “Conformational Domain Wall Switch,” *Advanced Functional Materials*, **29**(18), p. 1807523.
<https://onlinelibrary.wiley.com/doi/abs/10.1002/adfm.201807523>
- [127] IHLEFELD, J. F., B. M. FOLEY, D. A. SCRYMGEOUR, J. R. MICHAEL, B. B. MCKENZIE, D. L. MEDLIN, M. WALLACE, S. TROLIER-MCKINSTRY, and P. E. HOPKINS (2015) “Room-Temperature Voltage Tunable Phonon Thermal Conductivity via Reconfigurable Interfaces in Ferroelectric Thin Films,” *Nano Letters*, **15**(3), pp. 1791–1795.
<https://doi.org/10.1021/nl504505t>
- [128] ROYO, M., C. ESCORIHUELA-SAYALERO, J. ÍÑIGUEZ, and R. RURALI (2017) “Ferroelectric Domain Wall Phonon Polarizer,” *Physical Review Materials*, **1**(5), p. 051402.
<https://link.aps.org/doi/10.1103/PhysRevMaterials.1.051402>
- [129] HOPKINS, P. E., C. ADAMO, L. YE, B. D. HUEY, S. R. LEE, D. G. SCHLOM, and J. F. IHLEFELD (2013) “Effects of Coherent Ferroelastic Domain Walls on the Thermal Conductivity and Kapitza Conductance in Bismuth Ferrite,” *Applied Physics Letters*, **102**(12), p. 121903.
<https://aip.scitation.org/doi/full/10.1063/1.4798497>
- [130] WEILERT, M. A., M. E. MSALL, A. C. ANDERSON, and J. P. WOLFE (1993) “Phonon Scattering from Ferroelectric Domain Walls: Phonon Imaging in KDP,” *Physical Review Letters*, **71**(5), pp. 735–738.
<https://link.aps.org/doi/10.1103/PhysRevLett.71.735>
- [131] GIOCONDI, J. L. and G. S. ROHRER (2001) “Spatially Selective Photochemical Reduction of Silver on the Surface of Ferroelectric Barium Titanate,” *Chemistry of Materials*, **13**(2), pp. 241–242.
<https://doi.org/10.1021/cm000890h>

- [132] CHOI, T., S. LEE, Y. J. CHOI, V. KIRYUKHIN, and S.-W. CHEONG (2009) “Switchable Ferroelectric Diode and Photovoltaic Effect in BiFeO₃,” *Science*, **324**(5923), pp. 63–66, 19228998.
<https://science.sciencemag.org/content/324/5923/63>
- [133] CHU, Y.-H., Q. HE, C.-H. YANG, P. YU, L. W. MARTIN, P. SHAFER, and R. RAMESH (2009) “Nanoscale Control of Domain Architectures in BiFeO₃ Thin Films,” *Nano Letters*, **9**(4), pp. 1726–1730.
<https://doi.org/10.1021/nl900723j>
- [134] YADAV, A. K., C. T. NELSON, S. L. HSU, Z. HONG, J. D. CLARKSON, C. M. SCHLEPÜTZ, A. R. DAMODARAN, P. SHAFER, E. ARENHOLZ, L. R. DEDON, D. CHEN, A. VISHWANATH, A. M. MINOR, L. Q. CHEN, J. F. SCOTT, L. W. MARTIN, and R. RAMESH (2016) “Observation of Polar Vortices in Oxide Superlattices,” *Nature*, **530**(7589), pp. 198–201.
<https://www.nature.com/articles/nature16463>
- [135] HONG, Z. and L.-Q. CHEN (2018) “Blowing Polar Skyrmion Bubbles in Oxide Superlattices,” *Acta Materialia*, **152**, pp. 155–161.
<http://www.sciencedirect.com/science/article/pii/S1359645418302982>
- [136] XUE, F., Y. GU, L. LIANG, Y. WANG, and L.-Q. CHEN (2014) “Orientations of Low-Energy Domain Walls in Perovskites with Oxygen Octahedral Tilts,” *Physical Review B*, **90**(22), p. 220101.
<https://link.aps.org/doi/10.1103/PhysRevB.90.220101>
- [137] SUN, E. and W. CAO (2014) “Relaxor-Based Ferroelectric Single Crystals: Growth, Domain Engineering, Characterization and Applications,” *Progress in materials science*, **65**, pp. 124–210, 25061239.
<https://www.ncbi.nlm.nih.gov/pmc/articles/PMC4104389/>
- [138] KHAN, A. I., K. CHATTERJEE, B. WANG, S. DRAPCHO, L. YOU, C. SERRAO, S. R. BAKAUL, R. RAMESH, and S. SALAHUDDIN (2015) “Negative Capacitance in a Ferroelectric Capacitor,” *Nature Materials*, **14**(2), pp. 182–186.
<https://www.nature.com/articles/nmat4148>
- [139] SEIDEL, J., G. SINGH-BHALLA, Q. HE, S.-Y. YANG, Y.-H. CHU, and R. RAMESH (2013) “Domain Wall Functionality in BiFeO₃,” *Phase Transitions*, **86**(1), pp. 53–66.
<https://doi.org/10.1080/01411594.2012.695371>
- [140] BHATNAGAR, A., A. ROY CHAUDHURI, Y. HEON KIM, D. HESSE, and M. ALEXE (2013) “Role of Domain Walls in the Abnormal Photovoltaic Effect in BiFeO₃,” *Nature Communications*, **4**(1), p. 2835.
<https://www.nature.com/articles/ncomms3835>
- [141] KONTOSOS, A. and C. M. LANDIS (2009) “Computational Modeling of Domain Wall Interactions with Dislocations in Ferroelectric Crystals,” *International Journal of Solids and Structures*, **46**(6), pp. 1491–1498.
<http://www.sciencedirect.com/science/article/pii/S0020768308004939>

- [142] LIU, D., M. CHELF, and K. W. WHITE (2006) “Indentation Plasticity of Barium Titanate Single Crystals: Dislocation Influence on Ferroelectric Domain Walls,” *Acta Materialia*, **54**(17), pp. 4525–4531.
<http://www.sciencedirect.com/science/article/pii/S1359645406003958>
- [143] GAO, P., J. BRITSON, J. R. JOKISAARI, C. T. NELSON, S.-H. BAEK, Y. WANG, C.-B. EOM, L.-Q. CHEN, and X. PAN (2013) “Atomic-Scale Mechanisms of Ferroelastic Domain-Wall-Mediated Ferroelectric Switching,” *Nature Communications*, **4**, p. 2791.
<https://www.nature.com/articles/ncomms3791>
- [144] YANG, T. J., V. GOPALAN, P. J. SWART, and U. MOHIDEEN (1999) “Direct Observation of Pinning and Bowing of a Single Ferroelectric Domain Wall,” *Physical Review Letters*, **82**(20), pp. 4106–4109.
<https://link.aps.org/doi/10.1103/PhysRevLett.82.4106>
- [145] REN, X. (2004) “Large Electric-Field-Induced Strain in Ferroelectric Crystals by Point-Defect-Mediated Reversible Domain Switching,” *Nature Materials*, **3**(2), pp. 91–94.
<https://www.nature.com/articles/nmat1051>
- [146] SEIDEL, J., R. K. VASUDEVAN, and N. VALANOOR (2016) “Topological Structures in Multiferroics – Domain Walls, Skyrmions and Vortices,” *Advanced Electronic Materials*, **2**(1), p. 1500292.
<https://onlinelibrary.wiley.com/doi/abs/10.1002/aelm.201500292>
- [147] KIM, K.-E., S. JEONG, K. CHU, J. H. LEE, G.-Y. KIM, F. XUE, T. Y. KOO, L.-Q. CHEN, S.-Y. CHOI, R. RAMESH, and C.-H. YANG (2018) “Configurable Topological Textures in Strain Graded Ferroelectric Nanoplates,” *Nature Communications*, **9**(1), pp. 1–12.
<https://www.nature.com/articles/s41467-017-02813-5>
- [148] SIMONS, H., A. C. JAKOBSEN, S. R. AHL, H. F. POULSEN, W. PANTLEON, Y.-H. CHU, C. DETLEFS, and N. VALANOOR (2019) “Nondestructive Mapping of Long-Range Dislocation Strain Fields in an Epitaxial Complex Metal Oxide,” *Nano Letters*, **19**(3), pp. 1445–1450.
<https://doi.org/10.1021/acs.nanolett.8b03839>

Vita

Xiaoxing Cheng

Xiaoxing Cheng was born in Tianjin, China on May 14th, 1991. He lived in Tianjin for 8 years, then in Beijing for 5 years, and then moved to Shanghai, where later he was admitted to the Materials Science and Engineering Department of Shanghai Jiaotong University in 2009. After he completed his Bachelor degree in 2013, he was enrolled in the intercollege Ph.D. program of Materials Science and Engineering at the Pennsylvania State University at State Collgege, USA, and joined Dr. Long-qing Chen's research group. The primary research topic of Xiaoxing is the phase-field simulation of microstructure evolution in ferroelectric materials. During his Ph.D. period, he improved the existing phase-field program in Dr. Long-Qing Chen's group and developed several useful tool for performing simulations, including high-throughput jobs creator, 3D data visualization, etc.. His research also lead to a series of peer reviewed collaboration publications. Xiaoxing Cheng received his Ph.D. in 2020.